HELLENIC REPUBLIC
National and Kapodistrian University of Athens
EST. 1837
DEPARTMENT OF GEOLOGY & GEOENVIRONMENT

Postgraduate Programme
Earth Science and Environment

ANGELOS ZYMVRAGAKIS

7114112100002

Probabilistic and Stochastic seismic hazard assessment for Boeotia (Central Greece)

Applied Geology - Geophysics

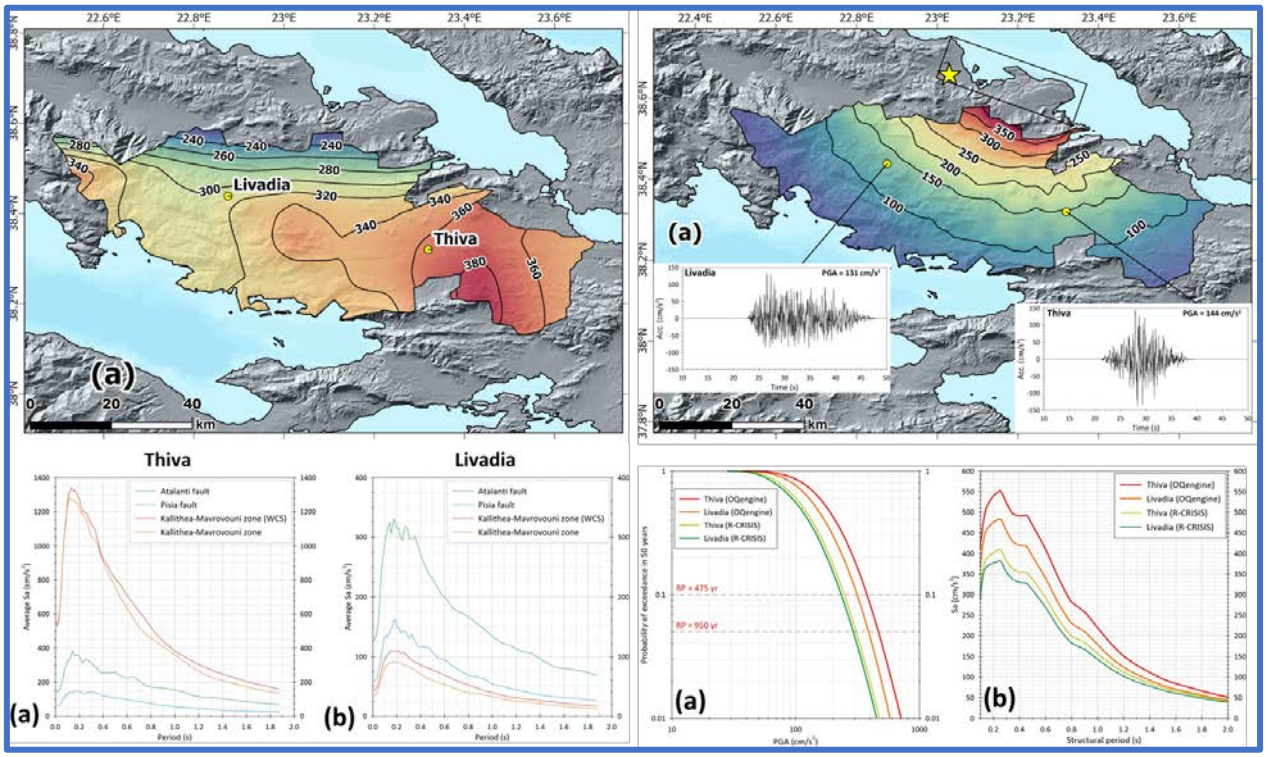

Three-member Committee of Examination

Kaviris George, Associate Professor NKUA, Supervisor

Voulgaris Nicholas, Professor NKUA, Member

Kouskouna Vasiliki, Professor NKUA, Member

ATHENS 2023

ΕΛΛΗΝΙΚΗ ΔΗΜΟΚΡΑΤΙΑ
Εθνικόν και Καποδιστριακόν Πανεπιστήμιον Αθηνών
ΙΔΡΥΘΕΝ ΤΟ 1837
Τμήμα Γεωλογίας και Γεωπεριβάλλοντος

Πρόγραμμα Μεταπτυχιακών Σπουδών
Επιστήμες Γης και Περιβάλλον

ΑΓΓΕΛΟΣ ΖΥΜΒΡΑΓΑΚΗΣ

7114112100002

Πιθανολογική και στοχαστική εκτίμηση σεισμικής επικινδυνότητας στη Βοιωτία (Κεντρική Ελλάδα)

Εφαρμοσμένη Γεωλογία – Γεωφυσική

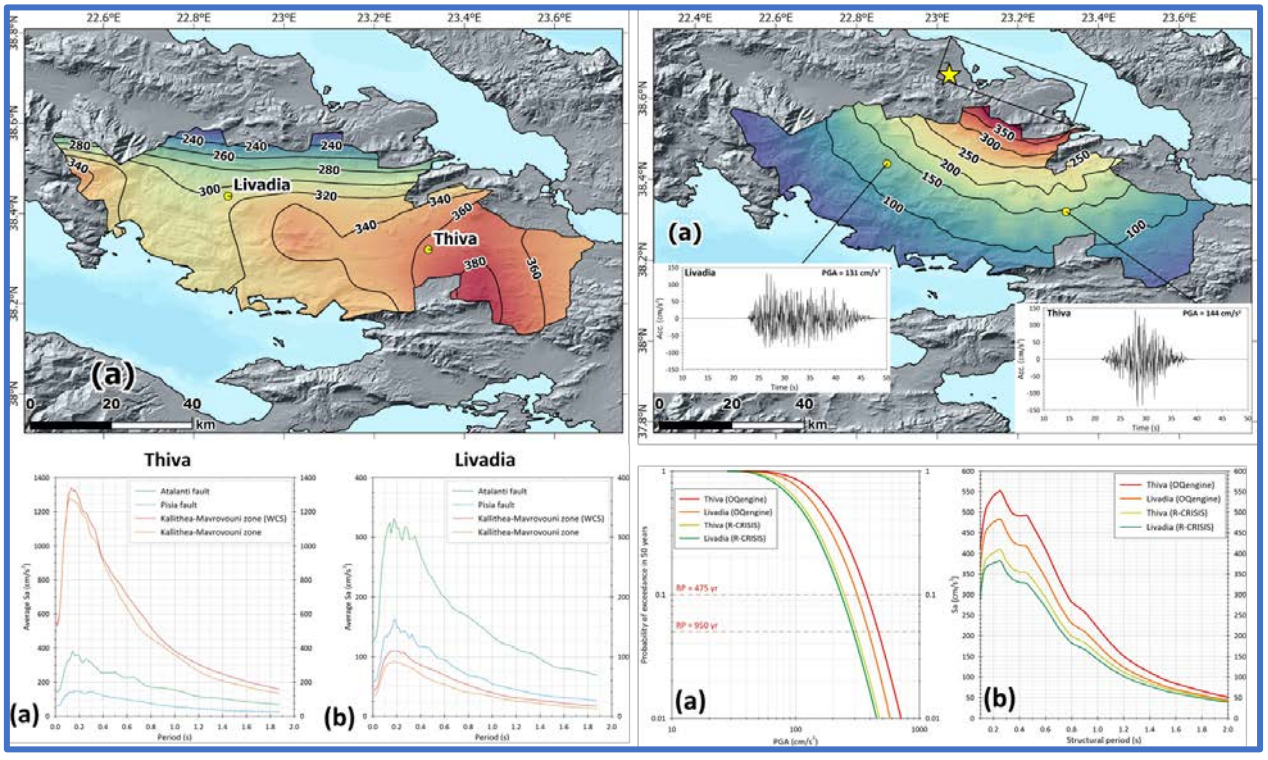

Τριμελής Εξεταστική Επιτροπή:

Καβύρης Γεώργιος, Αναπληρωτής Καθηγητής ΕΚΠΑ, Επιβλέπων

Βούλγαρης Νικόλαος, Καθηγητής ΕΚΠΑ, Μέλος Τριμελούς Εξεταστικής επιτροπής

Κουσκουνά Βασιλική, Καθηγήτρια ΕΚΠΑ, Μέλος Τριμελούς Εξεταστικής επιτροπής

ΑΘΗΝΑ 2023

ΔΗΛΩΣΗ ΠΕΡΙ ΜΗ ΠΡΟΣΒΟΛΗΣ ΠΝΕΥΜΑΤΙΚΗΣ ΙΔΙΟΚΤΗΣΙΑΣ

Προσβολή πνευματικής ιδιοκτησίας θεωρείται η ολική ή η μερική αναπαραγωγή του έργου άλλου προσώπου ή η παρουσίαση του έργου κάποιου άλλου ως προσωπικού του γράφοντος. Το Τμήμα Γεωλογίας και Γεωπεριβάλλοντος λαμβάνει πολύ σοβαρά υπόψη και καταδικάζει την προσφυγή σε τέτοιου είδους πρακτικές από τους Μεταπτυχιακούς Φοιτητές. Σε περιπτώσεις πρόδηλης ή εκ προθέσεως προσβολής πνευματικής ιδιοκτησίας, τα αρμόδια όργανα του Τμήματος δύνανται να επιβάλουν ως κύρωση έως και την οριστική διαγραφή από το ΠΜΣ. Κατά την εκπόνηση, υποβολή, εξέταση και δημοσίευση της Διπλωματικής Εργασίας Ειδίκευσης οι Μεταπτυχιακοί Φοιτητές οφείλουν να τηρούν τις ακόλουθες κατευθυντήριες οδηγίες:

1. Η Διπλωματική Εργασία Ειδίκευσης πρέπει να αποτελεί έργο του υποβάλλοντος αυτήν φοιτητή.
2. Η αντιγραφή ή η παράφραση έργου τρίτου προσώπου αποτελεί προσβολή πνευματικής ιδιοκτησίας και συνιστά σοβαρό αδίκημα. Στο αδίκημα αυτό περιλαμβάνεται τόσο η προσβολή πνευματικής ιδιοκτησίας άλλου φοιτητή όσο και η αντιγραφή από δημοσιευμένες πηγές, όπως βιβλία, εισηγήσεις ή επιστημονικά άρθρα. Το υλικό που συνιστά αντικείμενο λογοκλοπής μπορεί να προέρχεται από οποιαδήποτε πηγή. Η αντιγραφή ή χρήση υλικού προερχόμενου από το διαδίκτυο ή από ηλεκτρονική εγκυκλοπαίδεια είναι εξίσου σοβαρή με τη χρήση υλικού προερχόμενου από τυπωμένη πηγή ή βάση δεδομένων.
3. Η χρήση αποσπασμάτων από το έργο τρίτων είναι αποδεκτή εφόσον, αναφέρεται η πηγή του σχετικούαποσπάσματος. Σε περίπτωση αυτολεξί μεταφοράς αποσπάσματος από το έργο άλλου, η χρήση εισαγωγικών ή σχετικής υποσημείωσης είναι απαραίτητη, ούτως ώστε η πηγή του αποσπάσματος να αναγνωρίζεται.
4. Η παράφραση κειμένου, αποτελεί προσβολή πνευματικής ιδιοκτησίας.
5. Οι πηγές των αποσπασμάτων που χρησιμοποιούνται θα πρέπει να καταγράφονται πλήρως σε πίνακα βιβλιογραφίας στο τέλος της εργασίας.
6. Η προσβολή πνευματικής ιδιοκτησίας επισύρει την επιβολή κυρώσεων. Κατά την απόφαση επί των ενδεδειγμένων κυρώσεων, τα αρμόδια όργανα του Τμήματος θα λαμβάνουν υπόψη παράγοντες όπως το εύρος και το μέγεθος του τμήματος της εργασίας που οφείλεται σε προσβολή πνευματικής ιδιοκτησίας. Οι κυρώσεις θα επιβάλλονται σύμφωναμε το Άρθρο 7 Παράγραφος 7 του Κανονισμού Σπουδών.

Βεβαιώνω ότι η Διπλωματική Εργασία Ειδίκευσης, την οποία υποβάλλω, δεν περιλαμβάνει στοιχεία προσβολής πνευματικής ιδιοκτησίας, όπως αυτά προσδιορίζονται από την παραπάνω δήλωση, τους όρους της οποίας διάβασα και αποδέχομαι.

Παρέχω τη συναίνεσή μου, ώστε ένα ηλεκτρονικό αντίγραφο της διπλωματικής εργασίας μου να υποβληθεί σε ηλεκτρονικό έλεγχο για τον εντοπισμό τυχόν στοιχείων προσβολής πνευματικής ιδιοκτησίας.

Ημερομηνία

22/05/2023

Υπογραφή Υποψηφίου

Άγγελος Ζυμβραγάκης

Preface

This thesis is the result of extensive study in the scientific field of seismic hazard and seismic hazard assessment since 2021. Throughout the course of my bachelor's thesis, titled "Probabilistic seismic hazard assessment for Messinia (SW Peloponnese)" (in Greek), I gained a profound appreciation for the scientific domain of seismic hazard. This inspired me to explore new methodologies and software tools for enhancing my work. Consequently, this master's thesis represents an advancement of my previous bachelor's thesis. In a scientific field predominantly driven by statistical analysis, continuous improvement is crucial. As expressed by the British statistician George Box, "All models are wrong, but some are useful" (Box, 1976). Acknowledging the imperfections inherent in the herein used models, my primary objective is to consistently refine my work in an attempt to minimize epistemic uncertainties. In this thesis all units are following the metric system and the date format is DD/MM/YYYY.

It is essential to recognize the contributions of some individuals, some of which are listed here, who have influenced the development of this thesis, whether to a significant or minor extent. Foremost, I would like to express my deepest gratitude to my supervisor, Associate Professor George Kaviris. I hold immense respect for the countless hours he dedicated to supporting me in various ways, such as engaging in discussions regarding the core aspects of my thesis, offering invaluable suggestions and advice both within and beyond the academic setting. I am particularly grateful for his constructive criticism, as it has played a pivotal role in my scientific and personal growth. I would also like to extend my appreciation to the other two members of the Examining Committee, Professor Vasiliki Kouskouna, whose valuable advice and suggestions significantly enhanced this thesis, and Professor Nicholas Voulgaris, for providing me with opportunities. Furthermore, I express my gratitude to my fellow MSc students, Eleni Anyfanti, Sophie Avgerinou, Vasileios Gkosios and Nikolas Vagionakis, for the fruitful collaboration we shared throughout the master's program. I am also grateful to my friends for their continual encouragement and availability for insightful discussions. Last but not least, I would like to extend a heartfelt appreciation to my parents, Christos and Theoni, and my brothers, Apostolis and Panayotis, for their unconditional love and unwavering support, both emotionally and financially. I am also indebted to MSc Ioannis Spingos for our profound conversations and constructive criticism, as well as Dr. Vasilis Kapetanidis and Dr. Nikolaos Sakellariou for their valuable scientific discussions. Finally, I would like to express my gratitude to all the members of the Section of Geophysics and Geothermics for their invaluable contribution to my academic journey throughout my pursuit of a master's degree. Their profound expertise and guidance have enriched my scientific understanding, while their constructive criticism has played a vital role in my development.

Table of Contents

Περίληψη

Η υπό εξέταση περιοχή μελέτης είναι η Βοιωτία. Η περιοχή αυτή είναι σημαντική από σεισμοτεκτονικής άποψης, καθώς βρίσκεται μεταξύ δύο ενεργών τεκτονικών τάφρων: του Κορινθιακού κόλπου στα νότια και του Ευβοϊκού κόλπου στα βόρεια. Η δυναμική φύση αυτού του περιβάλλοντος έχει οδηγήσει στην εκδήλωση αξιοσημείωτων σεισμών τόσο κοντά όσο και εντός της Βοιωτίας. Μεταξύ των πιο γνωστών σεισμών από την ιστορική εποχή (πριν από το 1900) είναι ο σεισμός της Αταλάντης μεγέθους 7.0, που συνέβη στις 27/04/1894, με το επίκεντρο να εκτιμάται ότι βρισκόταν βόρεια της Βοιωτίας. Ένα άλλο σημαντικό σεισμικό γεγονός εκτιμώμενου μεγέθους 6.0 έλαβε χώρα κοντά στη Θήβα το 1914. Επιπλέον, οι ισχυροί σεισμοί της 24/02/1981, 25/02/1981 και 04/03/1981 με μεγέθη Mw = 6.7, 6.4 και 6.4, αντίστοιχα, εντοπίστηκαν κοντά στα νότια σύνορα της Βοιωτίας. Πρόσφατα, καταγράφηκαν τέσσερις ενδιαμέσου μεγέθους σεισμοί κοντά στη Θήβα: στις 02/12/2020 (Mw = 4.6), στις 11/07/2021 και 20/07/2021 (και τα δύο Mw = 4.2) και στις 02/09/2021 (Mw = 4.1). Λαμβάνοντας υπόψη τη σεισμικότητα της περιοχής, είναι επιτακτική ανάγκη να πραγματοποιηθεί μια επικαιροποιημένη εκτίμηση της σεισμικής επικινδυνότητας για την περιοχή της Βοιωτίας, με στόχο τη μείωση των επιστημονικών αβεβαιοτήτων. Η εκτίμηση αυτή επικεντρώθηκε στην ποσοτικοποίηση των μέγιστων αναμενόμενων εδαφικών κινήσεων, μέσω του υπολογισμού της μέγιστης εδαφικής επιτάχυνσης (PGA), της μέγιστης εδαφικής ταχύτητας (PGV) και των φασματικών τιμών επιτάχυνσης (Sa). Οι τιμές Sa προσδιορίστηκαν αποκλειστικά για τις δύο πιο σημαντικές πόλεις της Βοιωτίας, τη Λιβαδειά και τη Θήβα. Για την εκτίμηση της σεισμικής επικινδυνότητας χρησιμοποιήθηκαν δύο μεθοδολογίες: η κλασική ημιστατιστική πιθανολογική προσέγγιση και η στοχαστική προσομοίωση εδαφικής κίνησης σε ρήγματα πεπερασμένων διαστάσεων. Στην πρώτη προσέγγιση, χρησιμοποιήθηκαν τρία σεισμοτεκτονικά μοντέλα με τη μορφή επιφανειακών ζωνών, καθώς και ένας επικαιροποιημένος κατάλογος ενόργανης σεισμικότητας. Εφαρμόστηκαν πολλές σχέσεις απόσβεσης (GMPEs), οι οποίες ανακατασκευάστηκαν ώστε να λαμβάνουν υπόψη τα κύρια είδη των μηχανισμών γένεσης με βάση τα σχετικά ποσοστά τους ανά ζώνη. Τα αποτελέσματα προέκυψαν μέσω λογικού δέντρου και απεικονίστηκαν με τη μορφή χαρτών για τις παραμέτρους PGA και PGV, για περιόδους επανάληψης 475 και 950 ετών, καμπυλών επικινδυνότητας PGA, καθώς και ομοιόμορφων φασμάτων επικινδυνότητας (UHS) Sa τύπου για τη Λιβαδειά και τη Θήβα. Όσον αφορά τη δεύτερη προσέγγιση, διεξήχθη διαδικασία βαθμονόμησης πριν από τις στοχαστικές προσομοιώσεις για να εξασφαλιστεί η ακριβής ενσωμάτωση των παραμέτρων της πηγής, της διαδρομής και του εδάφους. Στη συνέχεια, κατασκευάστηκαν τέσσερα σενάρια σεισμών για την αξιολόγηση των μοντελοποιημένων τιμών PGA, PGV και Sa. Τα σενάρια αυτά περιλάμβαναν τους σεισμούς της Αταλάντης με μέγεθος 7.0, των Αλκυονίδων με μέγεθος 6.4 και της Θήβας με μέγεθος 6.0, καθώς και το ακραίο σενάριο ταυτόχρονης ενεργοποίησης των ρηγμάτων Καλλιθέας - Μαυροβουνίου. Αναλύοντας τα αποτελέσματα που προέκυψαν μέσω της πιθανολογικής προσέγγισης, παρατηρήθηκε ότι το κεντρικό και το βόρειο τμήμα της Βοιωτίας καλύπτονται από την τιμή PGA που προτείνει ο ισχύων Ελληνικός Αντισεισμικός Κανονισμός, ενώ οι τιμές που υπολογίστηκαν για το νότιο τμήμα υπερβαίνουν τον κανονισμό αυτόν. Η Θήβα παρουσίασε υψηλότερα επίπεδα σεισμικής επικινδυνότητας από τη Λιβαδειά σε όλες τις περιόδους επανάληψης και επίσης επέδειξε υψηλότερες τιμές Sa σε όλες τις συχνότητες. Σχετικά με τη δεύτερη προσέγγιση, μόνο το σενάριο του σεισμού των Αλκυονίδων προσομοίωσε εδαφικές κινήσεις που συμφωνούν με τον κανονισμό. Ο σεισμός της Αταλάντης αποτελεί μεγαλύτερη απειλή για τη Λιβαδειά, ενώ η προσομοιωμένη διάρρηξη της ενεργού ζώνης με μέγεθος 6.3 (Καλλιθέα – Μαυροβούνι) αποτελεί σημαντική απειλή για τη Θήβα.

Abstract

The study area under investigation is Boeotia, located in Central Greece. This region is of considerable seismotectonic significance, as it lies between two active tectonic rifts: the Gulf of Corinth to the south and the Euboekos Gulf to the north. This setting has resulted in notable seismic events, both close and within Boeotia. Among the most well-known earthquakes from the historical era (pre-1900) is the Atalanti event of magnitude 7.0, which occurred on 27/04/1894, with its epicenter estimated to be north of Boeotia. Another significant seismic event of estimated magnitude 6.0 took place in the main town of Boeotia, Thiva, in 1914. Furthermore, the events of 24/02/1981, 25/02/1981 and 04/03/1981 with magnitudes Mw = 6.7, 6.4 and 6.4, respectively, are located close to the southern borders of Boeotia. Recently, four moderate events with magnitudes greater than 4.0 occurred close to Thiva: on 02/12/2020 (Mw = 4.6), 11/07/2021, 20/07/2021 (both Mw = 4.2) and 02/09/2021 (Mw = 4.1). It is imperative to conduct an up-to-date seismic hazard assessment for the Boeotia area, with the aim of reducing epistemic uncertainties. The assessment focused on quantifying the maximum anticipated ground motions through the computation of Peak Ground Acceleration (PGA), Peak Ground Velocity (PGV), and Spectral acceleration values (Sa). The Sa values were determined exclusively for the two major towns in Boeotia, Livadia and Thiva. Two methodologies were employed for the seismic hazard assessment: the classical semi-probabilistic approach and the scenario-based finite fault stochastic ground motion simulation. In the first approach, three seismotectonic models in the form of area sources were utilized, along with an updated earthquake catalogue. Multiple Ground Motion Prediction Equations (GMPEs) were applied to account for the main types of fault plane solutions based on their relative percentages. The results were derived through a logic tree approach and were visualized in the form of maps for PGA and PGV, considering return periods of 475 and 950 years, PGA-hazard curves for Livadia and Thiva, and Uniform Hazard Spectra (in terms of Sa) for Livadia and Thiva. Regarding the second approach, a calibration procedure was conducted prior to the stochastic simulations to ensure accurate incorporation of the source, path, and site parameters. Four earthquake scenarios were constructed to evaluate the modeled PGA, PGV, and Sa values. These scenarios included the 1894 Atalanti event with magnitude 7.0, the 1981 Alkyonides earthquake with magnitude 6.4, a simulation of an active zone rupture yielding an earthquake with magnitude 6.3, and the 1914 Thiva event with magnitude 6.0. Analyzing the results obtained via the probabilistic approach, it was observed that the central and northern portions of Boeotia generally comply with the PGA value proposed by the Greek Building Code, whereas the southern portion exceeds this value. Thiva exhibited higher levels of seismic hazard than Livadia across all return periods and demonstrated higher Sa values across all frequencies. Shifting focus to the second approach, only the scenario involving the Alkyonides earthquake generated ground motions that conform to the regulations outlined in the Greek Building Code. The Atalanti event posed a greater threat to Livadia, while the simulated rupture of the active zone of Kallithea – Mavrovouni with magnitude 6.3 poses a significant threat to Thiva.

1 Introduction

The study area of the present MSc thesis is Boeotia, a region located in Central Greece (Figure I), with a total population of 106,107 (ELSTAT, 2021). The capital town, Livadia, hosts 27,379 residents (ELSTAT, 2021). Boeotia holds significant importance in the seismotectonic field due to its proximity to two active gulfs: the Gulf of Corinth (GoC), situated along its southern border, and the Euboeokos Gulf, located to the north (Figure I). The region's active tectonic background is responsible for significant earthquake events. One of the notable earthquake sequences that occurred in the vicinity of the study area is the destructive 1981 Alkionides earthquake sequence, with the mainshock (24/02/1981) having a magnitude of Mw = 6.7. Two major events, both with Mw = 6.4 occurred on 25/02/1981 and on 04/03/1981. Another noteworthy seismic event in the region is the historical Atalanti earthquake of 27/03/1894, with an estimated magnitude of M = 7.0. Another important earthquake is the one that occurred in 1914 in Thiva, a main town within Boeotia with a population of 32,410 residents, which had significant implications to the area. Recently, a sequence was initiated during the end of November 2020, with small magnitude earthquakes located near Kallithea village. On 02/12/2020 a Mw = 4.6 earthquake was located near Kallithea and the aftershocks lasted until January 2021. An event of Mw = 4.2 struck a few km to the west of Kallithea, close to Thiva on 11/07/2021, followed by an occurrence of similar magnitude earthquake on 20/07/2021 in the same area. Another earthquake of magnitude Mw > 4.0 was recorded in the same epicentral area on 02/09/2021. These instances serve as compelling evidence of the area's susceptibility to significant earthquake occurrences, underscoring the seismic potential within Boeotia.

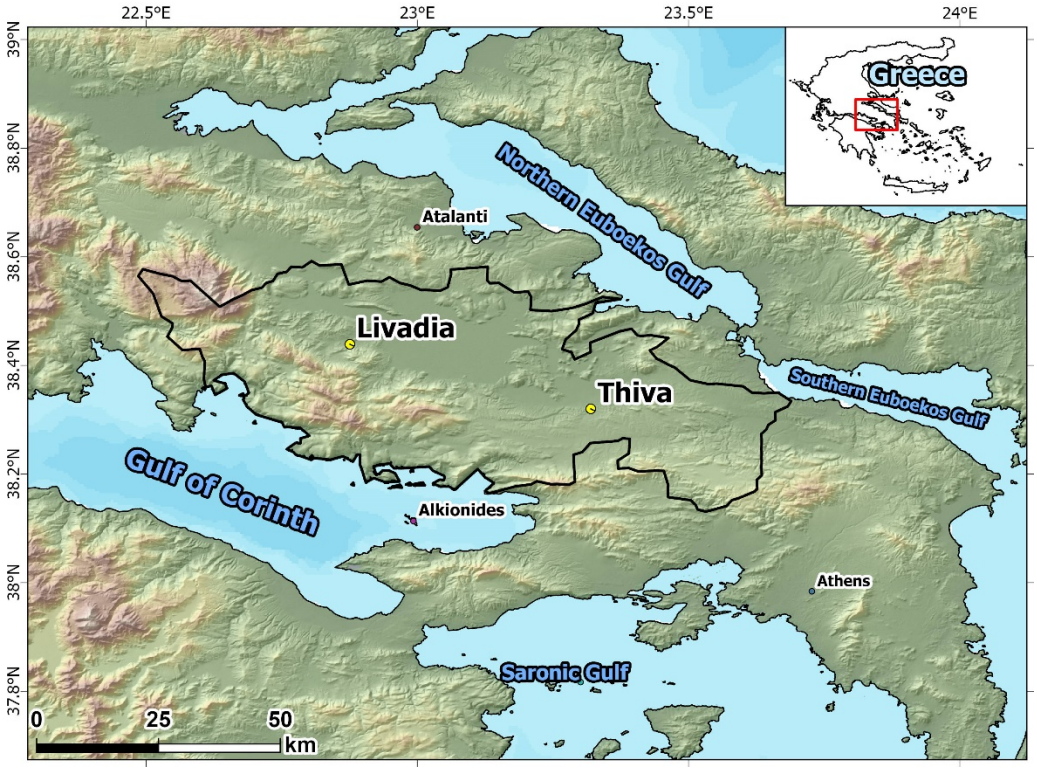

Figure I: The broader study area. Boeotia's borderline is marked as thick black line.

The primary objective of this thesis is to present an up-to-date seismic hazard model for Boeotia, with reduced epistemic uncertainties focusing on estimating key parameters, such as Peak Ground Acceleration (PGA), Peak Ground Velocity (PGV), and Spectral acceleration (Sa) values. Seismic hazard was conducted utilizing two methodologies: Probabilistic Seismic Hazard Assessment (PSHA) and scenario-based finite-fault stochastic ground motion simulation. In the context of PSHA, three seismotectonic models in the form of area sources were incorporated into the computational process to account for inherent variability. This crucial step aimed to mitigate epistemic uncertainties associated with the analysis. Additionally, numerous Ground Motion Prediction Equations (GMPEs) derived from Greek seismological data were employed within the computational framework. Overall, two software packages were utilized for PSHA, and their differences are also highlighted. The second approach entailed the inclusion of specific fault ruptures that could potentially pose a threat to Boeotia. These candidate faults underwent a selection process, considering factors, such as well-documented tectonic characteristics and past strong earthquakes. Furthermore, site effects were incorporated by considering the site classification for each grid point within the Boeotia region.

The spatial distribution of PGA and PGV values in Boeotia was obtained for return periods of 475 and 950 years. Furthermore, hazard curves were generated to illustrate PGA values among multiple return periods specifically for the locations of Livadia and Thiva. Lastly, elastic response spectra were constructed to depict Sa values for Livadia and Thiva. Focusing on PGA values for a return period of 475 years, it was observed that northern Boeotia adheres to the regulations specified in the Greek Building Code. Regarding the outcomes derived from the finite-fault stochastic ground motion simulation, it was determined that among the past earthquake scenarios, the seismic event that occurred near Thiva in 1914 generated the highest PGA values in Boeotia. The findings serve as a foundation for future research endeavors, enabling the evaluation of seismic risk in the region.

1.1 Ground deformation in Boeotia

Ground deformation can be caused by tectonic plate motions, volcanic eruptions or by earthquake occurrences. This type of deformation can be measured through the utilization of Global Navigation Satellite System (GNSS) stations or/and Synthetic Aperture Radar Interferometry (InSAR). GNSS can provide information about the three – dimensional ground deformation at a single point, which is the installed station. On the other hand, InSAR provides spatiotemporal information concerning the ground deformation by studying SAR acquisitions (satellite images) during two satellite paths (ascending and descending) in the same area but in different time.

The prefecture of Boeotia has a proximity to two active tectonic rifts, the GoC to the south and the Euboekos Gulf to the north (Figure I). The Gulf of Corinth is considered as one of the most active tectonic rifts worldwide (Rigo et al., 1996; Papadimitriou et al., 1999; Kaviris et al., 2017, 2021). A plethora of studies concerning the ground deformation of the GoC have been published, as the work of Avallone et al., 2004; Bernard et al., 2006 and Elias and Briole, 2018. Such studies have been conducted in the Euboekos Gulf as well (Ganas et al., 2016; Valkanou et al., 2021). Given that there is no published work concerning only the ground deformation in Boeotia, the latter will be examined through the use of Greek kinematic models. Various velocity fields have been proposed for Greece and the neighboring regions (Kreemer and Chamot-Rooke, 2004; Nyst and Thatcher, 2004; Hollenstein et al., 2006; Chousianitis et al., 2013, 2015; Briole et al., 2021). In this thesis, the 10 crustal kinematic blocks proposed by Briole et al. (2021) will be adopted, as the authors exploited data only on permanent stations.

Briole et al. (2021) analyzed velocity data from 282 Greek and 47 in other countries GNSS stations for the period 2000 – 2020. However, there was a significant increase in data during the period 2010 – 2020 due to more GPS station installations. Briole et al. (2021) removed the effect of earthquake occurrence in the data. Specifically, all events with Mw ≥ 5.3 and focal depth < 40 km were removed. The earthquake catalogue that was utilized in that study was the European Mediterranean Seismological Centre (EMSC, https://www.emsc-csem.org) catalogue. The uncertainties were evaluated by taking into account the velocity scattering in neighboring GNSS stations (distance smaller than 15 km). The results of the 329 GNSS (Greek and abroad) stations were adopted by Briole et al. (2021) and visualized through mean annual velocity vectors. The direction of the vectors is derived with respect to a stable European tectonic plate (Figure 1.1). The velocity within Boeotia is estimated 30 mm/yr in a SW direction. The velocity vectors inside the broader study area are among those with the highest magnitude (Figure 1.1), meaning that Boeotia is an area with intense ground deformation. The latter is reasonable concerning the continuous internal processes that exist in the broader region, i.e., the slab pull of Tethys oceanic plate (McKenzie, 1978; Doutsos et al., 1988; Jolivet et al., 1994) and the push concerning the North Anatolian Fault (Armijo et al., 1996, 1999).

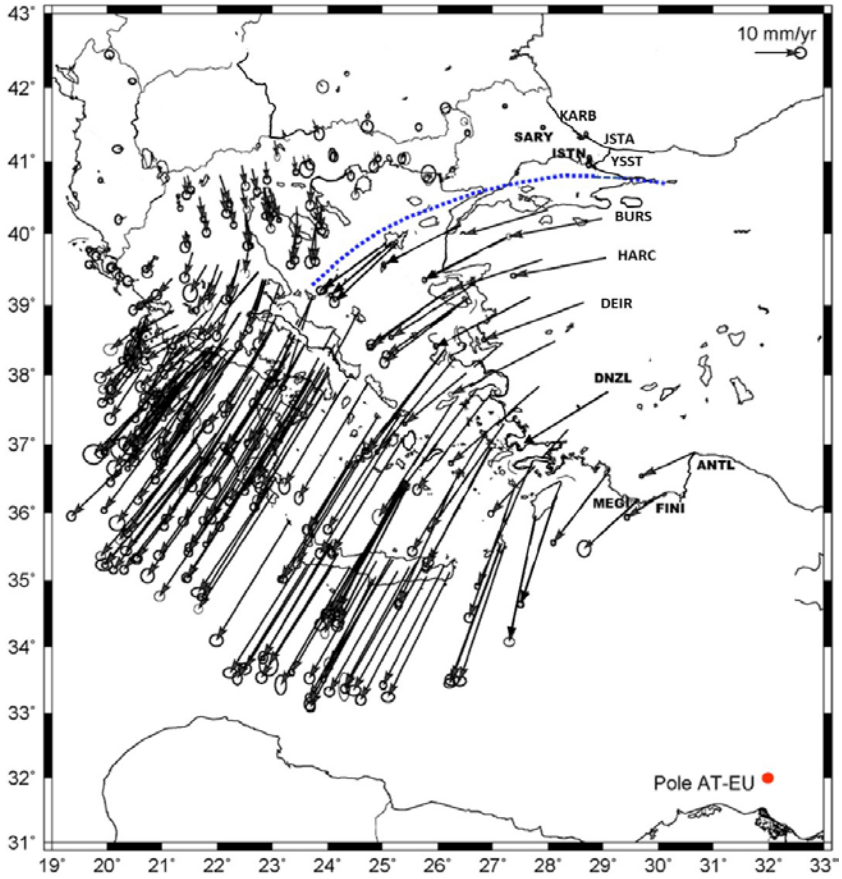

Figure 1.1: The annual mean velocity vectors that are derived from 329 GNSS stations are depicted with reference to the stable European plate. The blue dotted line represents the trace of the North Anatolian Fault. The red dot depicts the pole of rotation of Anatolia – Eurasia (modified by Briole et al., 2021).

In a next step, Briole et al. (2021) defined 10 crustal kinematic blocks where the velocity values, obtained from permanent GNSS stations within each block, have small variations. The boundaries of the blocks represent known ground deformation zones in most cases (letters in Figure 1.2). In

this thesis the coordinates of the barycenter of each block, the mean horizontal velocity value for both the N–S and E–W directions and the rates of rotation in respect to the Eurasian tectonic plate will be utilized (Table 1.1).

Boeotia is located within the Central Greece kinematic block, which is bordered to the south by the Central Aegean block, to the northwest by the Pindos block and to the northeast by the Northern Aegean block. All mentioned block's parameters are depicted in Table 1.1. Among the three blocks the most stable is the Central Aegean block. All blocks have a SW direction of rotation with respect to the Eurasian plate and the corresponding velocity values are depicted in Table 1.1. The relative movement between the barycenters' of Central Greece and Central Aegean kinematic blocks is equal to 10 mm/yr.

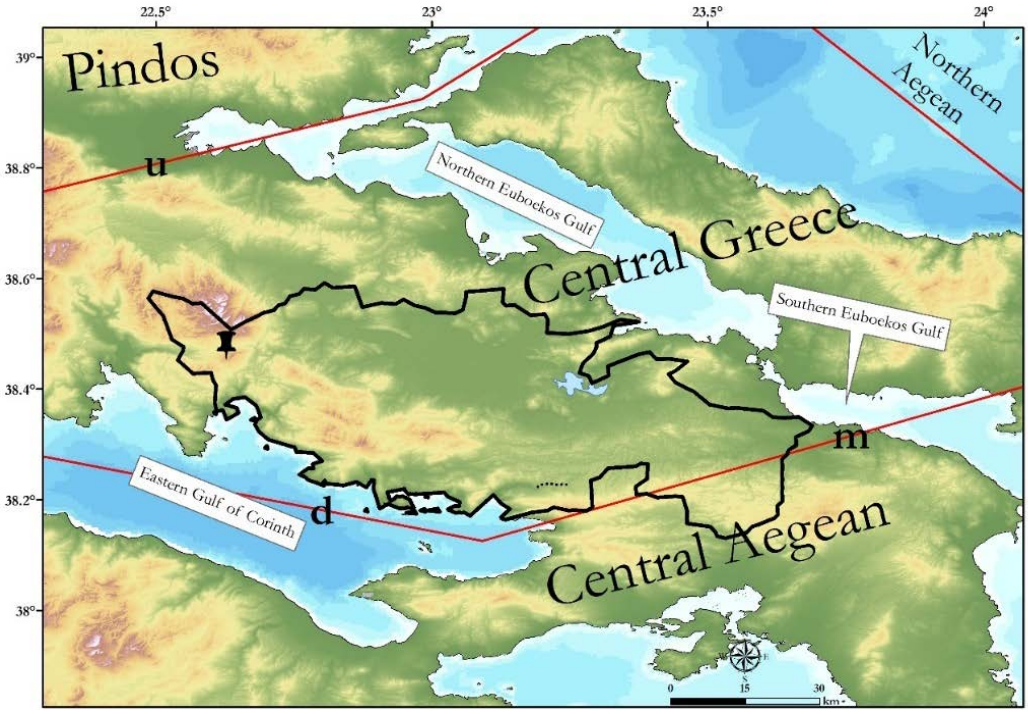

Figure 1.2: The crustal kinematic blocks of the broader study area, proposed by Briole et al. (2021) with hollow red polygons. The name of each polygon is written as a text. The black pin corresponds to the barycenter of the Central Greece block. The border depicted via a black line corresponds to the prefecture of Boeotia. The letters u, m and d represent known deformation zones (Briole et al., 2021). Specifically, u: the entrance of the Northern Euboekos Gulf to the NW and S of the Pindos block, d: Eastern Gulf of Corinth and m: through the Southern Euboekos Gulf with termination at the Eastern Gulf of Corinth close to the Kaparelli active fault (black dotted line within Boeotia).

Crustal kinematic block	LON (°)	LAT (°)	V_E (mm/yr)	V_N (mm/yr)	Ω (°/Ma)
Central Greece	22.628	38.477	11.7	-2.4	4.0
Central Aegean	23.994	37.414	8.1	-11.5	0.2
Pindos	21.874	39.602	20.1	7.1	2.6
Northern Aegean	25.718	38.943	11.7	-2.4	4.0

Table 1.1: The parameters that characterize each crustal kinematic block. LON and LAT stand for longitude and latitude, respectively, of the barycenter of each block. V_E and V_N is the mean horizontal velocity in the N–S and the E–W component. The Ω parameter is the rate of rotation in respect to the Eurasian tectonic plate (values by Briole et al., 2021).

1.2 Active tectonics of broader Boeotia area

The first step to initiate a seismic hazard study is to comprehend the active tectonics in the area under investigation. The Greek territory is world-widely known about its active tectonics that characterize the country as a "geological museum" for geoscientists to visit across the globe. In order to evaluate seismic hazard for the prefecture of Boeotia, it is required to know the seismicity and the active tectonic structures that have an impact on the study area. Even though the area of research is the prefecture of Boeotia, the active faults that will be examined will not be limited within Boeotia. The latter is justified as ground motions in terms of ground acceleration and velocity can be substantial even if the hypocenter of the earthquake is located outside, but not far from, Boeotia.

In general, Boeotia is not characterized by as many active faults as its adjacent areas, which are the Gulf of Corinth and the Euboekos Gulf. On the other hand, the Gulf of Corinth, as can be clearly seen in Figure 1.3, hosts a plethora of active tectonic structures. The faults in the study area have a general E–W direction. Obviously, there are deviations from this general strike, as faults with a NE–SW direction have been mapped on the southwestern coast of Boeotia (Figure 1.3), such as Antikira, EAN 2, Velanidia 1, Aspra Spitia and Kirfis faults (Ganas, 2022). The predominant type of faulting in the study area is normal, which is reasonable due to the active rifts of the Gulf of Corinth and of the Euboekos Gulf that surround Boeotia.

The goal is to select faults that were related with the occurrence of significant earthquakes in the broader Boeotia region. These faults will most likely be selected for the development of seismic scenarios regarding the scenario-based seismic hazard assessment. The selection criteria of the faults that are analyzed were: a) to be associated with at least one $M > 4.5$ event and b) to azimuthally cover the study area in order to compute strong ground motions within entire Boeotia.

At this point it is important to state that there are two available digital fault databases that have been proposed for the Greek region. The one that was released first is the **Gre**ek **Da**tabase of **S**eismogenic **S**ources (GreDaSS), proposed by Caputo and Pavlides (2013). This database contains individual and composite seismogenic sources, as well as areas of relevance, both online (http://gredass.unife.it) and offline, via a kml file to be inserted in Google Earth and other mapping software. The main goal of the database was to provide useful data for each source, for instance strike, dip, rake, maximum expected magnitude, slip rate and minimum–maximum depth. It must be mentioned that the latest update of the database was in July 2013 (version 2.0). The second digital database is the National Observatory of Athens Faults (NOAFaults), initially proposed by Ganas et al. (2013). Since then, the database has been constantly updated, with the latest version being the NOAFaults v4.0 (Ganas, 2022). The database can be viewed online via the ArcGIS online web application (https://arcg.is/04Haer) or can be downloaded via a kml file, similar to the GreDaSS database. The main difference between the two datasets is that the NOAFaults database includes more faults and provides more information about them. For example, there is available information on whether there was a strong earthquake that ruptured the fault, as well as field photos etc.

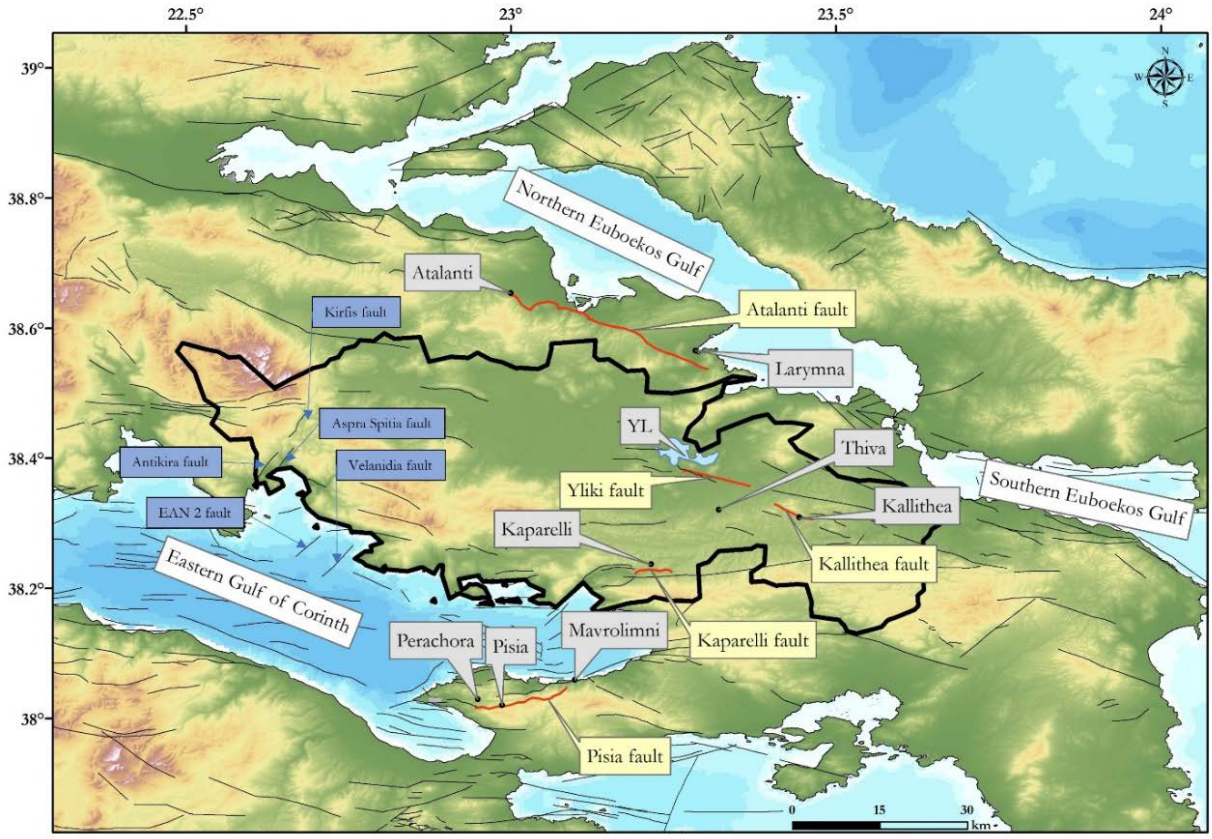

Figure 1.3: The faults in the broader Boeotia area (by NOAFaults v4.0, Ganas, 2022). The selected faults for further analysis are marked in red and their names are depicted via yellow labels. The border depicted via a black line corresponds to the prefecture of Boeotia. YL: Yliki Lake.

1.2.1 The Atalanti fault zone

The fault of Atalanti (Figure 1.4) initiates 500 m SSE of Atalanti town and ends approximately 3.5 km SE of Larymna town. It is part of the Sperchios–Chalkis Fault System and contributes to the crustal extension accommodated in the Euboekos Gulf since 3.6 million years in the Late Pliocene–Quaternary (Kranis and Papanikolaou, 2001; Papanikolaou and Royden, 2007). It is a normal fault with a general direction of 120° and dipping 60° to the NE, according to the NOAFaults database (Ganas, 2022). However, it is noted that Karastathis et al. (2007) have estimated a dip in the range of [45°, 49°], whereas Savvaidis et al. (2012) proposed a change in the fault's dip, from 60° (SW) to 80° (NE). The mean slip rate has been computed by Ganas et al. (1998) equal to 0.4 mm/yr. The total length of the fault is approximately 32 km meaning that if the entire tectonic structure ruptured, an Mw = 6.9 earthquake would be produced according to the database proposed by Ganas (2022). The latter is in accordance with the well–known 1894 earthquake sequence that occurred due to the rupture of Atalantis fault. The sequence hosted two M6+ events with one week separation. The first event of the sequence was the 20 April 1894 M = 6.7 event that was related to a 15 km rupture. It had an important contribution to the genesis of the second earthquake on 27 April in the same year due to stress Coulomb transfer (Ganas et al., 2006). However, the maximum expected magnitude was re–estimated using the empirical relations proposed by Papazachos (1989); Wells and Coppersmith (1994) and Thingbaijam et al. (2017) (Table 1.2).

Figure 1.4: The trace of Atalanti fault along the mountain front, depicted by white arrows. The field photography is facing the SW (modified by Ganas et al., 2006).

Empirical equation	Mw
Papazachos (1989)	6.6
Wells and Coppersmith (1994)	6.9
Thingbaijam et al. (2017)	6.7

Table 1.2: Maximum expected magnitude if the whole 32 km length of the Atalanti fault ruptures.

1.2.2 The Pisia fault zone

The Pisia fault (Figure 1.5) initiates 1.5 km SSW of Perachora town and ends 9 km east of Pisia town, close to Mavrolimni. It has a total length of approximately 14 km. The maximum expected magnitudes according to different empirical relations are depicted in the Table 1.3. It was first mapped by Jackson et al. (1982) after the Alkyonides earthquake sequence, the major shock of which occurred on 24/02/1981 with Mw = 6.7. The Pisia fault is a normal north–dipping tectonic structure with a direction and dip equal to 70° and 45°, respectively (Ganas, 2022). In addition, it has a co–seismic slip and slip rate equal to 1.2 mm and 2.3 mm/yr, respectively.

According to the work of Papazachos et al. (1984) and Hubert et al. (1996), the Pisia Fault was activated during the occurrence of the second major aftershock of the 1981 sequence (the 25/02/1981 Mw = 6.4 event). Initially, Jackson et al. (1982) associated the 25/02/1981 event with a longer structure, which did not fit well in the modeling done by Papazachos et al. (1984); Vita-Finzi et al. (1985) and Hubert et al. (1996). Jackson et al. (1982) suggested that an offshore fault produced the first major shock of the 1981 sequence (the 24/02/1981 Mw = 6.7 event). However, it seems that the causative tectonic structure extended onshore as proposed by Abercrombie et al. (1995), whose conclusions agree with the ones of Papazachos et al. (1984); Vita-Finzi et al. (1985) and Hubert et al. (1996). The fault database of Caputo and Pavlides (2013) was not taken into consideration because the Pisia fault does not exist with its exact location. Instead, the database depicts a large seismogenic source crossing the land and sea south of the border of Boeotia (Figure 1.6). Also, the causative fault of the 24/02/1981 Mw = 6.7 event will not be analyzed in this work due to the high uncertainties that surround the location of the tectonic structure.

Figure 1.5: Part of the Pisia fault trace (Ganas, 2022).

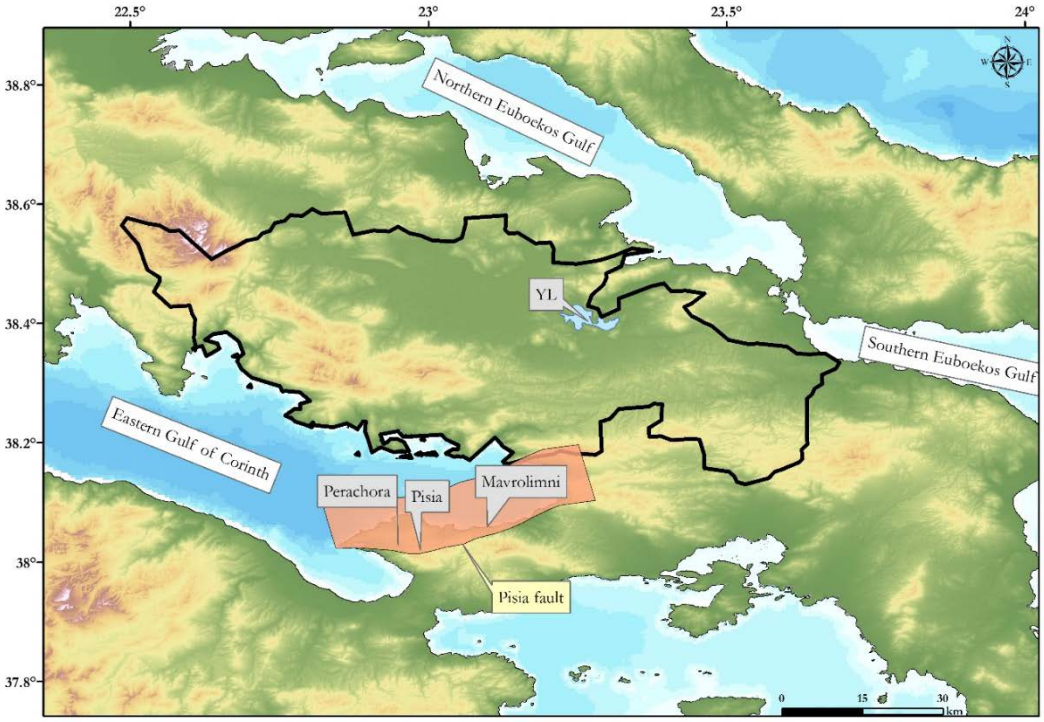

Figure 1.6: The Pisia seismogenic source (Caputo and Pavlides, 2013).

Empirical equation	Mw
Papazachos (1989)	5.9
Wells and Coppersmith (1994)	6.4
Thingbaijam et al. (2017)	6.1

Table 1.3: Maximum expected magnitude if the whole 14 km length of Pisia fault ruptures.

1.2.3 The Kaparelli fault zone

The westernmost part of the Kaparelli fault is located 2.7 km SW of Kaparelli village and terminates 3.2 km SE of it with a total length of 5.5 km (Figure 1.7). According to Ganas, 2022, the location reliability of the fault is precise. Concerning the kinematics of the structure, it is a normal fault with a south dip direction (Jackson et al., 1982; Papazachos et al., 1984; Hubert et al., 1996; Caputo and Pavlides, 2013; Ganas, 2022) striking almost E–W and dipping 50° (Ganas, 2022). The fault is associated with the second major aftershock of the 1981 Alkyonides sequence that occurred on 04/03/1981 with Mw = 6.3 (Papazachos et al., 1984; Papazachos and Papazachou, 2003). According to Kokkalas et al. (2007), the co–seismic slip is 0.7–1.0 mm and the slip rate is 0.3 mm/yr (Ganas, 2022). Caputo and Pavlides (2013) have proposed significantly different fault characteristics, such as length, strike and co–seismic slip, compared to the NOA faults database. However, these data have not been updated since 2011 and some fields within the attribute table have a "to be filled" statement in the "reference" column. Concerning the maximum expected magnitude, both databases propose a result within the range of Mw = 6.2–6.3, however, in the Table 1.4 the results estimated in this thesis using the empirical relations are depicted. These values cannot be taken into account, because they are considerably smaller than the magnitude of the earthquake that ruptured the fault.

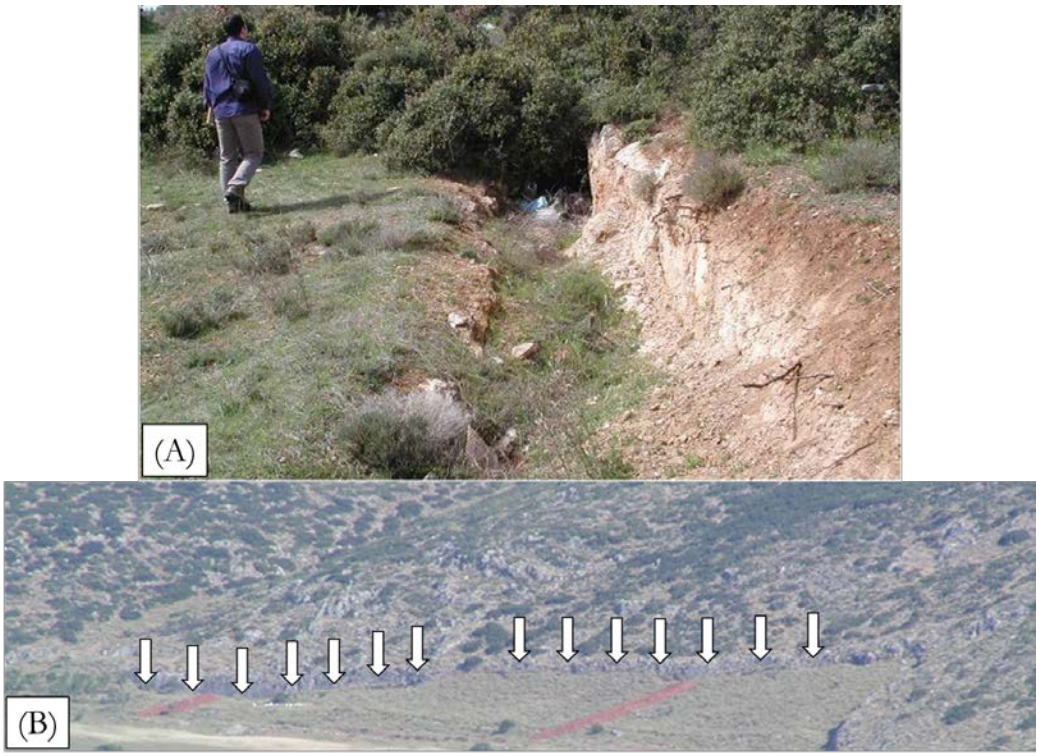

Figure 1.7: Part of the Kaparelli fault's trace in a closeup view (A) and a larger–scale field photography depicting the fault's trace with white arrows (B) (modified by Ganas, 2022).

Empirical equation	M
Papazachos (1989)	5.1
Wells and Coppersmith (1994)	5.5
Thingbaijam et al. (2017)	5.4

Table 1.4: Maximum expected magnitude if the whole 5.5 km length of the Kaparelli fault ruptures.

1.2.4 The Kallithea fault zone

The fault of Kallithea has a proximity to Thiva, a major town in Boeotia region in terms of population (32,410 residents, ELSTAT, 2021), agriculture and economics. The fault has a total length of 6 km (Elias et al., 2021; Ganas, 2022; Kaviris et al., 2022a). This tectonic structure is considered a segment of the Kallithea and Mavrovouni fault zone that could produce an event in the range of [6.2, 6.4] (Sboras et al., 2010; Elias et al., 2021). The Mavrouvouni fault is located SE of the Kallithea fault. Kallithea fault is a normal neotectonic structure with a minor seismic activity (Figure 1.8). However, it turned out to be the causative fault of the 02/12/2020 Mw = 4.6 earthquake (Elias et al., 2021; Kaviris et al., 2022a).

Elias et al. (2021) supported that the Kallithea fault was activated during the Mw = 4.6 event occurrence through InSAR and seismological methods. The InSAR results supported the activation of a structure close to the Kallithea village with a strike approximately of N120°E (Figure 1.9). The focal mechanism computed through moment tensor inversion had strike/dip/rake equal to 106°/31°/-81° (Elias et al., 2021).

In the NOA Faults database (Ganas, 2022), the location of the fault is considered precise. However, kinematic properties were not adopted, since the corresponding fields have not been updated with the results of Elias et al. (2021). Concerning the GreDaSS database (Caputo and Pavlides, 2013) there is no specific location of the aforementioned fault. Lastly, the maximum expected magnitude computed using the empirical relations is presented in Table 1.5. The largest value (Mw = 5.9) is obtained by applying the relationship of Wells and Coppersmith (1994). However, historical data report earthquakes of magnitude Mw ≥ 6.0 in Thiva (Kaviris et al., 2022a). This implies that the full seismic potential of the faults in the vicinity of Thiva has not yet been revealed.

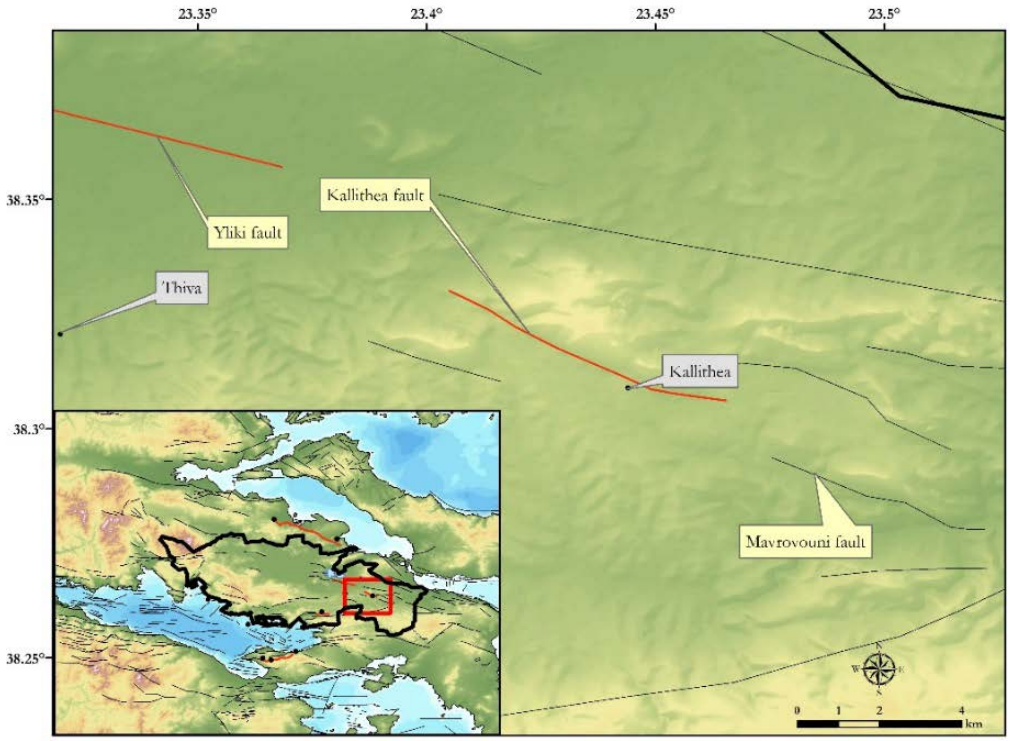

Figure 1.8: The Kallithea and the Mavrovouni faults. The bold black line denotes the borders of Boeotia.

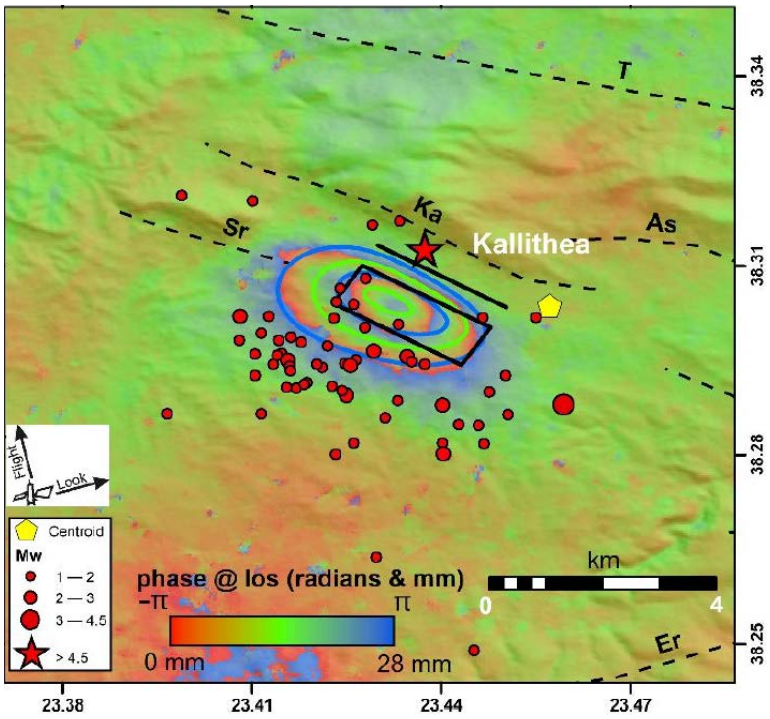

Figure 1.9: InSAR results for the 2 December Mw = 4.6 mainshock, adopted by Elias et al. (2021). The black line depicts the trace of the Kallithea fault and the black rectangle the rupture plane. In addition, the mainshock is depicted as a star along with the aftershocks shown as circles. The yellow polygon marks the seismological centroid (Elias et al., 2021).

Empirical equation	Mw
Papazachos (1989)	5.2
Wells and Coppersmith (1994)	5.9
Thingbaijam et al. (2017)	5.5

Table 1.5: Maximum expected magnitude if the whole 6 km length of the Kallithea fault ruptures.

1.2.5 The Yliki fault zone

The Yliki fault is a structure that is located ~15 km west of the Kallithea fault. In the NOAfaults database there are 4 different faults under the name of Yiliki (Yliki 2, 3, 4 and 5), all located south of the Yliki lake as depicted in Figure 1.10 (Ganas, 2022). Regarding the seismicity related to the Yliki fault zone, there was a seismic swarm that lasted from July to October 2021.

Three events with Mw > 4.0 occurred during the July–October 2021 sequence. The first was the 11/07/2021 Mw = 4.2 earthquake, the second event that occurred on 20/07/2021 had the same magnitude and the last important earthquake was the 02/09/2021 Mw = 4.1 event. Kaviris et al. (2022) relocated all events and interpreted the activated structures in the study area using seismic cross–sections. However, the July–October sequence had significantly larger focal depths compared to the December 2020 Kallithea sequence, which resulted in the absence of surface deformation. The latter raises the level of the uncertainty when pinpointing the causative fault. Kaviris et al. (2022) mentioned that the Yliki fault could be the activated structure that produced the Mw > 4.0 events if it was extended to the east, as was also proposed by Sboras et al. (2010).

In this thesis, the fault proposed by Kaviris et al. (2022) will be adopted as it was updated utilizing focal mechanisms and a relocated catalogue. The initial location of the fault was proposed by

Tsodoulos et al. (2008) and the inferred burial eastern extension was added by Kaviris et al. (2022). It has a total length of 6 km and a strike equal to 80° at the western part and 115° at the eastern one. In addition, the fault is dipping 60° to the south. Neither Ganas (2022) nor Caputo and Pavlides (2013) have sufficient information concerning the Yliki fault, strengthening the option to adopt the model proposed by Kaviris et al. (2022). Given the length of the fault, the maximum expected magnitude is estimated utilizing the aforementioned empirical relations. The results that are depicted in Table 1.6 are identical to the ones in Table 1.5, given that both the Yliki and Kallithea faults have the same length. However, as in the case of the Kallithea fault, the results obtained by the implementation of the empirical relations will not be adopted because they are lower than the maximum expected magnitude that is reported by historical records for the Thiva town (Mw ≥ 6.0, Kaviris et al., 2022).

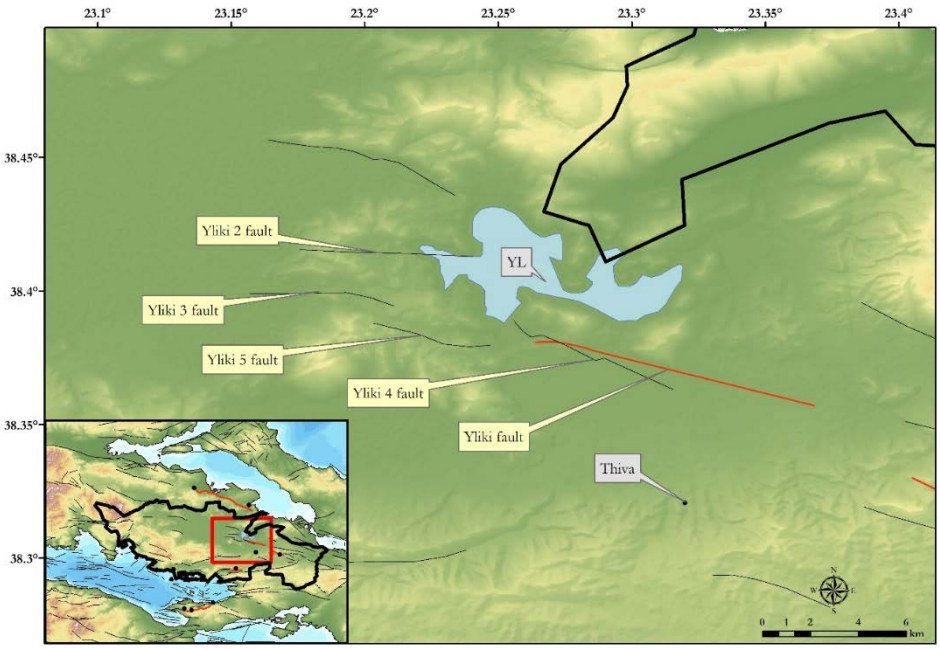

Figure 1.10: The Yliki fault, proposed by Kaviris et al. (2022), in red and all the Yliki faults, according to NOAFaults (Ganas, 2022).

Empirical equation	M
Papazachos (1989)	5.2
Wells and Coppersmith (1994)	5.9
Thingbaijam et al. (2017)	5.5

Table 1.6: Maximum expected magnitude if the whole 6 km length of the Yliki fault ruptures.

1.3 Seismicity of Boeotia

In a seismic hazard study, it is important to identify the seismicity of the investigated area because the results in terms of ground motion can be qualitatively expected. Earthquake catalogues should be examined in order to initiate a seismicity study. These catalogues include the spatial and temporal parameters of earthquakes, such as the origin time, the epicentral coordinates, the focal depth, the magnitude and, in some cases, the focal mechanism for each earthquake. The characteristics of an earthquake catalogue depend on the goal it is intended to serve. For example, a catalogue that also includes small magnitudes is exploited in seismotectonic studies to map active

tectonic structures, whereas a catalogue used for seismic hazard studies will consist of earthquakes upon a certain threshold magnitude. Finally, catalogues are classified as "historical" or "instrumental" depending on their time span coverage. Herein, the term historical seismicity is used for earthquakes that occurred prior to the installation of seismological stations, i.e., before 1900, while the term instrumental seismicity will refer to earthquakes taking place after 1900.

1.3.1 Historical seismicity of Boeotia

The historical seismicity data of the study area (22.297°E–24.070°E and 37.827°N–39.052°N) were adopted from the Seismic Hazard Harmonization in Europe Earthquake Catalogue (SHEEC), which is compiled by Stucchi et al. (2013). All magnitudes are converted in the Mw scale. The **E**uropean **P**re**I**nstrumental Earthquake **CA**talogue (EPICA), proposed by Rovida et al. (2022), was also investigated, but includes the same events and identical earthquake parameters. SHEEC exploited macroseismic data, available in the European Archive of the Historical Earthquake Data (AHEAD) database. These data are derived from historical records, studies and macroseismic databases. Furthermore, the records are reliable and have been verified by the Seismology and Earthquake Engineering Research Infrastructure Alliance for Europe (SERA). However, it is worth noting that several earthquakes were imported from the Greek historical catalogue of Papazachos and Papazachou (2003). Specifically, all pre–11th century events were added from Papazachos and Papazachou (2003) because SHEEC includes earthquakes after 1000 CE. Thus, the final catalogue contains 53 earthquakes for the broader Boeotia (Figure 1.11) with magnitudes ranging from 5.9 to 7.0. Regarding the origin time, the oldest event occurred in 480 CE and the youngest in 1894. Finally, in accordance with the spatial distribution of the epicentres, it is observed that the majority of them are located in the Eastern Gulf of Corinth, mainly on its southern mainland (Figure 1.11). On the contrary, 7 earthquakes are being hosted within Boeotia, while 2/7 events are located close to Thiva (Figure 1.11).

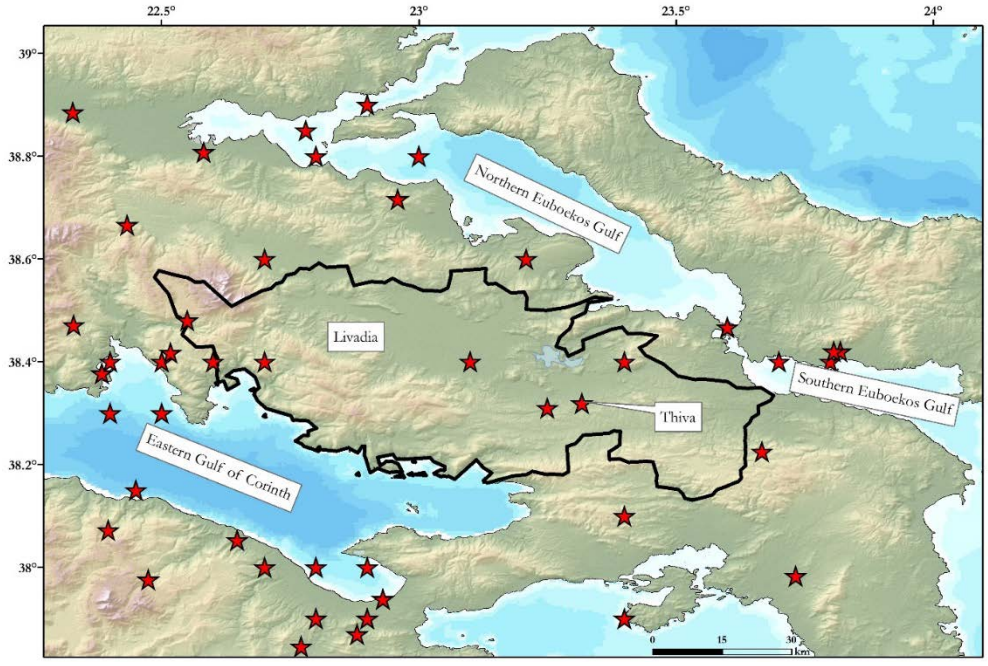

Figure 1.11: Spatial distributions of the 53 historical earthquakes in the broader study area. Data were derived from SHEEC and Papazachos and Papazachou (2003) historical earthquake catalogues (Papazachos and Papazachou, 2003; Stucchi et al., 2013).

1.3.1.1 The 1894 earthquake sequence

Regarding the Atalanti area, only a few earthquakes have occurred north of the city according to the historical seismicity catalogue (Figure 1.11) and the research of Makropoulos and Kouskouna (1994). However, a M = 7.0 earthquake took place on 27/04/1894 at 19:21 local time (Papazachos and Papazachou, 2003). The aforementioned event was preceded by a devastating M = 6.6 foreshock that occurred on 20/04/1894 (Figure 1.12), with a temporal gap of one week between the two earthquakes. No other significant earthquake has been recorded after the reported ones near Atalanti, reinforcing the argument that strong earthquakes in the area have a large return period. In the work of Papazachos and Papazachou (2003) it is stated that all magnitudes are estimated in the Mw scale after applying macroseismic magnitude conversion according to empirical relations. Other epicentral solutions of the two earthquakes have been proposed by estimating different macroseismic intensities (Karnik, 1971; Shebalin et al., 1974; Ambraseys and Jackson, 1990; Makropoulos and Kouskouna, 1994; Papazachos and Papazachou, 1997).

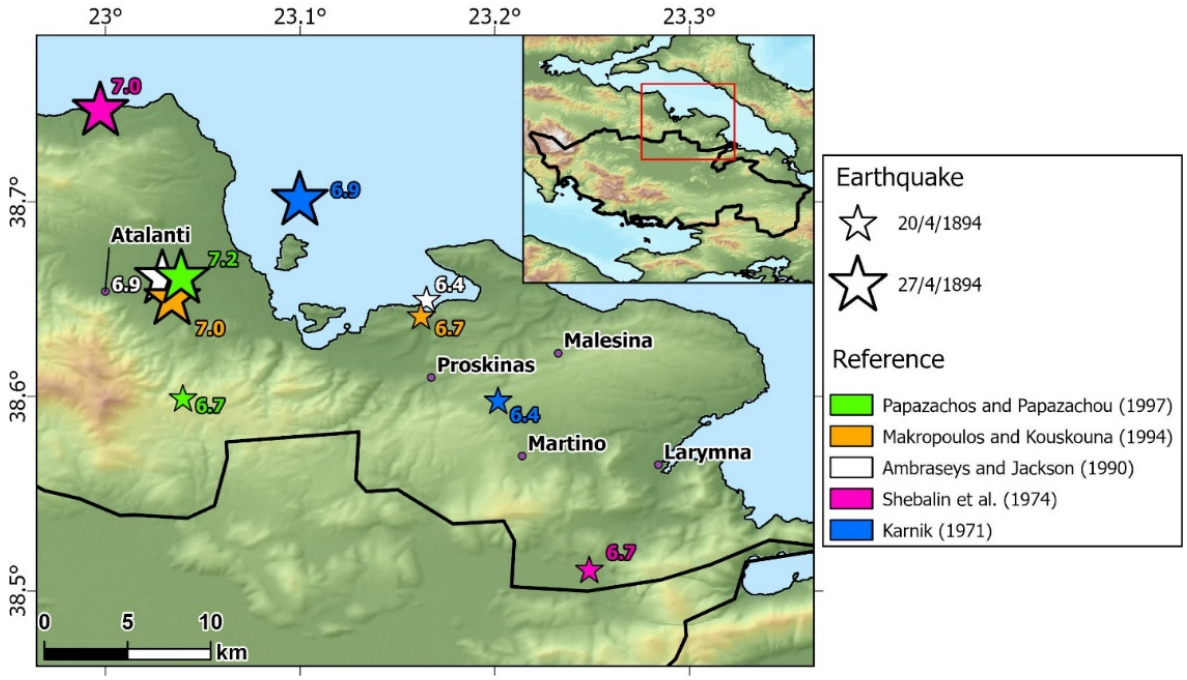

Figure 1.12: The foreshock (small star) and the mainshock (big star) of April 1894. The epicenters of 5 studies for these events are plotted (each pair indicated with different color). Every epicenter's magnitude is labelled on the map.

Although different solutions have been proposed, the significant damage caused by the two earthquakes is undeniable. The area of maximum macroseismic intensity includes the area between Larymna and Atalanti (Papazachos and Papazachou, 2003). The villages of Proskinas, Malesina and Martino suffered the greatest damage from the earthquakes, where the inhabitants felt the ground sinking beneath their feet. In Malesina the Monastery of St. George was destroyed and in Larymna the church of St. Nicholas collapsed. The overall consequences of the two earthquakes were 255 casualties and the destruction of 3,783 houses in 69 settlements. Sketches have been created after these events, representing the damage at a church and the survivors at Atalanti (Figure 1.13 A and B, respectively). The earthquake was felt in Athens according to Ambraseys and Jackson (1990), Makropoulos and Kouskouna (1994) and Papazachos and Papazachou (2003). In fact, Makropoulos and Kouskouna (1994) report that two earthquake tremors were felt in Athens, the first lasting 3–4 s and the second 5–7 s. They also report that cracks were observed in some

houses. Finally, Kouskouna et al. (2020) provide a diagram illustrating the state of preparedness of society for the occurrence of the two earthquakes and the secondary phenomena they caused (Figure 1.14).

Figure 1.13: The damage in the main church (A) and the survivors (B) in Atalanti (Albini and Pantosti, 2004).

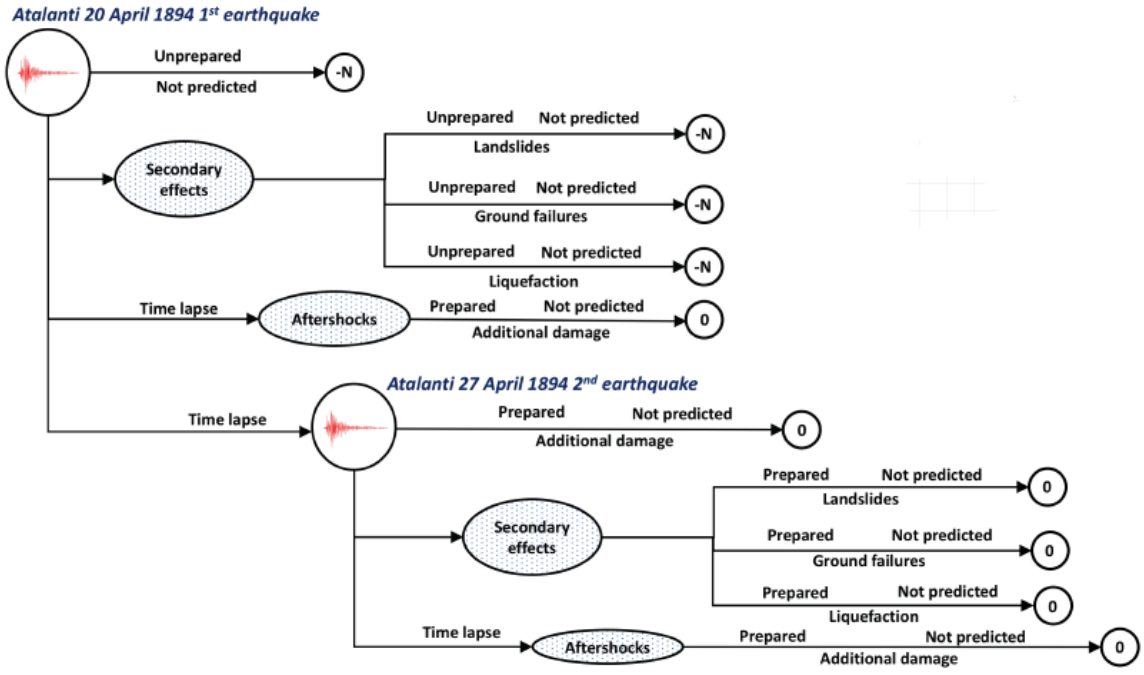

Figure 1.14: Risk communication and the secondary phenomena of the events (Kouskouna et al., 2020).

Valuable material for the earthquake sequence was provided by Skouphos (1894) and Mitsopoulos (1895). A major drawback that has been reported is that the effects of the two earthquakes are cumulative. In theory, Albini and Pantosti (2004) tried to resolve this issue, but the magnitudes of the two earthquakes they estimate are considerably smaller than those of the other studies. More specifically, they estimate magnitudes of 6.4 and 6.5 for the foreshock and the mainshock,

respectively. The spatial distribution of the Intensity Data Points (IDPs) proposed for each event by Albini and Pantosti (2004) are depicted in Figure 1.15.

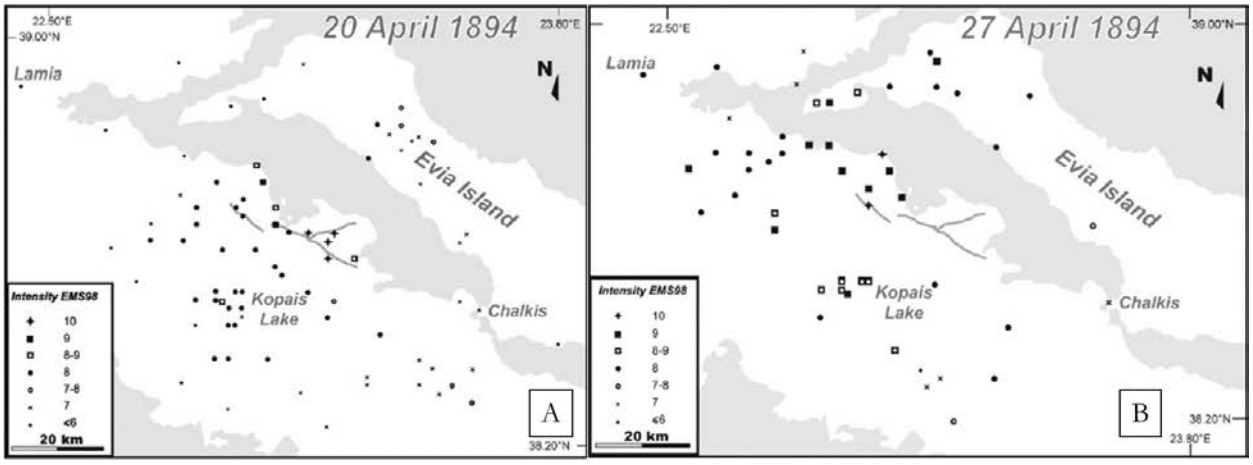

Figure 1.15: IDPs maps for the foreshock (A) and mainshock (B). Source: Albini and Pantosti (2004).

1.3.1.2 Historical seismicity of Thiva

The broader Thiva area is characterized by moderate seismicity. According to the reports of Jordanus, as mentioned by Kaviris et al. (2022), there were house collapses during 1321-1323. Considering the historical catalogue that is used in this thesis, a Mw = 6.0 earthquake took place in 1321 (Figure 1.16), but without aftershocks. On 18/08/1853 an earthquake occurred, whose magnitude varies according to different studies (Mw = 6.5 from Papazachos and Papazachou, 2003; Mw = 6.0 by Stucchi et al., 2013 and Mw = 6.2 by Kaviris et al., 2022) (Figure 1.16). Thiva with a population of was destroyed by this earthquake, having at that time 4400 inhabitants. The water supply system was interrupted for 24 hours, and the springs dried up for a few days (Papazachos and Papazachou, 2003). The earthquake caused 11 fatalities and 6 injuries (Kaviris et al., 2022a). Intense secondary effects were also caused, for example flooding on the beaches of the South Euboekos Gulf, rockfalls on a mountain 18 km north of Thiva and liquefaction near Atalanti town (Kaviris et al., 2022a). This event was followed by a strong aftershock (Mw = 6.3), according to Papazachos and Papazachou (2003), on 02/09/1853 (Figure 1.16), due to which the already damaged buildings collapsed. There was only 1 casualty because the already frightened residents stayed in the open (Papazachos and Papazachou, 2003; Ambraseys, 2009; Kaviris et al., 2022a). Thiva was rebuilt in 1860 and the houses had more space between them (Kaviris et al., 2022a). However, the 23/05/1893 Mw = 6.2 event (Figure 1.16) destroyed 100 houses and 800 were deemed uninhabitable. Consequently, 900 out of 1200 houses ceased to be functional (Papazachos and Papazachou, 2003; Kaviris et al., 2022a).

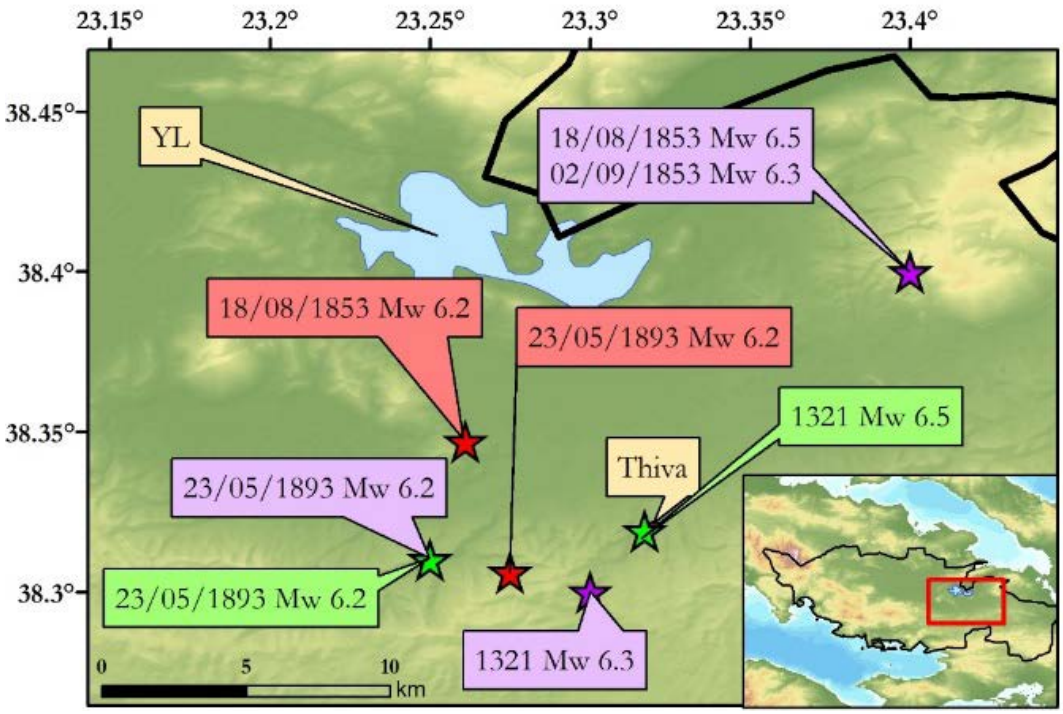

Figure 1.16: Epicenters of historical earthquakes in the Thiva area, as reported by Papazachos and Papazachou (2003) (in purple), Stucchi et al. (2013) (in green) and Kaviris et al. (2022) (in red).

1.3.2 Instrumental seismicity of Boeotia

The term "instrumental" corresponds to the installation commencement of seismological stations in order to record earthquakes. Every information that was stated in the previous chapter was strictly based on macroseismic data and historical reports (such as the Jordanus' reports on the 1321 Thiva event, Kaviris et al., 2022). Instrumental earthquake catalogues initiate in 1900. In this thesis, the catalogue proposed by Makropoulos et al. (2012) for Greece and adjacent areas is utilized to describe the seismicity of the study area. The threshold magnitude of the Makropoulos et al. (2012) catalogue was set to Mw = 4.1 (Ms = 4.0) in order to be exploited in seismic hazard studies. However, there is one drawback in the original catalogue, which is the time coverage, as it covers the period until 2009. This has an impact in both the characterization of the area's seismicity and the evaluation of seismic hazard. This obstacle was overcame due to the temporal expansion of the Makropoulos et al. (2012) catalogue to account for events for the period 2010–2019 (for details, see chapter 2).

In total 395 earthquakes are included in the catalogue for the broader Boeotia area (Figure 1.17). Similar to the historical seismicity map (Figure 1.11), the vast majority of the events are located at the eastern Gulf of Corinth, highlighting the seismotectonic importance of the area. More specifically, the eastern GoC hosts ~110 out of the 395 events (~30% of the total catalogue). On the contrary, Euboekos Gulf hosts only ~30 earthquakes (~8%). Boeotia is characterized by intermediate seismicity, when compared to the Gulf of Corinth and the Euboekos Gulf as ~70 among the 395 events recorded within Boeotia's borderline (Figure 1.17), covering the ~18% of the catalogue. It must be noted that there is a lack of earthquake occurrences close to Livadia and almost all the western part of Boeotia. The latter is crucial as ground motions in the aforementioned parts of Boeotia tend to be lower than the remaining study area.

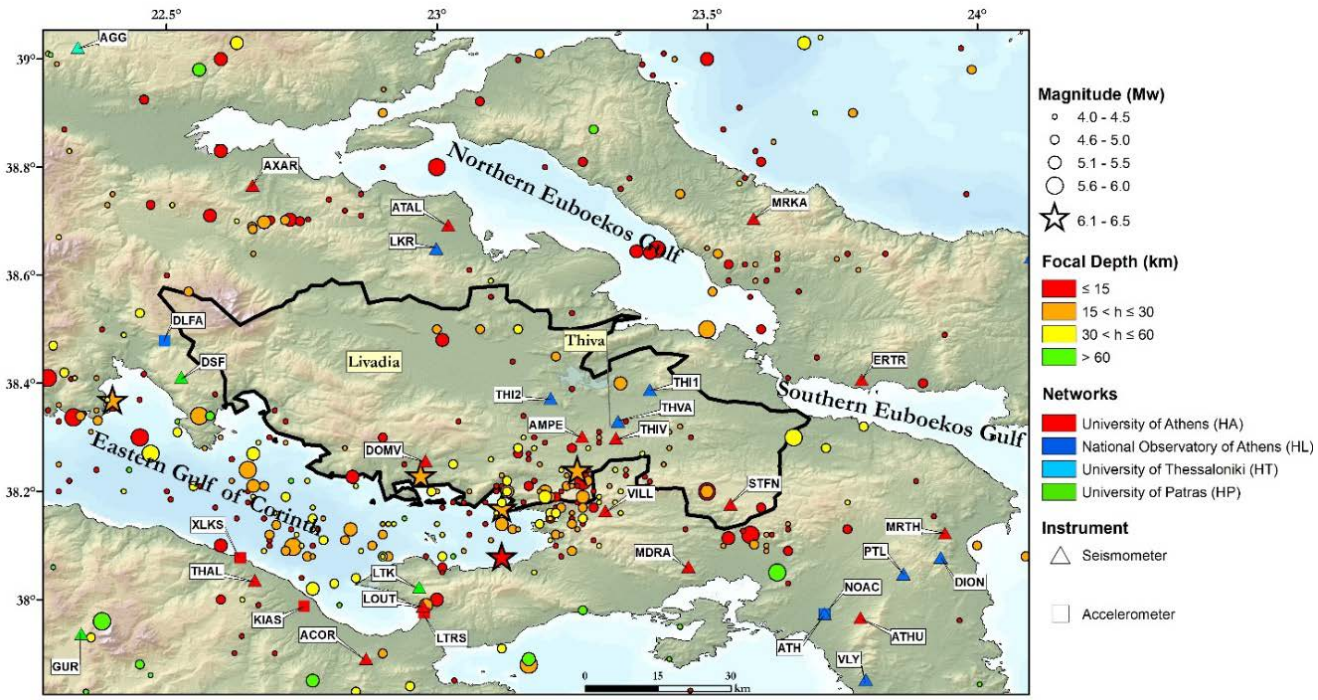

Figure 1.17: Instrumental seismicity of the study area. In addition, the seismological stations that are active in 2022 are presented with symbols according to their network and the type of instrument. Epicentres are from Makropoulos et al. (2012) extended up to 2019.

The number of earthquakes per focal depth bin is depicted in Figure 1.18a, whereas the respective graph for the earthquake magnitude is presented in Figure 1.18b. Concerning Figure 1.18a, most seismic events have a focal depth of about 10 km. The latter is possibly due to standard focal depth solutions that exist because of depth uncertainties, especially during the first decades covered by the catalogue. Continuing to Figure 1.18b, almost 1/3 of the catalogue consists of earthquakes of magnitude 4.1. The second higher peak is observed for Mw = 4.4, whereas less than 15% of the earthquakes of the catalogue have magnitudes Mw > 5.0.

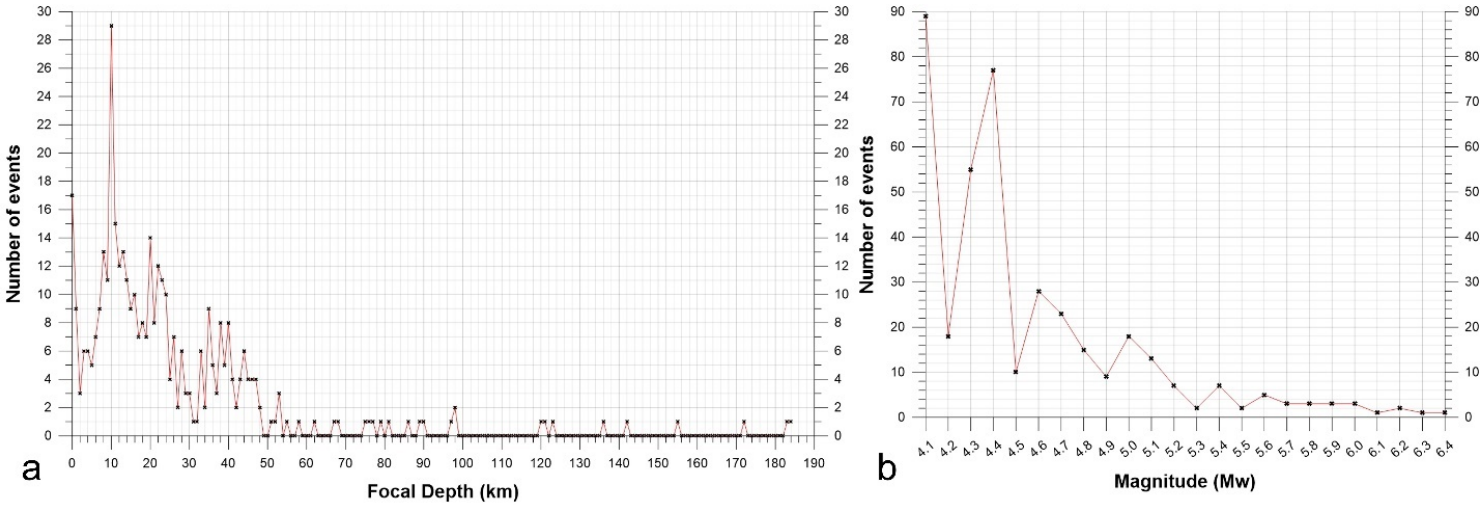

Figure 1.18: Number of earthquakes as a function of focal depth (a) and Mw (b).

1.3.2.1 The 1914, 1917 Thiva earthquakes

A destructive earthquake struck Thiva on 17/10/1914 causing significant damage at the town and the neighboring villages (Kaviris et al., 2022a). No foreshocks were reported, however, aftershocks inflicted more damage in the already stricken area and the seismicity was migrating to the west (Kaviris et al., 2022a). The epicenter is located SE of Thiva, at a close distance (Figure 1.19), which is in agreement with the solution proposed by Eginitis (1916) and Goulandris (1916). It must be noted that the mainshock did not cause any surface ground deformation, such as ground ruptures and cracks (Eginitis, 1916; Kaviris et al., 2022a). After three years, on 23/09/1917 an earthquake took place close to Thiva (Shebalin et al., 1974; Kaviris et al., 2022a). However, this event is not included in the earthquake catalogue of Makropoulos et al. (2012), as it is also stated in the work of Kaviris et al. (2022). At least 37 aftershocks occurred until the end of 1917. The epicenter of the event is illustrated in Figure 1.20. Information regarding the earthquake's parameters is presented in Table 1.7.

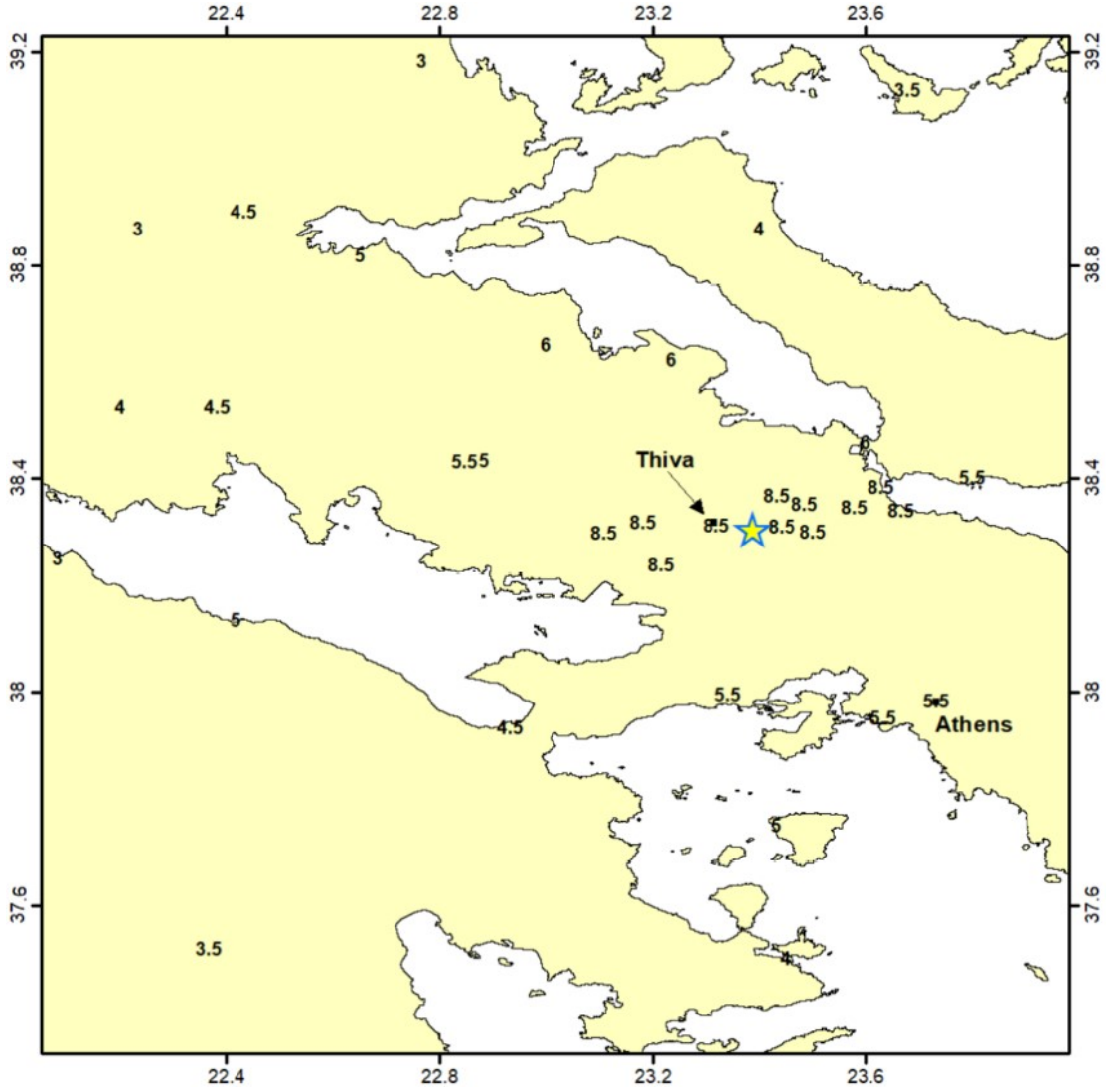

Figure 1.19: Spatial distribution of macroseismic intensities of the 1914 mainshock. Source: Kaviris et al. (2022a).

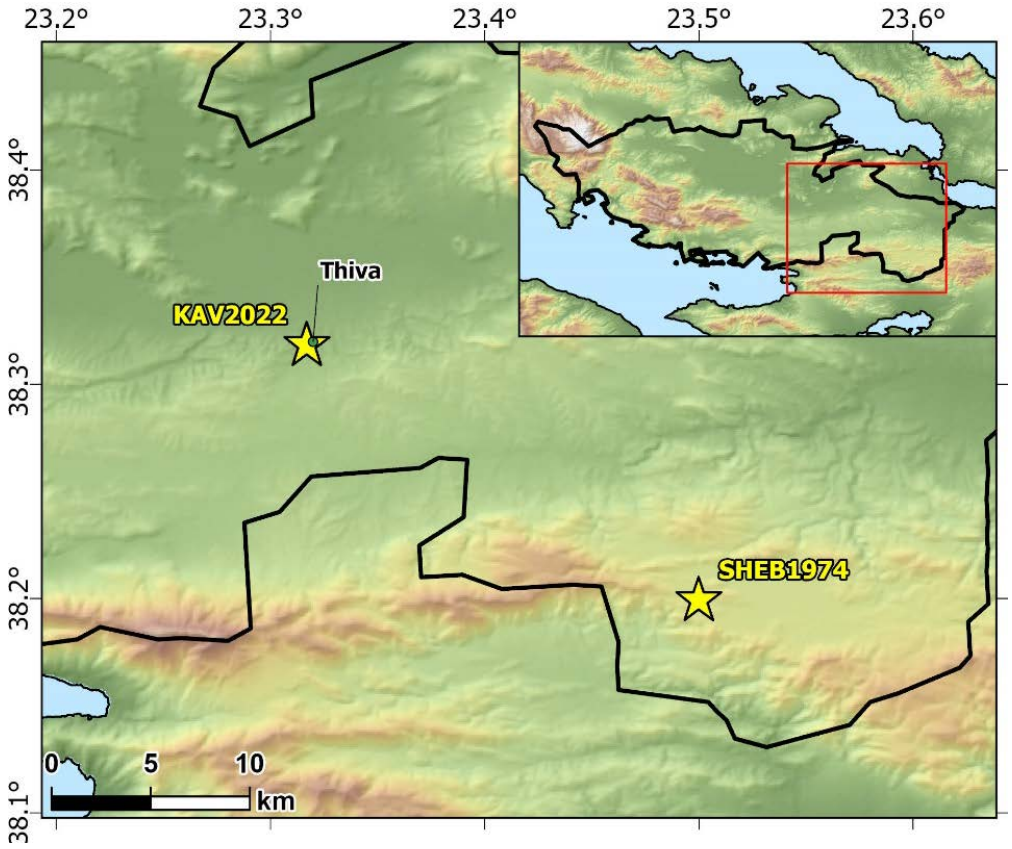

Figure 1.20:The epicenter of the 1917 Thiva earthquake, according to Shebalin et al. (1974) - SHEB1974 and Kaviris et al. (2022a) - KAV2022.

Source	Date	I_0	Lat (°N)	Lon (°E)	U_{epi} (km)	Mw	D (km)	IDPs
Kaviris et al. (2022a)	1914-10-17	8-9	38.306	23.388	6.7	6.0 ± 0.1	8 ± 1	62
Makropoulos et al. (2012)		–	38.200	23.500	–	5.9	8	–
Kaviris et al. (2022a)	1917-09-23	7-8	38.319	23.317	0	4.5	2	3
Shebalin et al. (1974)		7	38.200	23.500	33	4.5	4	1

Table 1.7:Macroseismic parameters for the 1914 and 1917 earthquakes adopted by Kaviris et al. (2022) and comparison with other studies. I_0: epicentral intensity, U_{epi}: epicentral uncertainty, D: focal depth and IDPs: number of intensity data points.

1.3.2.2 The 1981 sequence

On 24/02/1981 a strong offshore Mw = 6.7 earthquake (Jackson et al., 1982; Papazachos et al., 1984; Papazachos and Papazachou, 2003) occurred in the eastern Gulf of Corinth at 20:53 UTC. No foreshocks preceded the 24/02/1981 mainshock (Jackson et al., 1982; Papazachos et al., 1984). After ~5.5 hours, on 25/02/1981 at 02:35 a strong aftershock was located offshore at the eastern Gulf of Corinth (Jackson et al., 1982; Papazachos et al., 1984; Papazachos and Papazachou, 2003). The second aftershock (or the mainshock of a newer sequence according to Papazachos et al., 1984) took place on 04/03/1981 with a magnitude of Mw = 6.4 (Jackson et al., 1982) or Mw = 6.3 (Papazachos et al., 1984; Vita-Finzi et al., 1985; Hubert et al., 1996; Papazachos and Papazachou,

2003). These three events caused 20 fatalities, 500 injuries and severe damage. The total economic damage was estimated at 65 million dollars (Papazachos et al., 1984; Papazachos and Papazachou, 2003). Perachora, Pisia and Skinos were damaged by the ground motions produced by the 24/02 and 25/02 events (Jackson et al., 1982). In addition, residents of Skinos reported the occurrence of a tsunami after the 24/02 event, strengthening the consideration of an offshore causative fault. It is also reported that the last sequence before the occurrence of the 24/02 event was the one of February–April 1980. It was a minor sequence, with the largest event having M = 4.7. However, it caused damage to Kaparelli town (Papazachos et al., 1984).

Jackson et al. (1982) first studied the properties of the sequence. They mapped the ground ruptures and determined the epicenters using the joint epicenter location method, proposed by Jackson and Fitch (1979), in order to generate epicentral pattern for the estimation of the three aforementioned earthquakes. An earthquake that occurred on 07/03/1981 with $m_b = 5.5$ was set as a reference event by Jackson et al. (1982). That event was accurately located by temporary seismological stations that were installed in the epicentral area after the 04/03/1981 event, therefore the results of Jackson et al. (1982) were accurate. They also exploited teleseismic records to obtain the focal mechanism of the three major events.

However, Papazachos et al. (1984) managed to locate the three events through the "absolute" method. They utilized recorded waveforms from Greek and neighboring countries stations. Papazachos et al. (1984) also located aftershocks of the two sequences (1st: 24/02/1981–04/03/1981, 2nd: 04/03/1981–12/06/1981) and estimated the a and b values of the Gutenberg–Richter Frequency–Magnitude Distribution (FMD) (Gutenberg and Richter, 1944). The FMD diagrams are depicted in Figure 1.21. The a and b values for the first sequence are 6.24 and 1.09, respectively, whereas for the second sequence is 6.64 and 1.19, respectively. The seismicity map is illustrated in Figure 1.22.

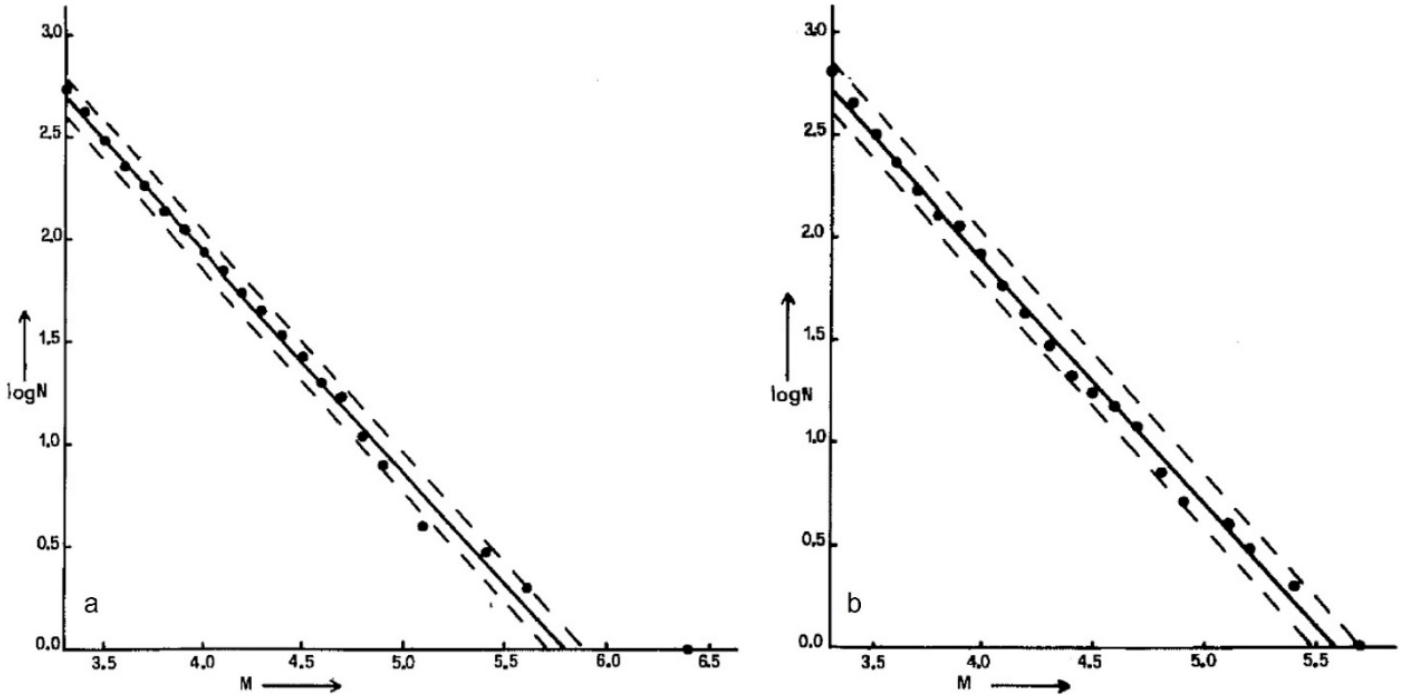

Figure 1.21: The FMD of the two sequences (Papazachos et al., 1984).

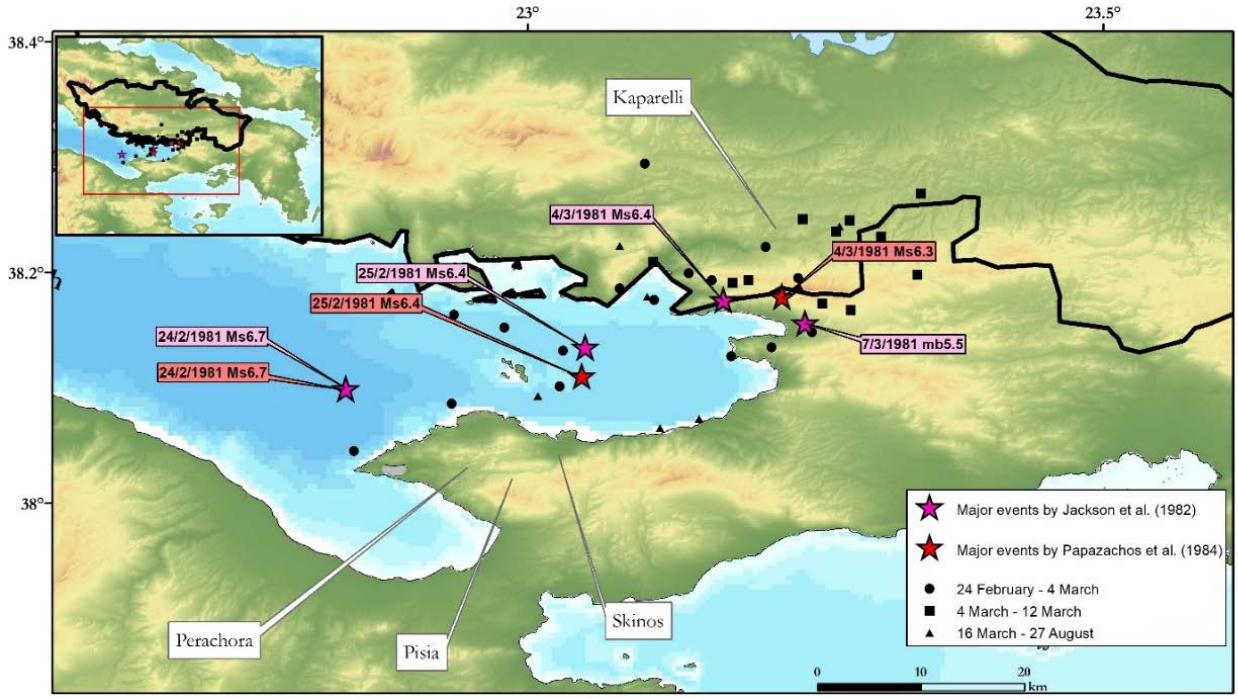

Figure 1.22:The three major 1981 earthquakes and the aftershocks with 4.6 ≤ Ms ≤ 5.7. The map was created by gathering data and georeferencing maps form both Jackson et al. (1982) and Papazachos et al. (1984).

1.3.2.3 The 2020-2021 Thiva earthquake sequence

Thiva is an area that is characterized by moderate seismicity. However, on 02/12/2020 an Mw = 4.6 mainshock occurred ~10 km east of Thiva at 10:54:56 UTC (Elias et al., 2021; Kaviris et al., 2022a). The aftershocks lasted until 03/01/2021 and the strongest aftershock had a magnitude of M_L = 3.3 and took place 2 hours after the mainshock. This sequence was initially investigated by Elias et al. (2021) in terms of seismology and geodesy. Concerning the first aspect, a routine catalogue analysis was conducted to produce a detailed earthquake catalogue by picking phase arrivals de novo. To achieve this, Elias et al. (2021) derived waveforms from the European Integrated Data Archive (EIDA) node at GI–NOA (Evangelidis et al., 2021). The selection of the stations from which data were derived was based on the visibility of the arrival of P/S phases (Elias et al., 2021). The Hypoinverse location code (Klein, 2002) was applied, and the velocity model proposed by Kaviris et al. (2007) was adopted. However, there were restrictions regarding the reliable computation of the focal depth due to the lack of seismological stations close to the epicentral area (<15 km). Moreover, the stations were not distributed in a homogeneous manner as they were concentrated in the SE part of the epicentral area (Elias et al., 2021). Regardless of the focal depth uncertainties, both the seismological and geodetic methods proposed a shallow seismic sequence, with the mainshock being located at ~2 km depth (Elias et al., 2021; Kaviris et al., 2022a).

An earthquake sequence was initiated seven months after the occurrence of the 02/12/2020 mainshock west of the epicentral area, closer to Thiva. Three events with Mw > 4.0 were recorded during the second sequence, between July–October 2021. Specifically, the first was the 01/07/2021 Mw = 4.2 earthquake, the second the 20/07/2021 Mw = 4.2 and the last one the 02/09/2021 Mw = 4.1 event. The epicenters of the events belonging to the sequence are located closer to Thiva,

compared to the ones of the December–January sequence. This caused concern among the residents of Thiva and the seismological community. The objective of Kaviris et al. (2022a) was to study this sequence and to understand its triggering mechanisms. A double–difference relocation procedure was applied to constrain a catalogue with high accuracy regarding the spatiotemporal parameters of the events from late November 2020 to October 2021. Before conducting the relocation procedure, location of the earthquakes of the sequence was performed using the Hypoinverse code in order to identify subsets that would be input separately in the procedure. Kaviris et al. (2022a) identified 12 spatiotemporal clusters. The seismicity of the second sequence started at the western part and migrated to the east. The relocated events of both sequences are plotted in Figure 1.23. The focal depths of the events belonging to the second sequence were significantly deeper than those of the first. Moreover, the second sequence was not triggered by the occurrence of the 02/12/2021 mainshock, because the combination of the event's small magnitude and focal depth was not sufficient to cause a stress transfer value capable of activating the Yliki fault. (Kaviris et al., 2022a). The possible triggering mechanism is fluid pore pressure (Kaviris et al., 2022a).

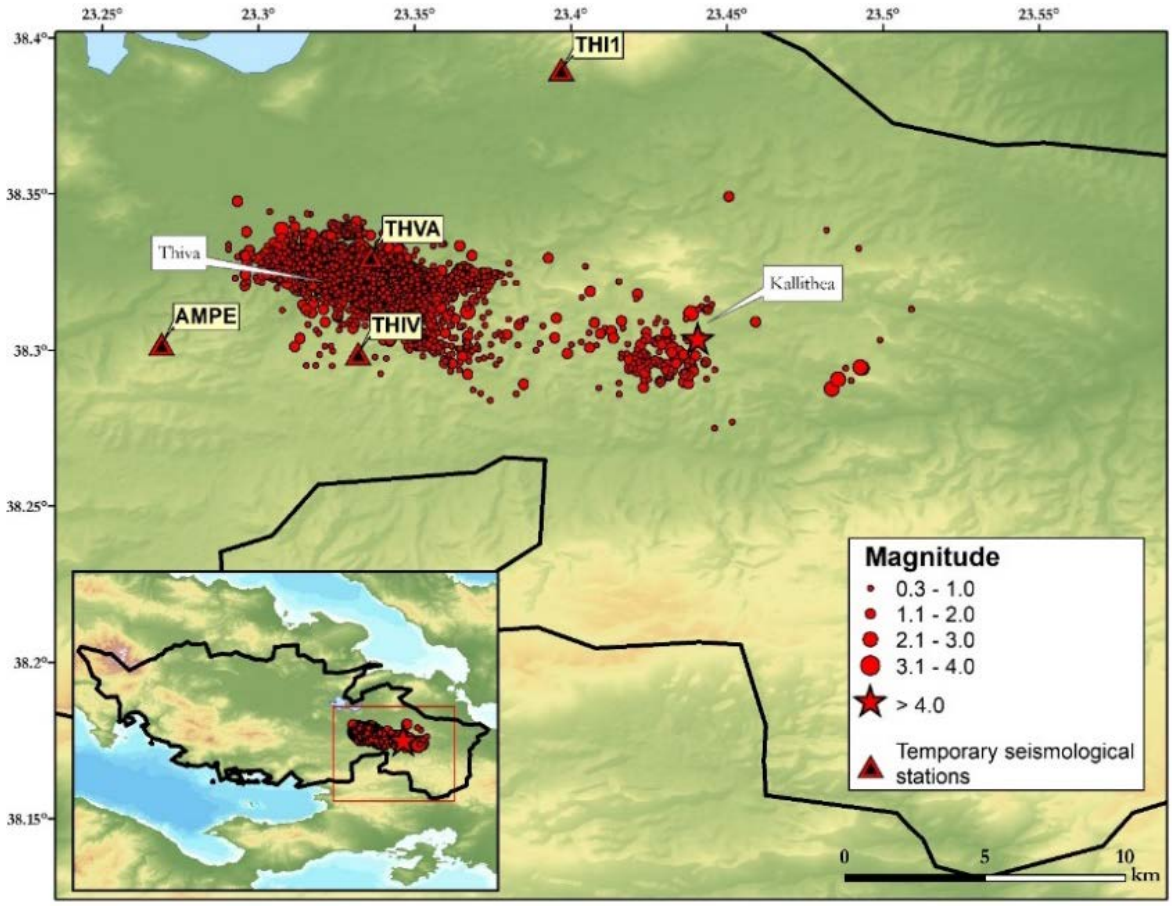

Figure 1.23: Relocated events of the 2020–2022 Thiva earthquake sequence and local stations that were installed. Information is gathered from the supplementary material of Kaviris et al. (2022a).

2 Fundamental concepts of Seismic Hazard Assessment

Seismic hazard describes the natural phenomena generated by an earthquake, such as ground movement and fault rupture. The catalyst of possible secondary phenomena (e.g., rockfalls, liquefaction, tsunamis, fires) is ground motion (Baker, 2015). Seismic Hazard Assessment (SHA) is an effort to quantify seismic hazard and its associated epistemic uncertainties (Wang, 2011). This quantification process is executed by the computation of the maximum expected Intensity Measure Level (IML) on a specific Intensity Measure Type (IMT) on a site (or sites) due to one or all possible earthquake occurrences (Tselentis and Danciu, 2010; Pavlou et al., 2021; Kaviris et al., 2022b, 2022c). An IMT could be Peak Ground Acceleration, Velocity (PGA, PGV) or Spectral acceleration (Sa). If the IMT is defined as a ground motion parameter (PGA, PGV, Sa etc.), then the IML will be computed by implementing in the calculation process one or more Ground Motion Prediction Equations–GMPEs. These equations, also known as Ground Motion Models (GMMs), are empirical relations that estimate the ground motion that will occur on a site due to an earthquake occurrence. GMPEs are created by statistical regression of multiple strong motion data for a plethora of earthquakes (Danciu and Tselentis, 2007; Graizer and Kalkan, 2016; Mori et al., 2020).

Seismic Hazard Assessment is often misleadingly associated with Seismic Risk Assessment (SRA). Seismic risk was initially defined as the probability of damage on the built environment given its exposure to a specific seismic hazard level (Cornell, 1968, 1988; Wang, 2005, 2006, 2011). The definition of seismic risk has been altered during the last years by also incorporating economic losses and potential human casualties. In order to evaluate seismic risk in a specific region, seismic hazard must be initially assessed, meaning that SHA is an input to SRA. Moreover, seismic hazard cannot be altered as it depends only on the seismotectonics of each case study, contradicted to seismic risk, which can be mitigated by reducing structural vulnerability (Tolis, 2014).

There are two general methodologies to perform SHA, i.e., the first is Probabilistic Seismic Hazard Assessment (PSHA) and the second is Scenario–Based Seismic Hazard Assessment (Kameda, 1994; Abd el-aal et al., 2015; Kaviris et al., 2022b). PSHA was introduced by Cornell (1968) and modified by McGuire (1976). In this technique, a seismotectonic model is applied to describe all possible seismic sources. Such models are available in many types depending on the knowledge of the active faults in an area. If the characteristics of all active faults are well known, then the seismotectonic model is represented by the active faults themselves. However, this is a rare case and most often the area sources are utilized. Area sources are polygons that define areas with similar seismotectonic characteristics. IML is computed by considering all possible earthquake scenarios (all possible combinations of magnitudes and distances) for a specific Return Period (RP), i.e., Probability of Exceedance (PoE)–P for T years. RP is computed via the equation (2.1):

$$\mathrm{RP} = -\frac{\mathrm{T}}{\ln\left(1-\mathrm{PoE}\right)} \tag{2.1}$$

If PoE is 10% and T is 50 yr then the equation (2.1) is rewritten as:

$$\mathrm{RP} = -\frac{50}{\ln(1-0.1)} = -\frac{50}{\ln(0.9)} \sim 475 \text{ yr} \tag{2.2}$$

A return period of 475 yr is utilized in the vast majority of National Building Codes in Europe (Kaviris et al., 2022b). If PoE is 10% and T is 100 yr then the RP is approximately 950 yr, doubling the previous RP. The latter is applicable for the construction of buildings of high importance, such as medical centers, because the IML is significantly increased.

In the second methodology, individual earthquake scenarios are created, and synthetic waveforms are simulated for one or many sites. The selection of the candidate earthquake scenario is a sophisticated task. The candidate earthquake can be referred to as the "maximum credible" earthquake scenario, which is not the worst–case but the worst realistic earthquake scenario. The maximum credible earthquake is considered as the most severe earthquake at a point of interest, taking into account both tectonic and seismological evidence. This methodology computes IML for a given site without the time framework that PSHA has.

2.1 Probabilistic Seismic Hazard Assessment

This technique allows the computation of ground motions for all possible earthquake occurrences. Therefore, the uncertainty behind the selection of the "maximum credible" earthquake scenario is diminished. All possible ground motions are computed alongside their probability of occurrence. The final IML is the one that corresponds to the desired annual exceedance rate (Baker, 2015; Baker et al., 2021). PSHA is composed of five steps (McGuire, 1976; Tselentis and Danciu, 2010; Baker, 2015; Baker et al., 2021):

1. the creation or input of a seismotectonic model to identify all seismic sources that produce ground motions,
2. the characterization of the earthquake magnitude distribution for all sources,
3. the characterization of the source–to site distance distribution for all sources,
4. the characterization of the resulting ground motion distribution for all sources and for all possible combinations of magnitudes and distances and
5. addressing epistemic uncertainties for a more realistic IML distribution with their associated exceedance rates.

Following the completion of these steps, the desired IML will be the one that matches the desired annual exceedance rate. Concerning the first step, the type of the seismotectonic model varies depending on the knowledge of the characteristics of the active faults. In most cases, area sources are adopted (or created) to characterize the seismotectonics of the study area by defining regions of similar seismotectonic characteristics (Figure 2.1).

Following the selection of the seismotectonic model, the distribution of the earthquake magnitude needs to be assessed. Gutenberg and Richter (1944) proposed the following equation to describe this distribution:

$$\log N(M) = a_t - bM \quad (2.3)$$

where N(M) is the number of earthquakes that have a magnitude larger than or equal to M, while a_t and b are constants that are typically computed through statistical analysis. The first constant (a_t) describes the overall rate of earthquakes in a region, subsequently its seismicity, whereas the second constant (b) indicates the relative ratio between small and high magnitudes, which is approximately 1 for most cases of background seismicity. Equation (2.3) depends on the time span of the earthquake catalogue, meaning that the equation can be converted to be temporally independent, referring to one year (equation, 2.4):

$$\log \lambda_M = a - bM \quad (2.4)$$

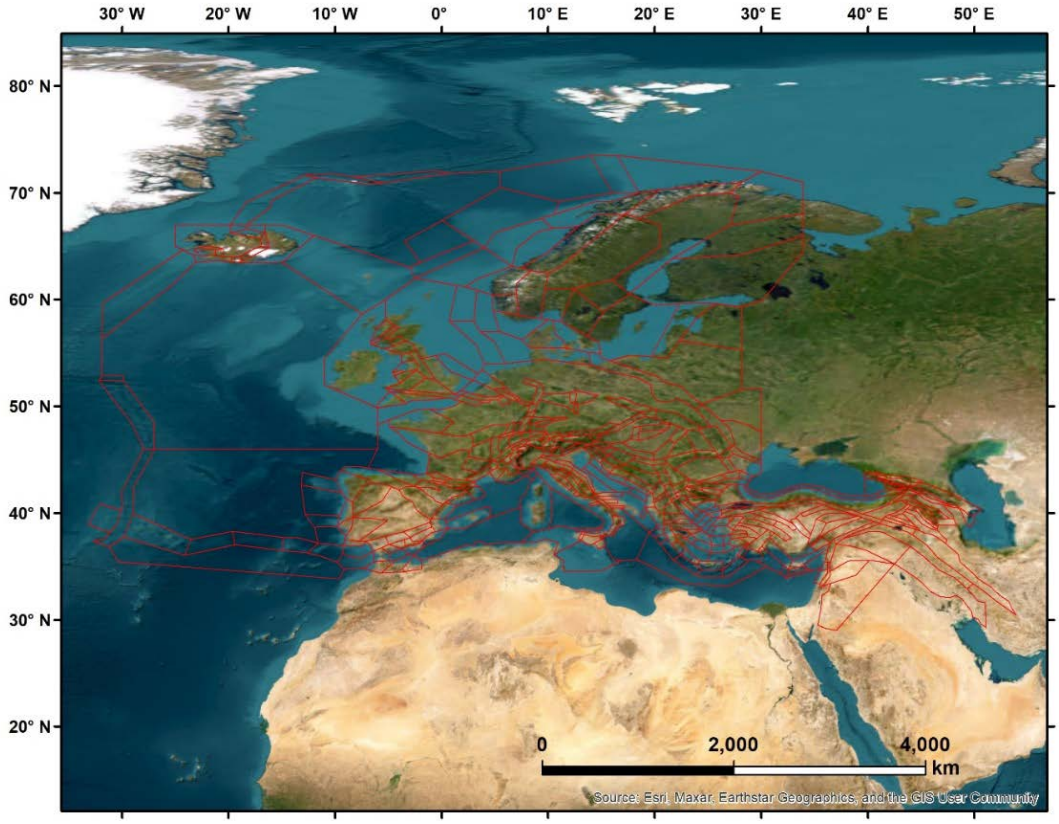

Figure 2.1: The Euro–Mediterranean Seismic Hazard Model 2013 (ESHM13) proposed by Woessner et al. (2015).

where λ_m is the annual rate of magnitudes greater than or equal to magnitude M and $a = a_t - \log t$, where t is the catalogue's duration (in years). Equation (2.4) is exploited to compute the Cumulative Distribution Function (CDF), as described in equation (2.5), of magnitudes higher than a threshold value–m_{min} which is commonly associated with the magnitude of completeness, Mc.

$$F_M(m) = P(M \le m | M > m_{min}) = \frac{\lambda_{m_{min}} - \lambda_m}{\lambda_{m_{min}}} = \frac{10^{a-bm_{min}} - 10^{a-bm}}{10^{a-bm_{min}}} \\ = 1 - 10^{-b(m-m_{min})}, \quad m > m_{min} \tag{2.5}$$

where $F_M(m)$ is the CDF of a random magnitude M and $P(M \le m | M > m_{min})$ is the probability that this random magnitude has a value lower than m and higher than the threshold–m_{min}. The Probability Density Function (PDF) is computed by the first–order derivative function of the CDF:

$$f_M(m) = \frac{d}{dm} F_M(m) = \frac{d}{dm}\left[1 - 10^{-b(m-m_{min})}\right] = b\ln(10)10^{-b(m-m_{min})} \\ = \beta 10^{-b(m-m_{min})}, m > m_{min} \tag{2.6}$$

where $\beta = b\ln(10)$. The distribution of the distances is also characterized by the CDF of a random distance R via equation (2.7) by considering the following circular area source model (Figure 2.2):

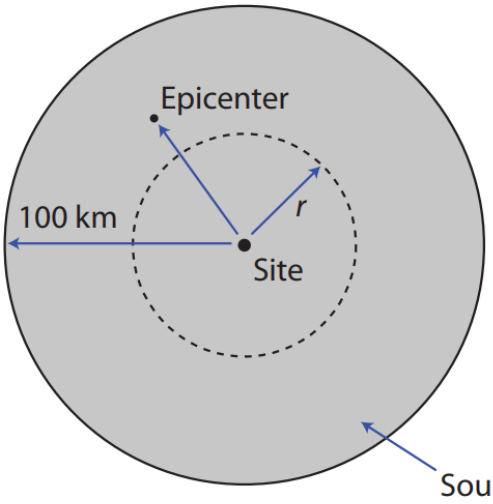

Figure 2.2: A single circular area source model that is utilized to address the CDF of a random distance R. The maximum radius of the area source is R_{max} = 100 km. Figure is obtained by Baker (2015).

$$F_R(r) = P(R \leq r) = \frac{\pi r^2}{\pi(100)^2} = \frac{r^2}{10000} \tag{2.7}$$

where $P(R \leq r)$ is the probability that this random distance has a value lower than or equal to r and π is the mathematical constant. Similar to the preceding test, the PDF is computed by the first–order derivative of the CDF, which is:

$$f_R(r) = \frac{d}{dr} F_R(r) = \begin{cases} \frac{r}{5000} & 0 \leq r < 100 \\ 0 \text{ otherwise} & \end{cases} \tag{2.8}$$

For the fourth step, it is essential to be provided with information regarding the selected GMPE, which is the standard deviation (σ) of the GMPE and its mean value (μ). The probability that an IML of the IMT, that is caused by an earthquake of magnitude m in distance r, is higher than a specific value x is computed via the equation (2.9):

$$P(IML > x|m, r) = 1 - \Phi\left(\frac{x - \overline{IML}}{\sigma}\right) \tag{2.9}$$

where $\overline{IML}$ is the mean IML computed by a selected GMPE and $\Phi(u)$, where $u = \frac{x-\overline{IML}}{\sigma}$, is the typical normal distribution. The CDF of the latter distribution is obtained by:

$$P(IML > x|m, r) = \int_x^{\infty} \frac{1}{\sigma\sqrt{2\pi}} e^{-\left(\frac{x-\overline{IML}}{\sigma}\right)^2} du \tag{2.10}$$

In the final step, the probability that an IML of the IMT is higher than a specific value of x, when taking into consideration all the possible combinations of m and r and for more than one area source, is computed via equation (2.10):

$$P(IML > x) = \sum_{i=1}^{n_{sources}} \int_{m_{min}}^{m_{max}} \int_0^{R_{max}} P(IML > x|m, r) f_M(m) f_R(r)\, dr dm \tag{2.11}$$

However, in the above equation there is no information regarding the earthquake occurrence rates. To incorporate this, the annual rate of exceeding the threshold magnitude for a specific area source (λm_{min}) is added in the following equation:

$$\lambda(IML > x) = \sum_{i=1}^{n_{sources}} \lambda(m_{min}) \int_{m_{min}}^{m_{max}} \int_{0}^{R_{max}} P(IML > x|m, r) f_M(m) f_R(r)\, drdm \qquad (2.12)$$

where $\lambda(IML > x)$ is the annual rate of IM > x (the annual rate of exceedance). Equation (2.11) is not in a form to be inserted in a software environment because of the two integrals. To overcome this obstacle, the discretization of the integrals is overtaken in equation (2.13):

$$\lambda(IML > x) = \sum_{i=1}^{n_{sources}} \lambda(m_{min}) \sum_{j=1}^{n_M} \sum_{k=1}^{n_R} P\left(IML > x \middle| m_j, r_k\right) P\left(M_i = m_j\right) P(R_i = r_k) \qquad (2.13)$$

It must be noted that there is no information regarding the return period in equation (2.13), which is thought–provoking, given that most of the studies provide PGA maps for a return period of 475 yr. The question that arises is how the IML is computed for a given return period. In the above equation, the specific values of x could be infinite, meaning that the annual exceedance rates are also infinite. Let us consider that the IMT is PGA and that the values are in cm/s^2. If one plotted all possible pairs of $\lambda(PGA > x)$ and x, then the PGA seismic hazard curve would be constructed (Figure 2.3). In order to estimate the PGA value that corresponds to a desired return period (for example 475 or 950 yr), the annual exceedance rate that matches that return period must be identified. After that, the final PGA value would be the x-axis value that corresponds to that annual exceedance rate (Figure 2.3).

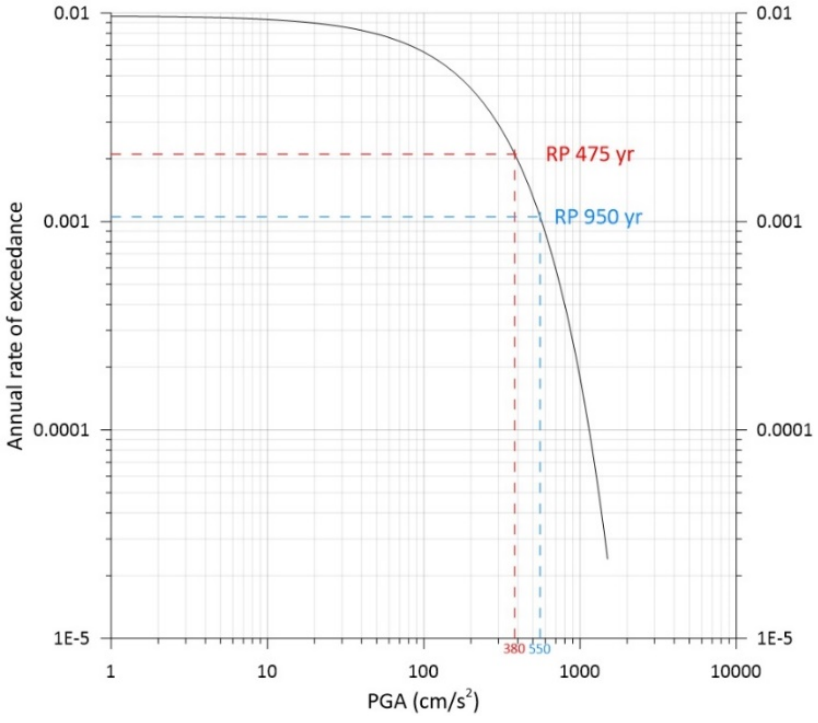

Figure 2.3: A seismic hazard curve for a random site. The refence axes correspond to return periods of 475 and 950 yr (red and blue axis, respectively).

2.2 Scenario–Based Seismic Hazard Assessment

A Scenario–Based Seismic Hazard Assessment is usually performed either by deterministic or stochastic modelling (or both). The output of a deterministic model is fully determined by the parameters and the initial conditions that are defined by the user. Stochastic models possess some inherent randomness, and the initial conditions will lead to an ensemble of different outputs (Byrne, 2013). In terms of SHA, the results of the IML will never be identical per run in stochastic modeling contradicted to deterministic modeling (Byrne, 2013). In the context of Scenario–Based Seismic Hazard Assessment, stochastic modeling is critical in the computation of the IML. To justify the preceding, the description of an earthquake rupture is essential. When the slip on a fault plane accelerates on a specific patch, then an earthquake is nucleated, and seismic waves of a wide frequency band are generated as the rupture propagates. There is a likelihood that these waves are refracted or reflected (or both) when travelling towards the surface, resulting in the scattering of seismic waves (Gibowicz and Kijko, 1994). Stress variations, seismic wave geometrical spreading and the heterogeneity of the upper crust are strengthening the selection of the stochastic modelling to import the uncertainty and randomness, especially when dealing with high frequency ground motions (Boore, 2003; Bonatis, 2020; Sabetta et al., 2021).

2.2.1 Finite fault stochastic ground motion modeling

Strong ground motions are initiated when seismic waves reach the surface. These ground motions–u(t)–are recorded by a sensor (seismometer or accelerometer) and can be expressed as the convolution of the seismic source–s(t)–, the wave propagation path–p(t)–, the local site effect–g(t)–and the instrument response–i(t)– (equation 2.14). However, multiplication is the equivalent of convolution when transforming the time domain to the frequency one, using the Fourier transform function. Therefore, the equation (2.14) can be rewritten as equation (2.15).

$$u(t) = s(t) * p(t) * g(t) * i(t) \tag{2.14}$$

$$u(f) = s(f) \times p(f) \times i(f) \tag{2.15}$$

All parameters, except for the instrument response, need to be addressed. Briefly, seismic source is parametrized by providing the fault dimensions, the seismic moment, the nucleation point and the slip distribution. Concerning the propagation path characteristics, the geometrical spreading needs to be addressed. Last, the local site effects are parametrized by providing parameters regarding the shallow sedimentary layers that affect the amplitude of the seismic wave.

Stochastic simulations of ground motions emerge from the idea that ground movement, especially during the arrival of S–waves and in proximity to the ruptured plane, is random in nature (Hanks, 1979; Hanks and McGuire, 1981). Since this randomness exist, then strong ground motions can be simulated by Gaussian white noise signal, in a band between the corner frequency and the frequency at which the logarithm of the Fourier amplitude spectra starts to decay for increasing frequencies (f_c–f_{max}). In this way, the acceleration transient time series can be obtained by fixing the spectral amplitude and then generating an array of phases, which are random numbers that are uniformly distributed between 0 and 2π. This was initially modelled by Boore (1983), who later introduced the Stochastic–Method SIMulation (SMSIM) computer code (Boore, 2003). According to Boore (2003), the aforementioned procedure could be described in 6 steps (Figure 2.4). In the first step, the Gaussian white noise signal is generated, whose mean value is equal to zero. Before explaining the second step, the window function must be defined. A window function in signal

processing is a mathematical function that is used to analyze or process a finite length section of a signal by modifying its shape in the time domain (Prabhu, 2014). The second step is to multiply the noise signal by a window function of specified duration, such as the Saragoni–Hart window (Saragoni and Hart, 1973) to obtain a shape that is representative of a damped oscillation. Regarding the third step, this signal is transformed to the frequency domain and is normalized for the Root Mean Square (RMS) spectrum to be equivalent to unity (fourth step). In the fifth step a theoretical point–source deterministic ground motion signal is multiplied by the RMS spectrum to obtain a ground motion that has the randomness of the white noise signal. In the final step the signal is transformed to the time domain to obtain the stochastic acceleration time series (Boore, 2003). The theoretical point–source deterministic acceleration spectrum, A(f), is computed by:

$$A(f) = \frac{CM_0(2\pi f)^2}{1 + (f_c)^2}\, e^{-\pi f k} \frac{e^{\frac{\pi f R}{Q\beta}}}{R} \tag{2.16}$$

where $C = K^{\theta\varphi} \frac{FV}{4\pi\rho\beta^3 R_0}$ in which $K^{\theta\varphi}$ is the radiation pattern, F is the free surface amplification (usually is equal to 2 if the site is not within a borehole), V is the partition of total S–wave energy into the two horizontal components (which is equal to 0.71 for small site–source distances), R is the hypocentral distance, k describes the local site characteristics, Q is connected to the anelastic attenuation, M_0 is the moment magnitude in dyn cm and β is the S–wave propagation velocity. The corner frequency is computed by:

$$f_c = 4.9 \times 10^6 \times \beta \left(\frac{\Delta\sigma}{M_0}\right)^{\frac{1}{3}} \tag{2.17}$$

where Δσ is the stress drop (in bars). Boore (2009) upgraded the algorithm to take into consideration fault ruptures. He developed the EXSIM code, which was successfully validated by Atkinson and Assatourians (2014). It is often mentioned as the Finite–Fault Modelling algorithm. Boore (2009) considered the dynamic corner frequency approach, proposed by Motazedian and Atkinson (2005). Let us consider a ruptured fault segment which is gridded in such way that each node represents a point source. The ground motion from the entire segment is obtained by the sum of all ground motions due to each subsource with an assigned time delay (Δt_{ij}). Each subsource is treated as a point source and, therefore, the acceleration spectrum, $A_{ij}(f)$, is computed by the equation (2.16). The corner frequency (f_c) of the first subfault, which is the nearest to the initiation of the rupture, is the same as in equation (2.17). The corner frequency of the ij^{th} patch (where i and j is the position of the subfault along the fault's length and width, respectively) is computed by equation (2.18):

$$f_{cij}(t) = 4.9 \times 10^6 \times \beta \left(\frac{N \times \Delta\sigma}{N_R \times M_0}\right)^{\frac{1}{3}} \tag{2.18}$$

where N represents the total number of subsources, while N_R is the quantity of subsources that have fractured when the rupture front reaches the ij^{th} subsource. In this way, the corner frequency is reduced as the rupture propagates. The algorithm inserts a scaling factor (H_{ij}) in the computations to overcome this obstacle and preserve the high frequency spectral content of the nodes (equation 2.19):

$$\mathrm{A(t)} = \sum_{i,j=1}^{N_i N_j} H_{ij} \times A_{ij}(t - \Delta t_{ij} - T_i) \qquad (2.19)$$

where A(t) is the acceleration time series on the site due to the whole ruptured area, $A_{ij}(t - \Delta t_{ij} - T_i)$ is the acceleration time series for ij[th] subfault, where Δt_{ij} is the corresponding time–delay and T_i is the rise time expressed as a fraction of the total duration of the signal. The scale factor in the distributed version of the program is determined by comparing the integral of the squared subfault velocity spectrum to the integral of the squared target (simulated event) spectrum, aiming to equate the former with the 1/N of the latter (Boore, 2009).

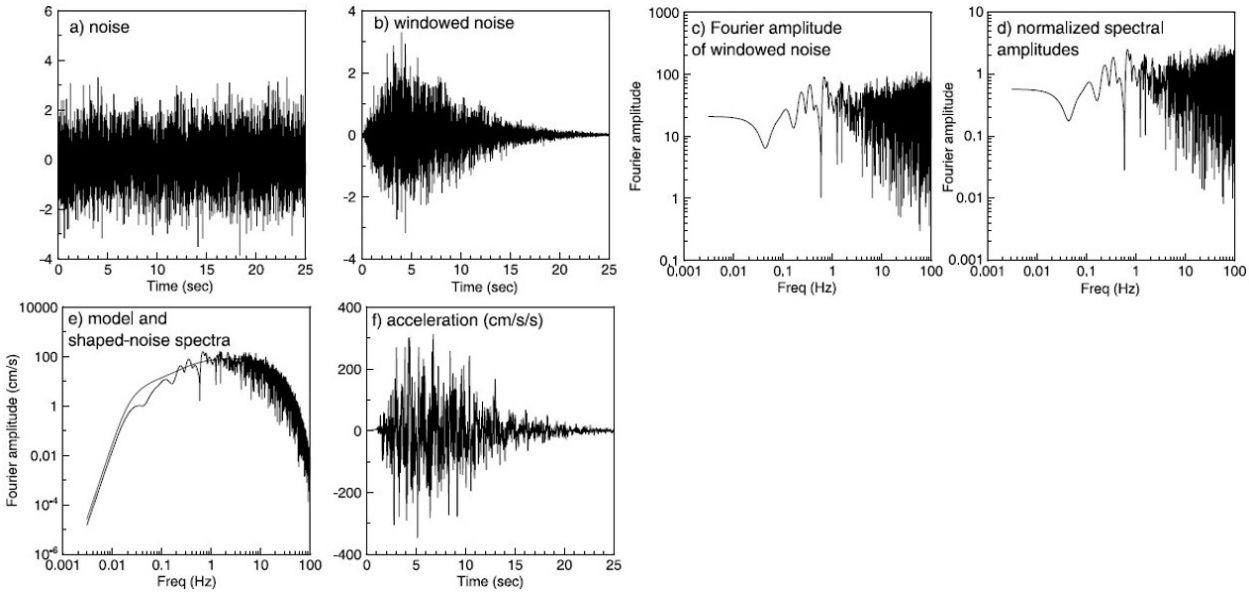

Figure 2.4: The six steps of the stochastic ground motion simulation. Figure 2.4 a represents the first step and 2.4 f the sixth step (Boore, 2003).

3 Probabilistic Seismic Hazard Assessment for Boeotia

To conduct a Probabilistic Seismic Hazard Assessment (or Analysis) utilizing the approach proposed by Cornell (1968) and McGuire (1976), a plethora of data is required. First and foremost, the implementation of an earthquake catalogue is essential for the analysis. The remaining data can be categorized as geometrical, seismicity and attenuation data. Following that, a software must be chosen to compute the desired results, by applying equation (2.13).

Regarding the geometrical data, seismotectonic models must be implemented, which will be used for the computation of the seismicity data. These data are a) the magnitude of completeness (Mc), the annual rate of Mc exceedance [λ(Mc)], the a and b constants of the Gutenberg–Richter Frequency Magnitude Distribution (FMD) and the maximum expected magnitude (Mu). The epicenters of each area source of each seismotectonic model are extracted and treated as separate earthquake catalogues. Therefore, the seismicity data have to be computed $n_{sources}$ times. Attenuation data are addressed by implementing one or more GMPEs.

Seismic hazard is assessed by computing several IMT utilizing mostly empirical relations, leading to non negligeable epistemic uncertainties (McGuire and Shedlock, 1981; Abrahamson and Bommer, 2005; Musson, 2012). In addition, the lack of knowledge regarding all active faults within the study area is a factor that leads to dissimilar versions of seismotectonic models that have different seismotectonic interpretations. A powerful tool to address epistemic uncertainties is through the logic tree approach (Bommer and Scherbaum, 2008; Atkinson et al., 2014; Marzocchi et al., 2015; Kaviris et al., 2022b, 2022c). A logic tree is used to represent the various choices and uncertainties involved in the assessment of seismic hazard. Each branch of the tree corresponds to a model selected by the analyst and a normalized weight is assigned to reflect the confidence of the chosen model. The hazard calculation is then performed by executing all possible branches of the tree. Major branches typically represent different seismotectonic models. The minor branches represent the various choices that are made within each major branch, such as different GMPEs (Figure 3.1).

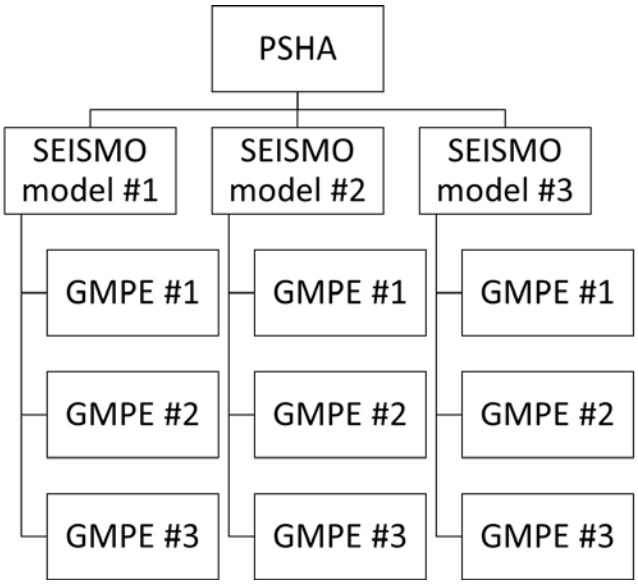

Figure 3.1: A template of the logic tree approach.

3.1 Geometrical data and earthquake catalogue

Three seismotectonic models in the form of area sources are implemented in the PSHA computational scheme in this thesis. The first model is the Euro–Mediterrenean Seismic Hazard Model 2013 (ESHM13) that was proposed by Woessner et al. (2015) under the Seismic Hazard Harmonization in Europe (SHARE) project. The second model is the ESHM20, which is the updated version of the latter (Danciu et al., 2021). Finally, the third one is the Greek Zonation model suggested by Vamvakaris et al. (2016), VAM16 hereafter.

The area sources of the first two models cover the whole European continent, whereas VAM16 covers all the Greek region. In order to take into account only earthquakes that may have an impact to the ground motions in Boeotia, a 100 km distance criterion was applied in the area sources (Kaviris et al., 2022b, 2022c). Specifically, all the adopted zones are entirely or partially within a 100 km distance from the northernmost, southernmost easternmost, and westernmost point of the Boeotia borderline (Figure 3.2). This criterion left ESHM13 with 14 zones, ESHM20 with 13 and VAM16 with 22.

In terms of seismotectonics, VAM16 describes area sources with greater detail than ESHM13 and ESHM20, as it can be clearly seen for the case of the Gulf of Corinth (Figure 3.2). VAM16 divides the western, central, and eastern GoC (zones 7, 8 and 9, Figure 3.2 c), whereas ESHM13 merges the whole gulf (zone 11, Figure 3.2 a) and ESHM20 merges the Gulf of Corinth with the Saronic Gulf (zone 11, ESHM20 in Figure 3.2 b). The level of detail in area sources has both advantages and disadvantages. The obvious advantage is that seismicity will be described with higher accuracy as this level increases, meaning that area sources of high, intermediate and low seismicity will be easily detected, as seismotectonic criteria are more accurate. However, the major disadvantage is that as the $n_{sources}$ variable increases, less earthquakes will be located in each area source, because obviously the initial catalogue contains a stable number of earthquakes in total. The smaller number of hypocenters per zone will affect the uncertainty of the seismicity data computation, e.g., of the b-value. On the contrary, having large area sources will bring more events per zone but seismicity data will be less related to the seismotectonics, given that area sources of high seismicity will be merged with zones of intermediate and perhaps even low seismicity. These issues are favoring the option to select more than one seismotectonic model, adding more major branches to the logic tree.

The selection of the earthquake catalogue is essential for the conduction of PSHA, as seismicity data will be computed by performing statistical analysis of each area source's catalogue. The computational scheme incorporates the instrumental earthquake database for Greece and the surrounding area for the years 1900–2009, which was compiled by Makropoulos et al. (2012). This decision was made given that this earthquake catalogue is homogeneous and that all magnitudes have been consistently calibrated to Mw. Historical data (pre–1900 events) were not used due to the greater uncertainty, regarding both the inferred locations and the magnitudes. The catalogue ends in 2009, meaning that earthquakes recorded after that year are not incorporated into, providing less data for the computation of the seismicity data. To solve this problem, the catalogue was temporarily updated to also include events after 2009 following the exact procedure described by Makropoulos et al. (2012). Specifically, reviewed events were adopted from the International Seismological Centre (ISC) hosted at (http://www.isc.ac.uk/iscbulletin/search/). These earthquakes are in the body-wave magnitude (m_b) scale, allowing the conversion from m_b to Ms and from Ms to Mw, as proposed by Makropoulos et al. (2012) following the equations:

$$Ms = 1.37m_b - 1.74 \pm 0.27 \quad (3.1)$$

$$Mw = 0.8786Ms + 0.582 \pm 0.26 \quad (3.2)$$

After the update, the catalogue was enriched with the Mw > 4.0 events of the Thiva 2020-2021 earthquake sequence.

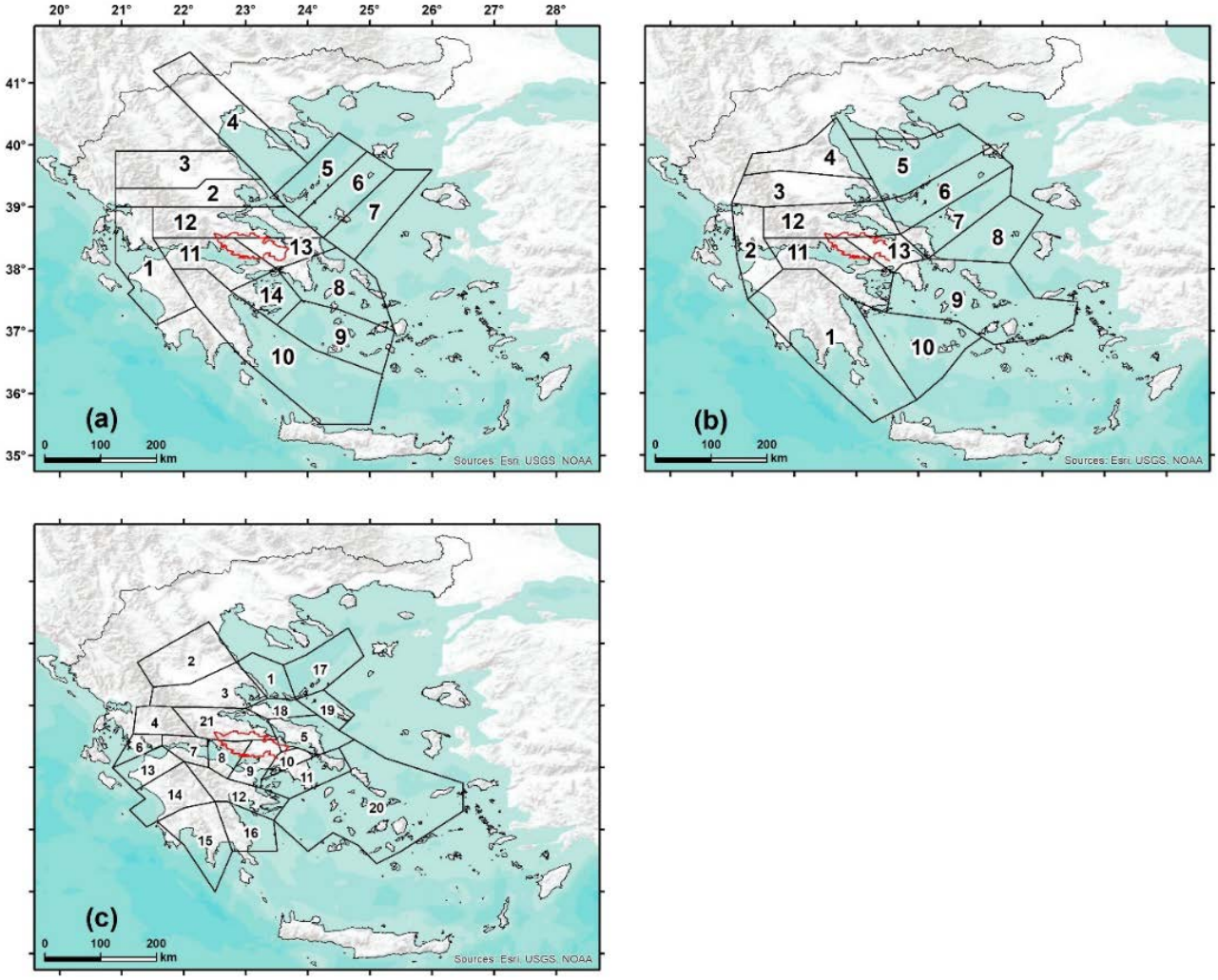

Figure 3.2: The area sources selected for Boeotia (red borderline) after applying the 100 km distance criterion. In the upper left the area sources of ESHM13 are depicted, in the upper right the sources of ESHM20 and those of VAM16 in the lower left.

3.2 Addressing the seismicity and attenuation data for Boeotia

The seismicity data are Mc, λ(Mc), the a and b constants of the Gutenberg–Richter FMD and Mu. The triplet of Mc, a and b values were computed using the **MAX**imum **C**urvature method (MAXC), proposed by Wiemer and Wyss (2000). The MAXC method is a quick and robust way to compute these parameters and has less uncertainties in zones that host a small number of earthquakes (Zhou et al., 2018). To understand the MAXC method, let us create an arbitrary magnitude histogram and plot its distribution fit as a red dashed line (Figure 3.3). In this method, Mc is defined as the point where the curvature of the non–cumulative distribution, the red dashed

line, is at its maximum (black solid line), subsequently, Mc = 4.1. Considering all data with magnitudes larger than or equal to the Mc value, the constants of the Gutenberg–Richter law are computed using the classical maximum likelihood approach proposed by Aki (1965).

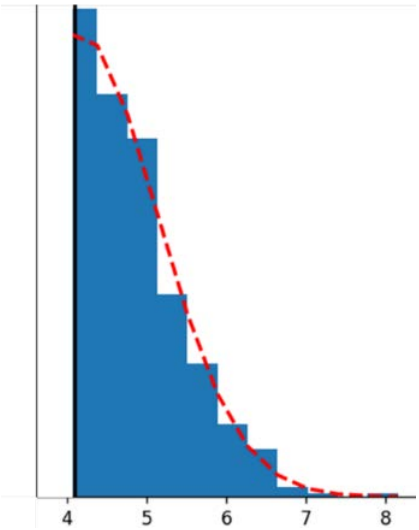

Figure 3.3: Arbitrary magnitude histogram. The black solid line denotes the value in which the curvature of the histogram (red dashed line) is at its maximum.

The annual rate of Mc exceedance, λ(Mc), was computed by dividing the total number of earthquakes that have M ≥ Mc within each zone for the whole time span of the earthquake catalogue (Kijko and Sellevoll, 1989, 1992; Kijko and Smit, 2012). The last seismicity parameter, Mu, was calculated using the Robson–Whitlock–Cooke (R–W–C) procedure proposed by Robson and Whitlock (1964) and Cooke (1979):

$$M_u = m_{maxobs} + 0.5(m_{maxobs} - m_{n-1}) \quad (3.3)$$

where m_{maxobs} is the maximum observed magnitude within the area source and m_{n-1} is the second maximum observed magnitude. If m_{n-1} is equal to m_{maxobs}, then the result in the parenthesis is zero.

In addition, the percentages of Normal Focal Mechanisms (NFM) and Non–Normal Focal Mechanisms (NNFM) were computed for each area source by considering the catalogue proposed by Kapetanidis and Kassaras (2019). To distinguish among the different types of focal mechanisms, the rake value was considered (Table 3.1). The latter provides significant aid in the logic tree approach (see section 3.5 “Creating the logic tree”). The final computed parameters are summarized for all area sources of all seismotectonic models (Table 3.2).

Focal mechanism	Rake (°)
Normal	-160 < Rake < -20
Thrust	20 < Rake < 160
Strike–slip	-20 ≤ Rake ≤ 20 or -180 ≤ Rake ≤ -160 or -160 ≤ Rake ≤ 180

Table 3.1: The main focal mechanism types depending on the rake value.

ESHM13								
ZONE	*λ(Mc)*	*β*	*Mu*	*Mc*	*b*	*NFM (%)*	*NNFM (%)*	*Events*
1	2.39	2.30	6.6	4.1	1.00	0.25	0.75	289
2	1.24	1.84	6.6	4.4	0.80	0.72	0.28	211
3	0.40	2.30	6.1	4.4	1.00	0.93	0.07	61
4	0.49	2.30	6.6	4.1	1.00	0.58	0.42	59
5	1.12	2.30	6.8	4.1	1.00	0.12	0.88	135
6	0.49	2.30	7.0	4.4	1.00	0.19	0.81	88
7	0.98	2.30	7.2	4.1	1.00	0.20	0.80	118
8	0.08	2.12	5.6	4.3	0.92	0.60	0.40	14
9	0.31	2.30	5.9	4.3	1.00	0.40	0.60	45
10	0.93	2.07	6.8	4.4	0.90	0.37	0.63	166
11	3.50	1.73	6.4	4.1	0.75	0.82	0.18	423
12	0.79	2.19	5.7	4.4	0.95	0.76	0.24	151
13	0.47	1.84	6.4	4.4	0.80	1.00	0.00	96
14	0.21	2.30	6.0	4.3	1.00	0.88	0.12	28
ESHM20								
1	1.64	1.96	8.0	4.4	0.85	0.59	0.41	303
2	0.78	2.35	6.6	4.4	1.02	0.21	0.79	152
3	1.31	2.23	6.6	4.4	0.97	0.73	0.27	219
4	0.08	2.10	6.1	5.1	0.91	0.86	0.14	26
5	1.48	2.00	6.8	4.1	0.87	0.27	0.73	179
6	0.68	2.10	7.0	4.4	0.91	0.43	0.57	113
7	1.02	2.28	7.2	4.1	0.99	0.27	0.73	124
8	0.56	2.19	5.8	4.1	0.95	0.11	0.89	68
9	0.21	1.91	5.4	4.3	0.83	0.60	0.40	31
10	0.51	2.49	5.8	4.1	1.08	0.40	0.60	62
11	3.68	2.19	6.4	4.1	0.95	0.82	0.18	445
12	0.78	2.37	5.7	4.4	1.03	0.76	0.24	147
13	0.45	1.91	6.4	4.4	0.83	1.00	0.00	93
VAM16								
1	0.33	2.21	6.1	4.4	0.96	0.50	0.50	50
2	0.20	2.35	6.5	4.4	1.02	1.00	0.00	31
3	1.16	1.98	6.6	4.4	0.86	0.78	0.22	192
4	0.46	2.88	6.0	4.3	1.25	0.64	0.36	60
5	0.35	2.62	6.0	4.1	1.14	0.93	0.07	43
6	0.09	2.53	5.5	4.6	1.10	0.67	0.33	38
7	1.76	2.10	6.5	4.1	0.91	0.83	0.16	23
8	0.42	2.10	6.3	4.4	0.91	0.89	0.12	211
9	0.76	2.10	6.5	4.4	0.91	0.85	0.15	80
10	0.13	1.87	5.9	4.4	0.81	1.00	0.00	25
11	0.05	2.46	5.4	4.6	1.07	1.00	0.00	14
12	0.39	1.82	6.3	4.1	0.79	0.31	0.69	156
13	0.76	2.37	6.6	4.4	1.03	0.17	0.83	47
14	1.23	2.14	6.0	4.1	0.93	0.48	0.52	127
15	0.50	2.33	5.8	4.4	1.01	0.84	0.17	147
16	0.25	2.28	6.9	4.4	0.99	0.67	0.33	82
17	0.85	2.67	6.8	4.1	1.16	0.11	0.89	102
18	0.14	2.60	5.5	4.4	1.13	0.56	0.44	25
19	0.30	2.86	6.4	4.3	1.24	0.14	0.86	53
20	0.33	2.86	6.0	4.3	1.24	0.40	0.60	50
21	0.24	3.52	5.6	4.3	1.53	0.84	0.16	29

Table 3.2: All seismicity data for each area source (see Figure 3.2 for ID–area source correspondence).

The data presented in the last column of Table 3.2 is an indicator of the uncertainties associated with selecting a suitable seismotectonic model. The number of earthquakes per zone varies depending on the model chosen. The area sources of Vamvakaris et al. (2016) exhibit the lowest event numbers, compared to those of ESHM13, 20. For instance, the 14th area source of the VAM16 model includes only 14 earthquakes, rendering the computation of the b–value using the maximum likelihood method impossible. Alternatively, the least–square method was considered to estimate the b–value in this area source. In contrast, ESHM20 has a higher number of earthquakes per area source, indicating that the seismicity parameters were calculated using more data. However, as the surface area of the zones increases, they may cover areas with dissimilar seismotectonic characteristics, thus affecting the seismic parameters calculated per zone.

In this thesis, seismic hazard is assessed by computing PGA and PGV for return periods of 475 and 950 years for the entire Boeotia and Sa for the first return period for the cities of Thiva and Livadia. Thus, GMPEs must be implemented in the computational process. The goal was to select GMPEs that have been proposed by considering strong motion data from the Greek territory. However, it must be highlighted that some distance types were not chosen for the PSHA of Boeotia, such as the Joyner and Boore type of distance that requires the usage of faults, as in the case of Akkar et al. (2014), Bindi et al. (2014) and Boore et al. (2020) models. For PGA the GMPEs of Margaris et al. (2002), Skarlatoudis et al. (2003), Danciu and Tselentis (2007), Sakkas (2016) and Chousianitis et al. (2018) were selected. In addition, for PGV the adopted models are the ones proposed by Margaris et al. (2002), Danciu and Tselentis (2007), Skarlatoudis et al. (2007) and Chousianitis et al. (2018). For Sa only the model proposed by Danciu and Tselentis (2007) is utilized. These models account for different focal mechanism (F) and soil types (S), apart from the model proposed by Margaris et al. (2002) that does not consider focal mechanism types. Specifically, for the beachball variable, a value of zero (0) and one (1) is assigned to a normal and non–normal fault plane solution, respectively. All aforementioned models are summarized in **Error! Reference source not found.** and are compared in Figure 3.4 for an arbitrary Mw = 6.0 event with a normal focal mechanism and for rock site conditions.

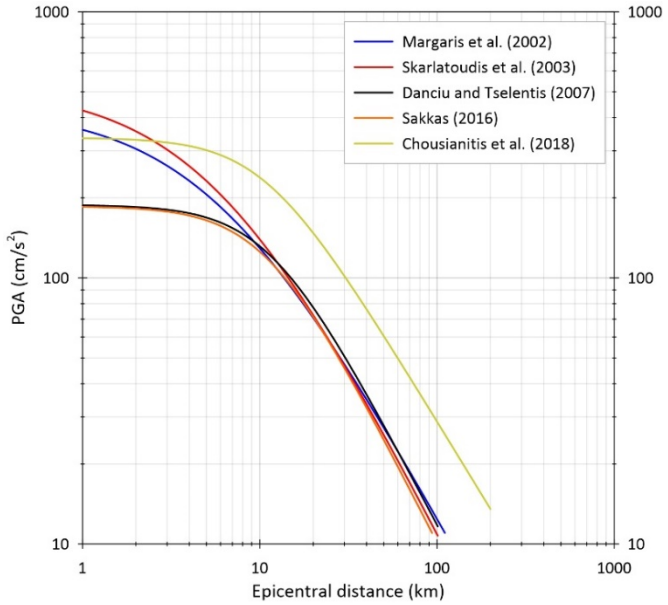

Figure 3.4: Comparison of all selected GMPEs in terms of PGA for an of magnitude Mw = 6.0 that ruptured a normal fault. All PGA values were obtained considering rock conditions.

GMPE	Authors
$\ln PGA = 4.16 + 0.69\,M - 1.24\ln(R_{EPI} + 6) + 0.12\,S \pm 0.70$ --- $\ln PGV = -1.51 + 1.11\,M - 1.20\ln(R_{EPI} + 5) + 0.29S \pm 0.80$	Margaris et al. (2002)
$\log PGA = 1.07 + 0.45M - 1.35\log(R_{EPI} + 6) + 0.09\,F + 0.06\,S \pm 0.286$	Skarlatoudis et al. (2003)
$\log PGA = 0.883 + 0.458\,M - 1.278\log\left(\sqrt{{R_{EPI}}^2 + 11.515^2}\right) + 0.038\,S + 0.116\,F \pm 0.27$	Danciu and Tselentis (2007)
$\log PGV = -1.436 + 0.625\,M - 1.152\log\left(\sqrt{{R_{EPI}}^2 + 10.586^2}\right) + 0.026\,S + 0.086\,F \pm 0.283$ --- $\log Sa = a + b\,M - c\log\left(\sqrt{{R_{EPI}}^2 + h^2}\right) + e\,S + f\,F \pm \sigma$	Danciu and Tselentis (2007)
$\log PGV = -1.46 + 0.64\,M - 1.29\log(R_{EPI} + 6) + 0.02\,F + 0.14\,S \pm 0.32$	Skarlatoudis et al. (2007)
$\log PGA = 0.814 + 0.472\,M - 1.319\log\left(\sqrt{{R_{EPI}}^2 + 11.056^2}\right) + 0.047\,S + 0.097\,F \pm 0.298$	Sakkas (2016)
$\log PGA = 0.787 + 0.478M - 1.092\log\left(\sqrt{{R_{EPI}}^2 + 10.688^2} - 0.0044\sqrt{{R_{EPI}}^2 + 10.688^2} + 0.096\,S + 0.146\,F \pm 0.285\right)$ --- $\log PGV = -1.082 + 0.692\,M - 1.614\log\left(\sqrt{{R_{EPI}}^2 + 12.641^2}\right) + 0.137\,S + 0.31\,S + 0.068\,F \pm 0.306$	Chousianitis et al. (2018)

Table 3.3: The GMPEs that were selected in this thesis. REPI indicates the epicentral distance. S and F variables account for soil and focal mechanism type, respectively. Regarding the model proposed by Danciu and Tselentis (2007), the coefficient "a" is an intercept coefficient, "b" is a magnitude coefficient, "c" is a distance coefficient, "h" is a fictitious depth, "e" is a soil coefficient and "f" is a fault mechanism coefficient.

3.3 Creating the logic tree

In this thesis, PSHA was performed by computing PGA and PGV values for return periods of 475 and 950 years for Boeotia. In addition, PGA hazard curves and Uniform Hazard Spectra (UHS) in terms of Sa were constructed for Livadia and Thiva. The results were obtained by implementing a complex logic tree approach (Figure 3.5). The coefficient that describes the type of focal mechanism in all GMPEs (except for the one of Margaris et al., 2002) takes a value of 0 or 1 for normal and strike-slip/thrust ruptures, respectively. Given that most seismic zones include more than one focal mechanism type, the participation rate of each type was calculated for each zone of both adopted models, resulting in weight-specific GMPEs.

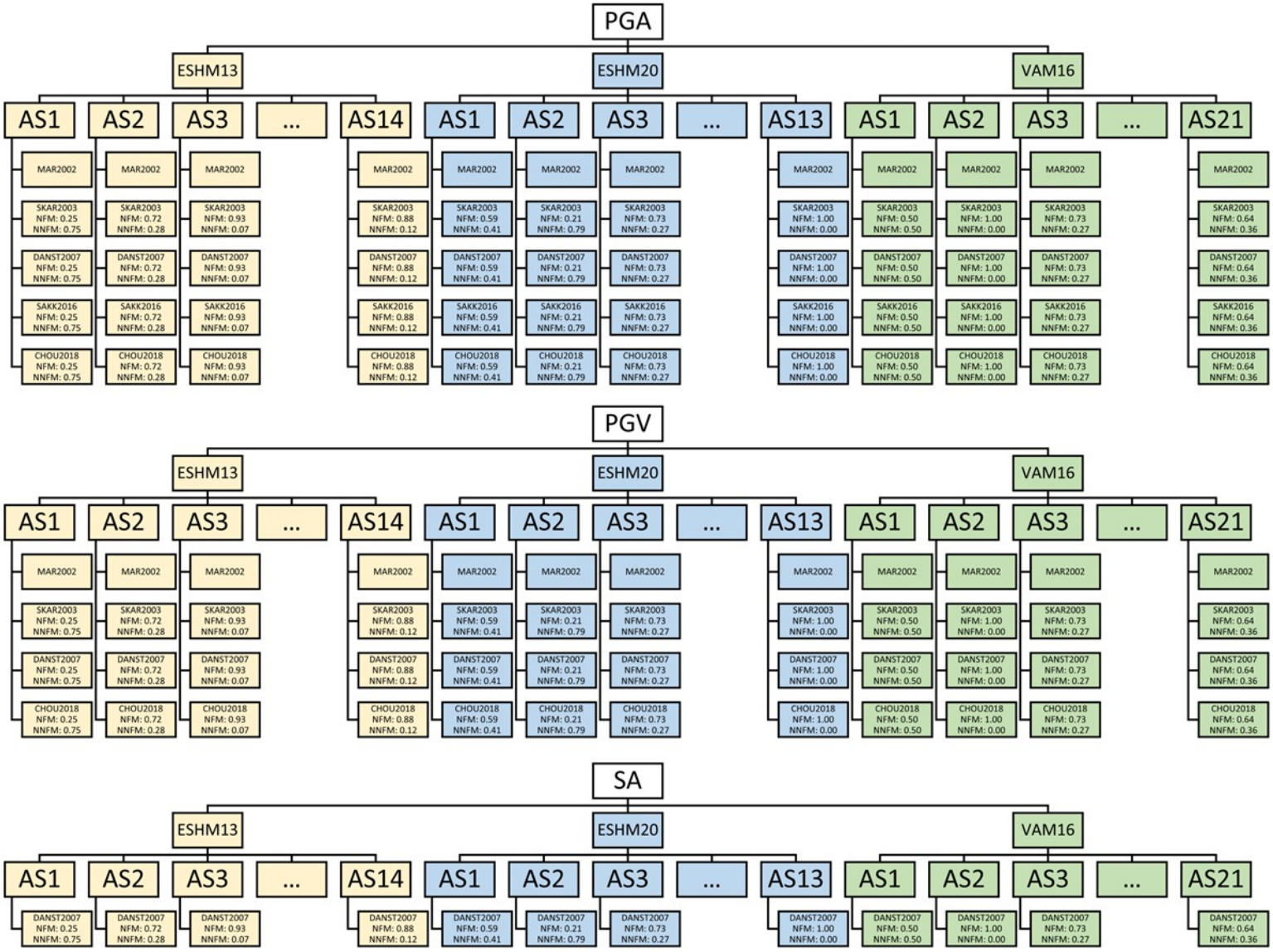

Figure 3.5: The logic tree approach that was used to compute PGA, PGV and Sa values.

3.4 Computational software

Two computational software were used to perform PSHA. The first one is the latest version of CRISIS, called R–CRISIS V20 (Ordaz et al., 2021). One fundamental benefit of CRISIS is the addition of a Graphical User Interface (GUI), written in the Visual Basic programming language. Furthermore, the new object–oriented technology, which produced an even more user–friendly GUI over the previous versions, was the aspect that was novel in R–CRISIS V20. The latter is critical because the user can observe dynamically the seismotectonic model, the FMD graphs and the random ruptures per area source.

The second applied software is the OpenQuake engine (OQ–engine) that was developed in the framework of the Global Earthquake Model (GEM) foundation by Pagani et al. (2014). The core of the OQ–engine was developed in Python. For an open–source scientific project, Python is released with an open–source license and has a widespread set of scientific and numerical modules that make it an appealing environment for interactive development between scientists and Information Technology (IT) developers.

One of the main features that differentiates the two software (apart from the fact that R–CRISIS is GUI–driven, whereas the OQ–engine is not) is the way they incorporate the logic tree approach into the computational process. R–CRISIS treats the constructed logic tree as a separate task, meaning that it is executed as a second run. This can be time–consuming, especially in logic trees such as the one of Figure 3.5 that has over 200 branches. In this regard, the novelty of the OQ–engine is its capability to process the logic tree as an integral part of a PSHA calculation. In addition, the OQ–engine adopts the Monte Carlo (MC) sampling modelling in its executions.

3.5 PSHA results using R–CRISIS V20

3.5.1 PGA maps (return periods of 475, 950 years)

PGA values that are computed using the R–CRISIS software via the logic tree approach, depicted in Figure 3.5, are presented in Figure 3.6. Concerning the spatial distribution of the PGA values for a return period of 475 years, the lowest values are observed to the northern part of Boeotia, whereas the highest values are mapped to the south, close to the Gulf of Corinth (Figure 3.6a). The highest PGA value for a return period of 475 years (Figure 3.6a) is ~300 cm/s^2, in an approximate distance of 20 km NW from Thiva and 40 km NE from Livadia. The lowest value was computed ~160 cm/s^2 at the northernmost edge of Boeotia at 23.10° and 38.58°.

Continuing for the larger return period of 950 years, the spatial PGA distribution remains similar, but the values increase, as obviously expected. The lowest value is ~200 cm/s^2, ~40 cm/s^2 larger than the previous return period, meaning that the low PGA values are not significantly affected (Figure 3.6b). However, the highest value is ~400 cm/s^2, indicating an increase of the order of ~100 cm/s^2.

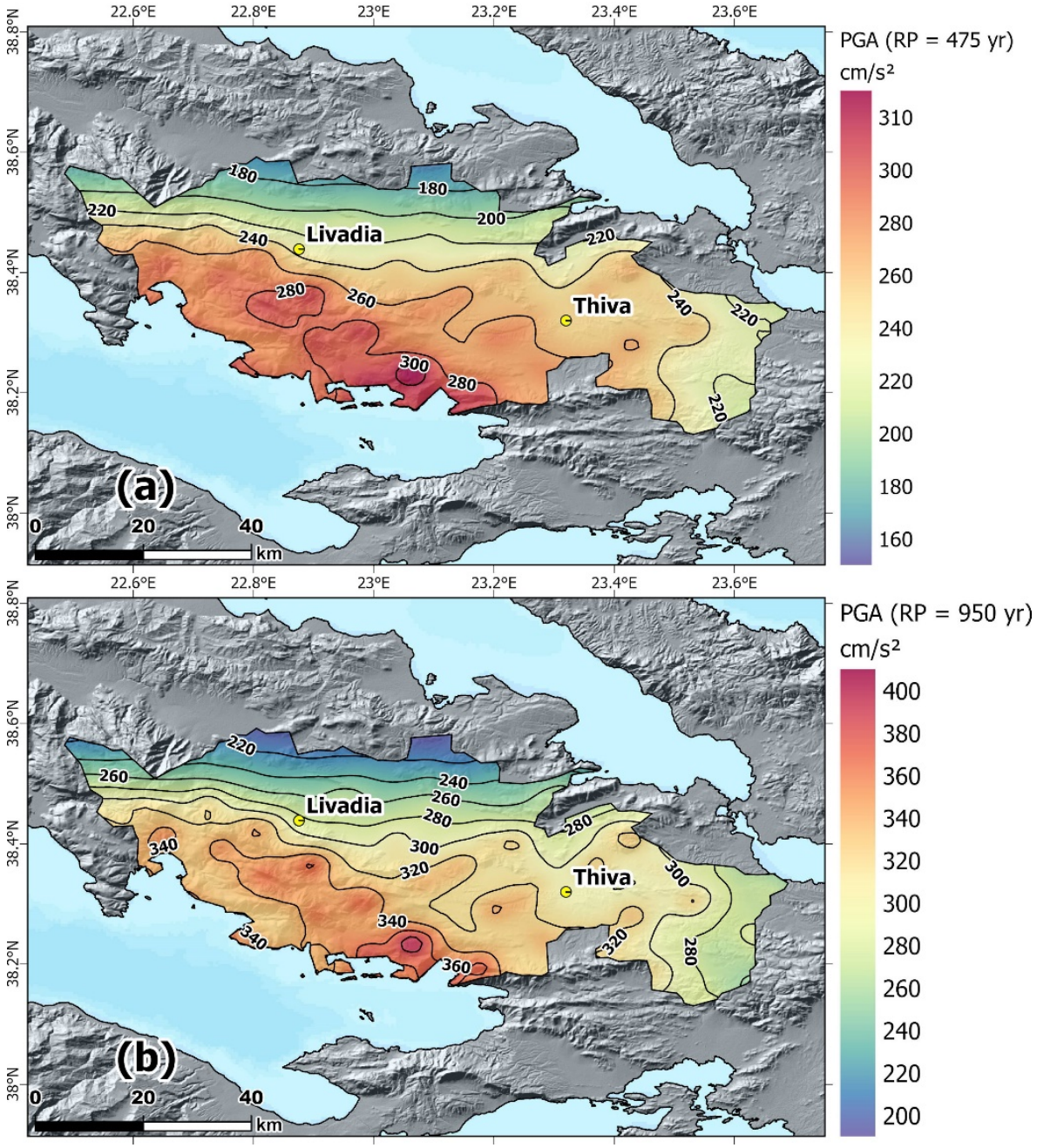

Figure 3.6: Distribution of PGA values in Boeotia for a return period of 475 (a) and 950 (b) years. The values are computed using the R–CRISIS software.

3.5.2 PGV maps (return periods of 475, 950 years)

The next ground motion parameter that was computed is PGV. The spatial distribution of the PGV values for the return periods of 475 and 950 years are depicted in Figure 3.7a and b, respectively. Regarding Figure 3.7a, the highest values are again to the south and the lowest to the north. The larger PGV value is ~17 cm/s, whereas the smaller one is ~8 cm/s. The highest PGV value for a return period of 950 years (Figure 3.7 b) is ~22 cm/s and the bottommost one is 10 cm/s. The PGV

values of the two return periods are not significantly different overall. The values for Livadia and Thiva are shown for both return periods and both parameters in Table 3.4.

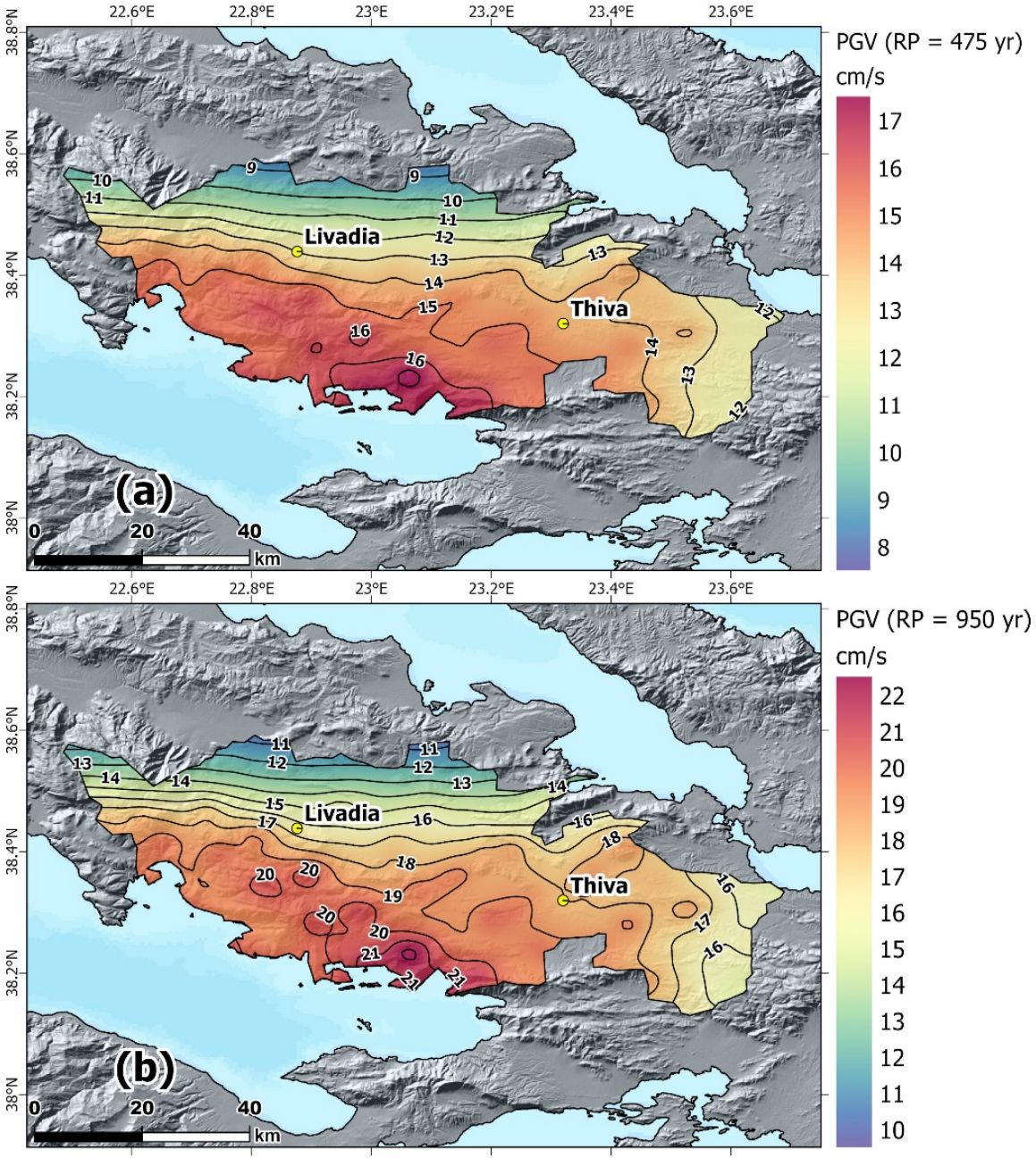

Figure 3.7: Distribution of PGV values in Boeotia for a return period of 475 (a) and 950 (b) years. The values are computed using the R–CRISIS software.

Return period (yr)	***475***		***950***	
Site	**PGA (cm/s^2)**	**PGV (cm/s)**	**PGA (cm/s^2)**	**PGV (cm/s)**
Livadia	236	13.0	288	16.6
Thiva	246	14.2	302	18.0

Table 3.4: PGA and PGV values for both return periods for Livadia and Thiva. The values are computed using the R–CRISIS software.

3.5.3 PGA hazard curves for Livadia and Thiva

When concentrating on one site, the PGA values for a plethora of return periods can be computed. Consequently, the PGA hazard curves for Livadia and Thiva were constructed for a stable occurrence time of 50 years (Figure 3.8). The town of Thiva possesses higher PGA values than Livadia for all probabilities of occurrence. In addition, PGA values do not exceed 1 g (~1000 cm/s^2) even in the lowest probabilities of exceedance, indicating that such extreme ground motions are not likely to occur at the major towns of Boeotia.

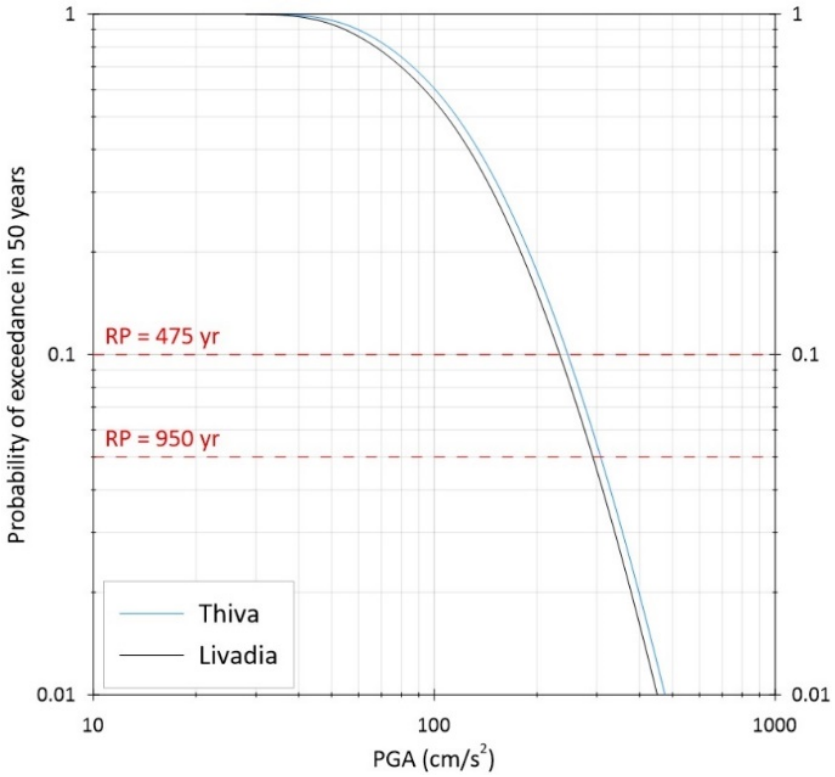

Figure 3.8: PGA hazard curves for Livadia (black) and Thiva (blue). The values are computed using the R–CRISIS software.

3.7.3 Uniform Hazard Spectra for Livadia and Thiva

UHS in terms of Sa were constructed for Livadia and Thiva (Figure 3.9) following the procedure described by the applied logic tree. Sa values were computed for the period range [0.1, 2.0] s, as proposed by Danciu and Tselentis (2007) in the description of their GMPE for a return period of 475 years. As also in the case of the hazard curves, the UHS of Thiva presents higher values than the one of Livadia. The peak of both curves is at the period value of 0.25 s, with the corresponding Sa value for Thiva being 410 cm/s^2, whereas for Livadia 380 cm/s^2. To summarize, the town of Thiva has higher seismic hazard than Livadia.

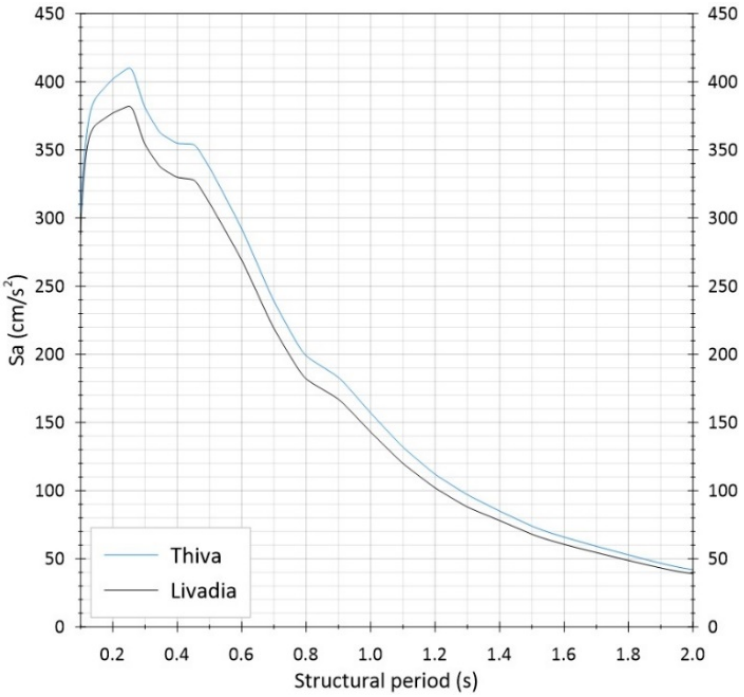

Figure 3.9: UHS for Livadia (black) and Thiva (blue). The values are computed using the R–CRISIS software.

3.6 PSHA results using the OpenQuake engine

3.6.1 PGA

PGA values were also calculated using the OQ–engine Python 3 module. The results are depicted in Figure 3.10. Regarding the spatial distribution of the PGA values for a return period of 475 years (Figure 3.10a), the lowest values are concentrated on the northern territory of Boeotia, whereas the highest values to the southeastern part of the study area. The highest PGA value for a return period of 475 years is ~400 cm/s^2 in an approximate distance of 10 km SE from Thiva. PGA also increases at the western part of Boeotia at a distance of ~50 km from Livadia, reaching values of ~350 cm/s^2. In addition, the lowest value was calculated 220 cm/s^2 to the northernmost edge of Boeotia.

For the second return period of 950 years, the spatial distribution of PGA remains similar (Figure 3.10b). The lowest value is ~260 cm/s^2, which is approximately 40 cm/s^2 larger than the respective one of the previous return period of 475 years. The highest value, which is identified at the southeastern part of the study area, is ~480 cm/s^2, indicating an important increase of the order of ~100 cm/s^2.

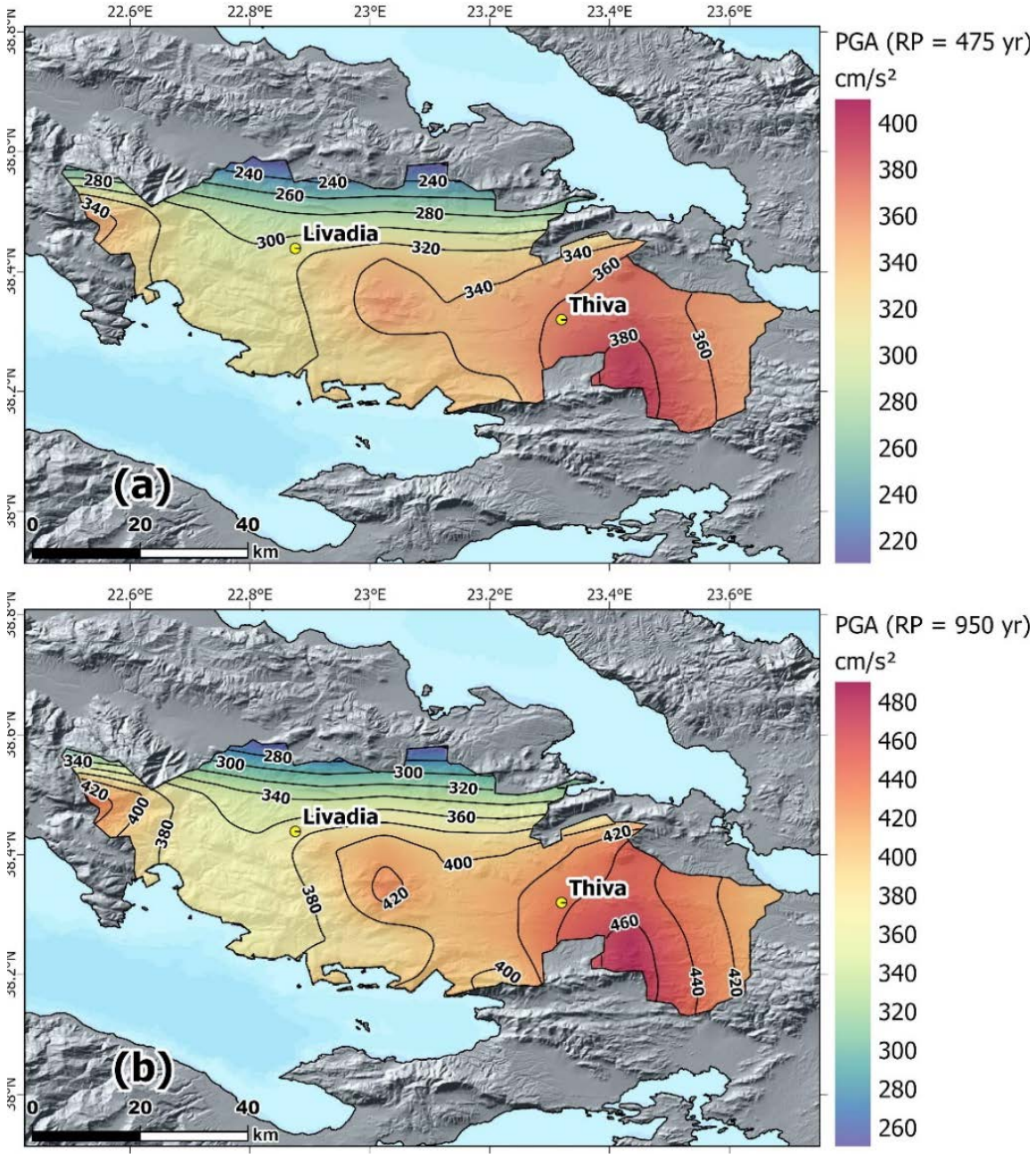

Figure 3.10: Distribution of PGA values in Boeotia for a return period of 475 (a) and 950 (b) years. The values are computed using the OQ–engine software.

3.6.2 PGV

Regarding PGV, the distribution pattern remains similar to the one of PGA for both return periods. For a return period of 475 years (Figure 3.11a), the greatest PGV value is ~24 cm/s, whereas the lowest ~10 cm/s. The largest PGV value for a return period of 950 years (Figure 3.11b) is ~30 cm/s and the bottommost one is 14 cm/s. The PGV values for the two return periods are not significantly different, as also in the R–CRISIS case. However, the OQ–engine produced higher values. PGA and PGV values for Livadia and Thiva are presented for both return periods in Table

3.5. When comparing them with the results obtained by R–CRISIS, the herein obtained values are generally higher.

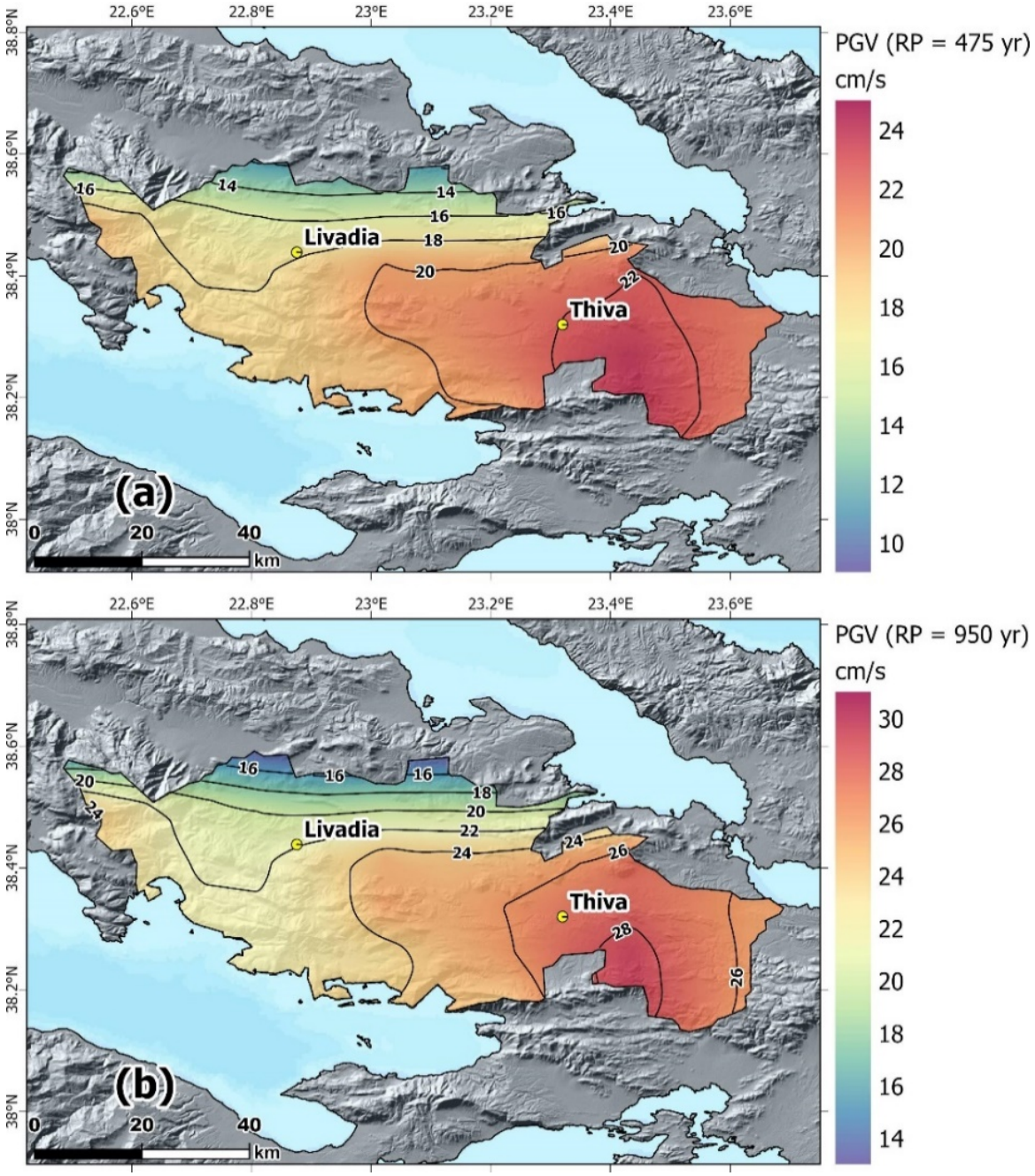

Figure 3.11: Distribution of PGV values of Boeotia for a return period of 475 (a) and 950 years (b) years. The values are computed using the OQ–engine software.

Return period	**475**		**950**	
Site	**PGA (cm/s^2)**	**PGV (cm/s)**	**PGA (cm/s^2)**	**PGV (cm/s)**
Livadia	310	17.8	366	21.9
Thiva	362	22.2	436	26.8

Table 3.5: PGA and PGV values for both return periods for Livadia and Thiva. The values are computed using the OQ–engine software.

3.6.3 PGA hazard curves for Livadia and Thiva

PGA hazard curves for Livadia and Thiva were constructed for the stable occurrence time of 50 years. The town of Thiva presents higher PGA values than Livadia for the entirety of probabilities of occurrence, meaning that has higher levels of seismic hazard (Figure 3.12). In addition, PGA values do not exceed 1 g (~1000 cm/s^2) even in the lowest probabilities of exceedance, indicating that such extreme ground motions are not likely to occur. The seismic hazard curves obtained using the OQ–engine resulted in higher PGA values, compared to the ones constructed with R–CRISIS, for all probabilities of exceedance in a stable 50 year framework.

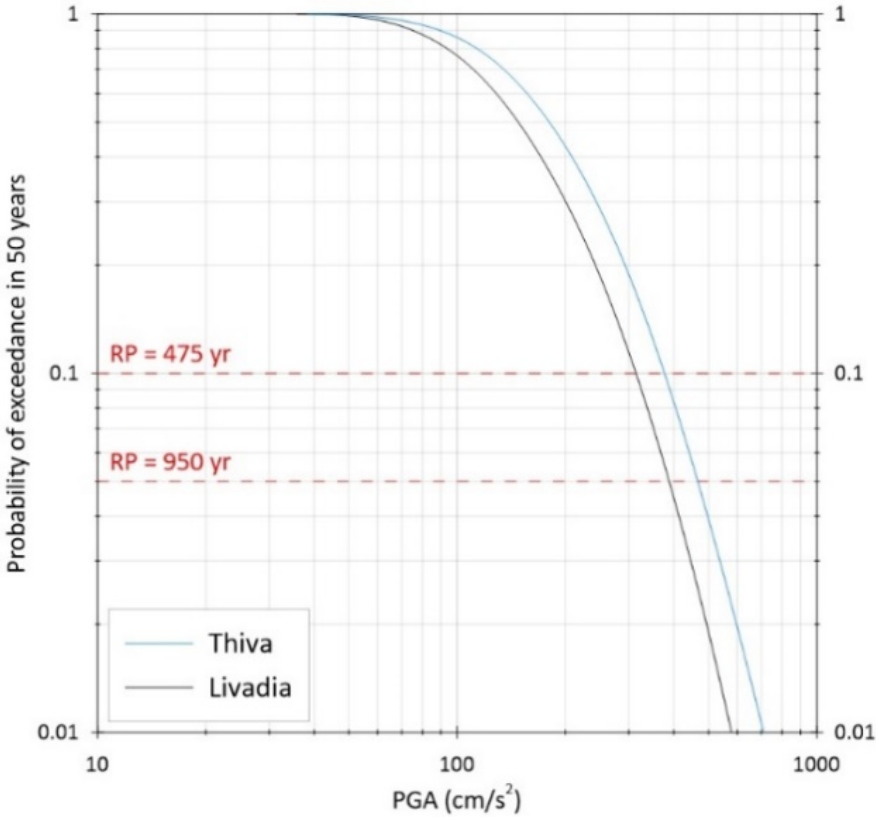

Figure 3.12: PGA hazard curves for Livadia (black) and Thiva (blue). The values are computed using the OQ–engine software.

3.7.3 Uniform Hazard Spectra for Livadia and Thiva

UHS in terms of Sa were also constructed for Livadia and Thiva (Figure 3.13) with the OQ–engine, taking into account only the GMPE of Danciu and Tselentis (2007) for the same period range. Thiva has higher Sa values than Livadia for all periods. The peak of the two curves is at the period value of 0.25 s, as with R–CRISIS. The greatest Sa value for Thiva is 550 cm/s^2, whereas for Livadia is 480 cm/s^2. To summarize, the town of Thiva has higher seismic hazard than Livadia. Moreover, the OQ–engine computed higher Sa values than R-CRISIS, of the order of 100 cm/s^2.

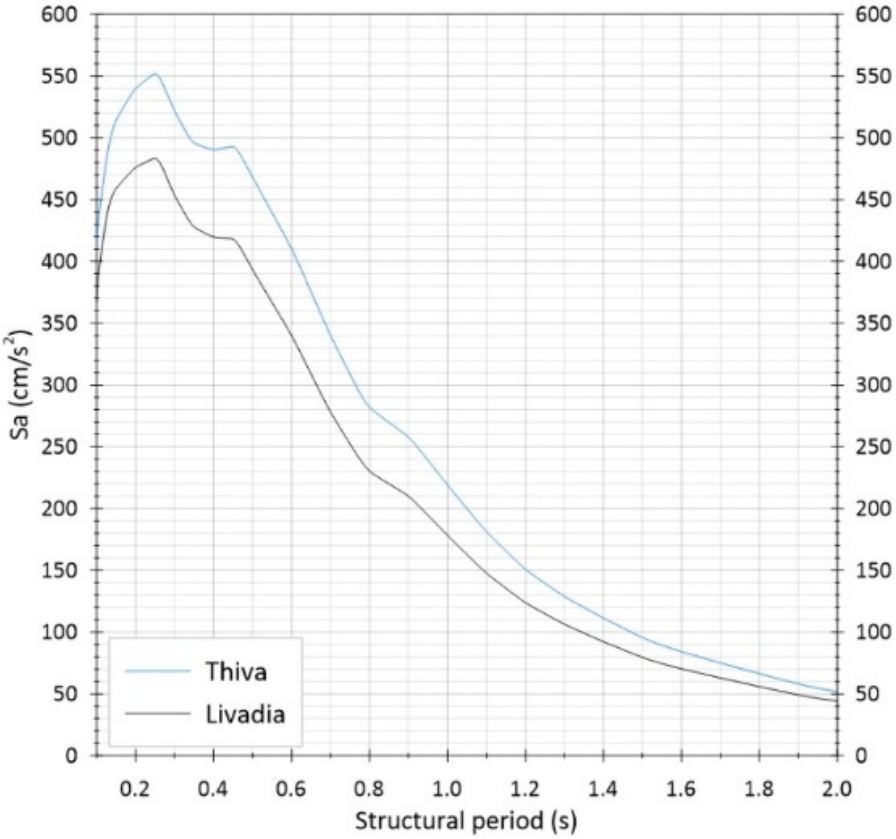

Figure 3.13: UHS for Livadia (black) and Thiva (blue). The values are computed using the OQ–engine software.

4 Stochastic Seismic Hazard Assessment for Boeotia

In order to perform physics–based seismic hazard assessment via stochastic modeling of PGA and PGV values, the user is required to input specific data that can be classified into three groups, namely, source, path, and site (Figure 4.1). It is essential to ensure that these parameters adequately characterize each case study, and the best way to achieve this is by comparing modeled PGA values to observed values from seismological stations. These stations should be located within or close to the case study area and should be distributed properly in azimuth. In cases where there is limited observed data availability, up to date GMPEs should be additionally utilized to enable a second comparison, which is less reliable. It is crucial to note that the most important aspect of comparing observed and modeled PGA or PGV values is to avoid trying to minimize the misfit only for the stations within or close to the study area. Such an approach can lead to the creation of amplifications in the remaining area, resulting in unrealistically high PGA values near the modeled ruptured plane. Therefore, the user must always compare observed and modeled IML for all the distances.

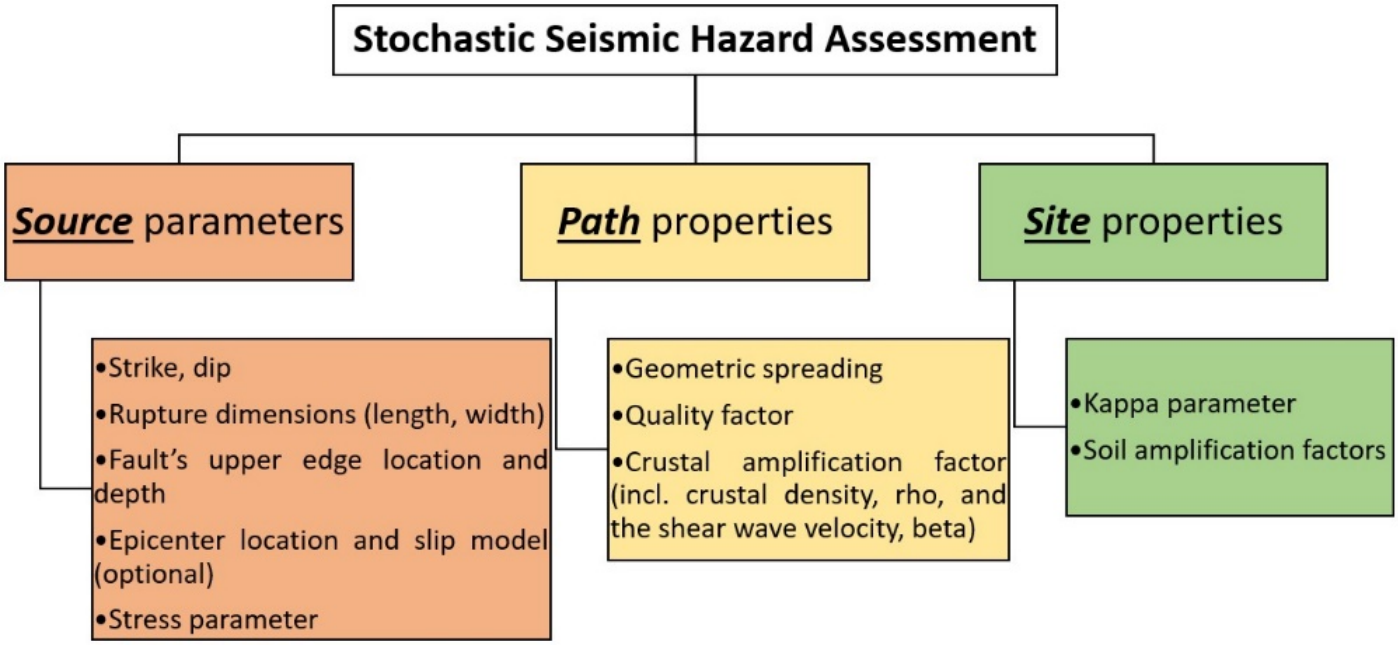

Figure 4.1: The required user input data for performing stochastic seismic hazard assessment.

4.1 Source parameters

Regarding the source parameters, the user is expected to provide information on the strike, dip and the dimensions of the causative fault. In addition, the location and the depth of the upper edge must be inserted to the input data. Regarding the hypocenter, the user must provide its location on the causative fault in terms of along–strike and along–dip, with reference to the upper edge, as indicated at the Figure 4.2. The last source parameter that needs to be defined is the stress parameter.

The notion of the stress parameter is often confused with stress drop, which was initially introduced as a means of measuring final fault slip in relation to fault dimension. Stress drop gained prominence in earthquake source parameters following Brune (1970), who demonstrated that the

far–field spectrum of shear waves could be explained using two source parameters: the seismic moment and the stress drop. This enabled the measurement of stress drop from seismic signals, and it subsequently became a crucial factor in engineering seismology after the work of Hanks and McGuire (1981) that showed that it could be utilized to model high–frequency ground motion. However, it has been observed that actual static stress drop values were generally lower than the 100–bar parameter used by Hanks and McGuire (1981) to match observed ground motion values in California. Moreover, highly variable stress drop values for the same earthquake have been reported (Atkinson and Beresnev, 1997). As a result, the value of stress drop as a descriptive source parameter for engineering seismology is questionable, especially as it may not accurately reflect stresses in the real earth or on the fault surface for complex ruptures.

Therefore, in the present thesis, the term "stress drop" will not be utilized to refer to the final source parameter. Instead, it will be substituted with the term “stress parameter”. The process for determining the stress parameter involves a standard procedure of matching modeled with observed values of acceleration (Atkinson and Assatourians, 2014; Raghucharan and Surendra Nadh Somala, 2018; Bonatis, 2020; Kaviris et al., 2022b). An alternative method is to employ the average stress parameter values that have been reported for various countries, such as the ones in the study by Margaris and Boore (1998), who found a mean stress parameter of 56 bars for Greece.

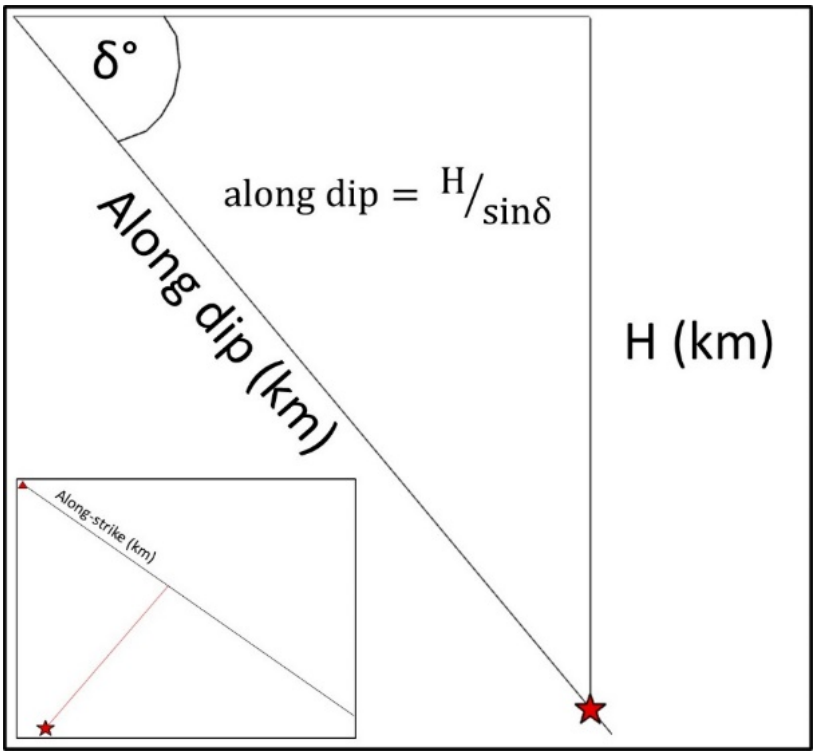

Figure 4.2: The measurements of along–strike and along–dip distances that are determined from a reference point situated at the upper edge, marked by a triangle symbol, of the fault. The fault is represented by a black line in the map projection which is illustrated in the lower left figure. To estimate the termination of the along–strike distance, a red line starting from the epicenter, perpendicular to the fault line, is drawn in the map. The along–dip distance is estimated by the fraction of the focal depth, H, and the sinus of the dip angle, δ.

4.2 Path properties

Geometrical spreading refers to the reduction in energy density that arises as an elastic wavefront expands. In a homogenous Earth, characterized by uniform velocity and density, the geometrical spreading of a seismic body wave is directly proportional to the inverse of the distance between the source and receiver (Cormier, 1990). Atkinson (2004) proposed different geometrical spreading values for three distance intervals (<70 km, 70–130 km, and >130 km) based on the predominant type of wave in the seismic signal. The Fourier spectral amplitudes exhibit a decay of $R^{-1.0}$, where R denotes the hypocentral distance, in the region extending up to 70 km from the source. In the range of 70–140 km, a transition zone exists, wherein the direct waves coexist with the ones that are generated by total reflection. The attenuation in this zone can be characterized as $R^{0.0}$. Further away from the source, i.e., beyond 140 km, the attenuation follows a well–defined pattern of $R^{-0.5}$, which is representative of two–dimensional geometric spreading.

It is important to state that the geometrical spreading and the anelastic attenuation are fundamentally different. The elastic energy is inevitably converted into other forms of energy that are irreversible. Had this not been the case, a body that has been excited elastically would oscillate indefinitely. The phenomenon of anelastic attenuation is responsible for the dissipation of elastic energy, and its investigation is crucial for multiple reasons. In particular, since attenuation influences wave amplitudes and shapes, it is imperative to account for its variations during the generation of synthetic waveforms (Pujol, 2003). Anelastic attenuation is parameterized by the quality factor, Q (Lay and Wallace, 1995). The quality factor can be expressed as a function of frequency via the equation (4.1).

$$Q(f) = Q_0 f^n \tag{4.1}$$

where Q_0 reflects the degree of heterogeneity of the medium, and the exponent n is proportional to the seismic activity of the area under consideration (Raghukanth and Nadh Somala, 2009). Seismically active zones are typically characterized by low Q_0 values and high n values, whereas more stable regions display higher Q values coupled with lower n values (Singh et al., 2004).

4.3 Site properties

The site properties (Figure 4.1) that will be discussed in detail solely depend on the prevailing soil conditions. Diverse soil types may be recognized via the computation of the average seismic shear–wave velocity from the surface to a depth of 30 meters (V_{S30}). Various site classification schemes have been introduced over the years, which delineate dissimilar soil types within specific V_{S30} range values. The National Earthquake Hazards Reduction Program (NEHRP) and the Eurocode 8 (EC8) are among the most widely recognized international site classification systems. Their respective site classification schemes have been summarized in Table 4.1.

To evaluate how the seismic motion is affected by the shallower sedimentary layers, the soil amplification factors, and the kappa parameter are used. The kappa parameter (κ_0), which acts as a low–pass filter, is defined by Anderson and Hough (1984) as an exponential decay that represents the diminution factor, D(f) (Ktenidou et al., 2014). The equation that expresses this factor used in stochastic modeling in relation to the kappa parameter is as follows:

$$D(f) = e^{-\pi \kappa_0 f} \tag{4.2}$$

Average shear wave velocity V_{S30} (m/s)		
Site Class	NEHRP	EC8
A	$V_{S30} > 1500$	$V_{S30} > 800$
B	$760 < V_{S30} \leq 1500$	$360 \leq V_{S30} \leq 800$
C	$360 < V_{S30} \leq 760$	$180 \leq V_{S30} \leq 360$
D	$180 < V_{S30} \leq 360$	$V_{S30} < 180$
E	$V_{S30} < 180$ (soil)	–
F	$V_{S30} < 180$ (soil requiring specific evaluation such as liquefiable soils, peat and high plasticity clay)	–

Table 4.1: Site classification system according to NEHRP and Eurocode 8 (EC8).

The meaning behind the kappa factor remains unclear. While some studies, such as the work of Hanks (1982) and Atkinson (2004), argue that it is a site–specific effect connected to the quality of the materials in the proximity of the source, others like Papageorgiou and Aki (1983) suggest that it is linked to source processes related to the size of a minimum cohesive zone. It is also possible that kappa may have origins from both the source and the site, as indicated by Atkinson (1996). The present thesis aims to treat the kappa parameter as a site–specific property to enhance the categorization of input parameters.

Multiple studies have been conducted in order to determine the kappa values applicable for large earthquakes in Greece (Hatzidimitriou, 1993; Margaris and Boore, 1998; Klimis et al., 1999; Ktenidou et al., 2013, 2014). Hatzidimitriou (1993) used a dataset of accelerograms recorded at sites varying from very soft to stiff soil conditions and estimated an average κ_0 value of 0.06. The same average value was obtained from Margaris and Boore (1998) Margaris and Boore (1998) and Klimis et al. (1999) also estimated k_0 values for different site classes, based on the range of V_{S30} values (Table 4.2).

Ref.	κ_0	V_{S30} (m/s)
Margaris and Boore (1998)	0.035	>760
	0.050	$360 < V_{S30} \leq 760$
	0.060	$180 < V_{S30} \leq 360$
Klimis et al. (1999)	0.044	$360 < V_{S30} \leq 760$
	0.066	$180 < V_{S30} \leq 360$

Table 4.2: Kappa values proposed by Margaris and Boore (2008) and Klimis et al. (1999) for different ranges of V_{S30} values.

The final parameters of interest are the soil amplification factors, represented in a tabular format with two columns, consisting of a frequency range value and its corresponding amplification factor. It is evident that different soil classifications possess distinct amplification factors (Table 4.3). The classification according to NEHRP and EC8 is determined based on the range of V_{S30} values (Table 4.1). Margaris and Boore (1998) proposed amplification factors for site classes A–C, while Klimis et al. (1999) revised the amplification factors for site class C and added the amplification factors for site class D (Table 4.3).

Site Class A		Site Class B		Site Class C		Site Class D	
Freq. (Hz)	Ampli.	Freq. (Hz)	Ampli.	Freq. (Hz)	Ampli.	Freq. (Hz)	Ampli.
0.01	1.00	0.01	1.00	0.11	1.076	0.09	1.125
0.10	1.06	0.09	1.21	0.15	1.107	0.10	1.142
0.24	1.13	0.16	1.32	0.31	1.253	0.19	1.307
0.45	1.22	0.51	1.59	0.50	1.504	0.35	1.742
0.79	1.38	0.84	1.77	0.66	1.763	0.46	1.993
1.38	1.65	1.25	1.96	1.10	2.219	0.50	2.094
1.93	1.86	2.26	2.25	1.78	2.633	1.03	3.347
2.85	2.05	3.17	2.42	2.11	2.751	1.15	3.536
4.03	2.17	6.05	2.70	2.67	2.898	1.52	3.909
6.34	2.28	16.60	3.25	3.51	3.029	1.98	4.113
12.54	2.38	61.20	4.15	5.40	3.243	3.09	4.376
21.23	2.42			8.01	3.446	5.34	4.722
33.39	2.44			12.24	3.659	7.07	4.918
82.00	2.46			24.16	3.990	9.39	5.051
				34.04	4.121	14.87	5.195
				62.50	4.306	40.50	5.461

Table 4.3:Amplification factors for different site classes. Specifically, site classes A and B were assigned amplification factors proposed by Margaris and Boore (1998), while site classes C and D were assigned amplification factors suggested by Klimis et al. (1999). The classification system of NEHRP was used.

4.4 Earthquakes for calibration in broader Boeotia

To ensure accurate calibration of the parameters related to path and site properties, suitable events must meet specific criteria. First, they must have been recorded by seismological stations located both within and outside the study area. This allows for meaningful comparison between modeled and observed ground motions. Recorded data from locations outside the study area is particularly important in calibrating models to accurately describe broader path parameters. If models are calibrated solely based on data recorded within the study area, there is a risk of inaccurately inverting parameters, leading to the generation of unrealistic results for close source distances. Secondly, it is important that the causative faults of the events are well–known and documented. This information is crucial in parameterizing accurate source properties. Lastly, the stress parameter must be calibrated, mostly via a trial–and–error method. By adhering to these criteria, the calibration process can be more accurately carried out, leading to improved results.

To identify suitable earthquakes, two freely available databases were utilized, namely the Engineering Strong Motion (ESM) (https://esm-db.eu/#/home) and the GIS Hellenic Accelerograms Database (GHEAD) (http://ghead.itsak.gr/map/). The ESM database provides users with a range of tools to search, select and download ground–motion data and associated metadata since 1969 (Luzi et al., 2016). This database is continuously being updated, with recent earthquakes being incorporated into the existing database. The database contains waveforms that are associated with earthquakes having a magnitude greater than or equal to 4.0, primarily recorded in the European–Mediterranean region and the Middle East. On the other hand, the GHEAD database comprises 1097 three–component accelerometric waveforms associated with 401 earthquakes that occurred in the broader Aegean area, also with magnitudes equal to or greater than 4.0, covering the time period from 1973 to 2010. For post–2010 earthquakes, the European Integrated Data Archive (EIDA) provides an online platform for users to search and acquire

unprocessed waveform data from the Hellenic Seismic Network, which is hosted at the National Observatory of Athens (NOA). When an earthquake has been documented in both the EIDA and ESM databases, the latter is preferred, given that it contains processed waveform data, and the PGA values have been assigned to all stations, irrespective of whether it is a seismograph or accelerograph.

In order to determine the path and site properties, the simulation of three earthquakes (instead of one) was deemed necessary due to limitation in data availability. The number of stations with records for both earthquakes within Boeotia or at distances not exceeding 10 km is limited, thus the use of more than one earthquake is critical to cover as many data points as possible for the broader Boeotia region. The three selected earthquakes were the 15/06/1995 Ms = 6.2 Aigion, the 07/09/1999 Mw = 6.0 Athens and the 19/07/2019 Mw = 5.1 earthquakes (Figures 4.3, Figure 4.5 and Figure 4.7). All events have been recorded in many seismological stations. However, the Aigion earthquake was recorded at two stations within or close to Boeotia, namely LEVA and AMIA (Figure 4.3), the Athens 1999 earthquake was recorded at three stations, namely THVC, THV1, and ATLA (Figure 4.5) and the Athens 2019 earthquake was recorded at one station, THV1 (Figure 4.7). Despite the limited data availability, the use of this data is preferred over relying solely on GMPEs for comparison between simulated ground motions.

4.4.1 The 15/6/1995 Ms = 6.2 Aigion earthquake

The 15/06/1995 Ms = 6.2 Aigion earthquake caused extensive damage in the Western Gulf of Corinth (WGoC) (Figure 4.3). This earthquake inflicted severe damage to Aigion town, which is located on the southern coastline of the WGoC, resulting in the damage of over 2,000 structures, the collapse of two buildings and 26 casualties (Bernard et al., 1997). In the study of Bernard et al. (1997), data from seismology (including local, regional and teleseismic records of the mainshock and its aftershocks), geodesy (GPS and SAR interferometry), and tectonics were used to relocate the hypocenter of this seismic event. According to their findings, the epicenter was located 15 km NNE from the damaged city of Aigion. The mainshock ruptured a normal fault with low dip angle (Figure 4.3). The parameters utilized for characterizing the properties of the source, path, and site have been derived from the recent study conducted by Kaviris et al. (2022c), except for the stress parameter, which was re–estimated. The principal aim of their research was to simulate seismic events in the WGoC, and the authors calibrated the path and site related parameters by means of simulating the Aigion earthquake (Table 4.4).

In order to calibrate the necessary parameters, two graphs were created. The first graph presents a comparison among modeled PGA values, estimated PGA values using selected GMPEs and observed PGA values at the stations illustrated in Figure 4.3 (Figure 4.4a). The graph offers a comprehensive overview of the modelled PGA distribution for different Joyner and Boore distances (R_{jb}). The second graph (Figure 4.4b) pertains solely to the comparison of modeled and observed PGA values. This graph serves as a valuable tool for visually assessing the degree of deviation between modeled and observed values, as significant deviations from zero suggest a lack of comparability between the two sets of values.

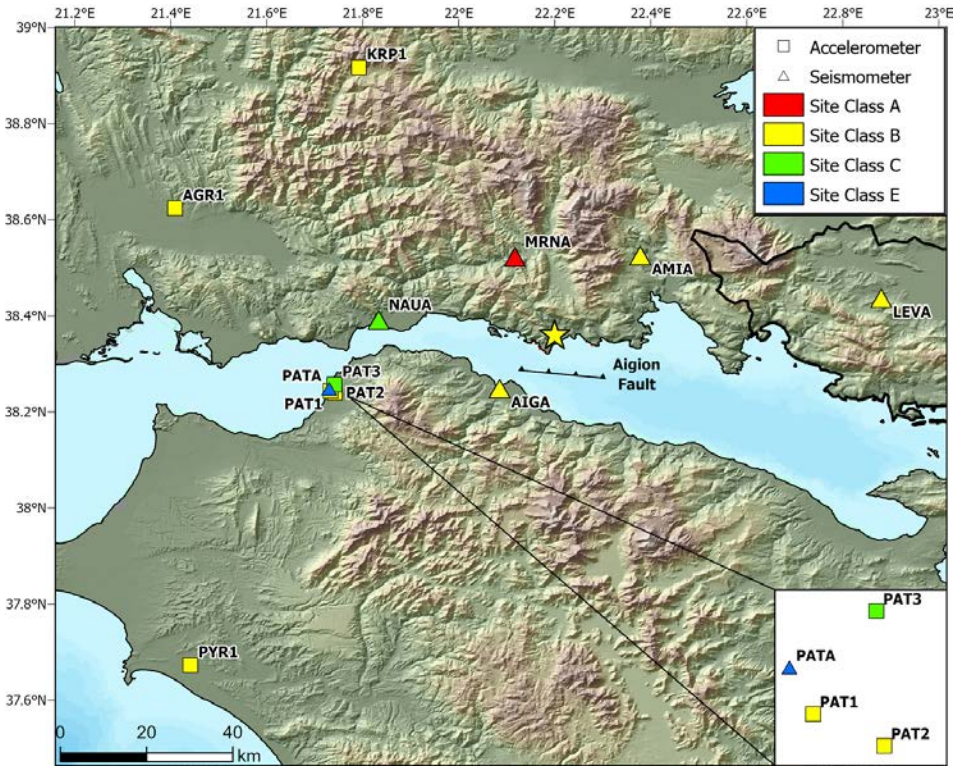

Figure 4.3: The epicenter and the causative fault of the Aigion 1995 earthquake, according to Bernard et al. (1997). The seismological stations that recorded the earthquake are presented. The Site Classes have been based on the EC8 classification system (Table 4.1).

Parameter	**Value**	**Reference**
Strike	277°	Kaviris et al. (2022c)
Dip	33°	Kaviris et al. (2022c)
Depth of the upper edge	5 km	Kaviris et al. (2022c)
Fault dimensions (Length × Width)	15 km × 9 km	Kaviris et al. (2022c)
Mw	6.5	Kaviris et al. (2022c)
Stress parameter	65 bars	This study
Kappa parameter (k_0)	0.044	Klimis et al. (1999)
Quality factor	$100f^{0.8}$	Hatzidimitriou (1993)
Geometrical spreading (R^n)	n = -1.0, R < 70 km n = 0.0, 70 km ≤ R < 130 km n = -0.5, R ≥ 130 km	Atkinson (2004)
Site amplification	Adopted from Klimis et al. (1999)	

Table 4.4: The parameters utilized for the stochastic ground motion modeling of the Aigion 1995 earthquake executed with the EXSIM code.

Regarding the first graph (Figure 4.4a), it can be observed that the modeled PGA values exhibit a good resemblance to the estimated PGA values obtained through GMPEs. Nonetheless, it is apparent that certain seismological stations with larger Joyner and Boore distances have recorded PGA values greater than others with smaller distances. Turning to Figure 4.4b, it can be noted that more than half of the data points exhibit natural logarithm ratios [ln(Obs. PGA/Mod. PGA)] in the

range of [-0.5, 0.5], indicating a strong correlation between the observed and modeled PGA values (Dang et al., 2021). Consequently, the parameters presented in Table 4.4 adequately describe the site and path characteristics of the WGoC and the western part of Boeotia (Figure 4.3).

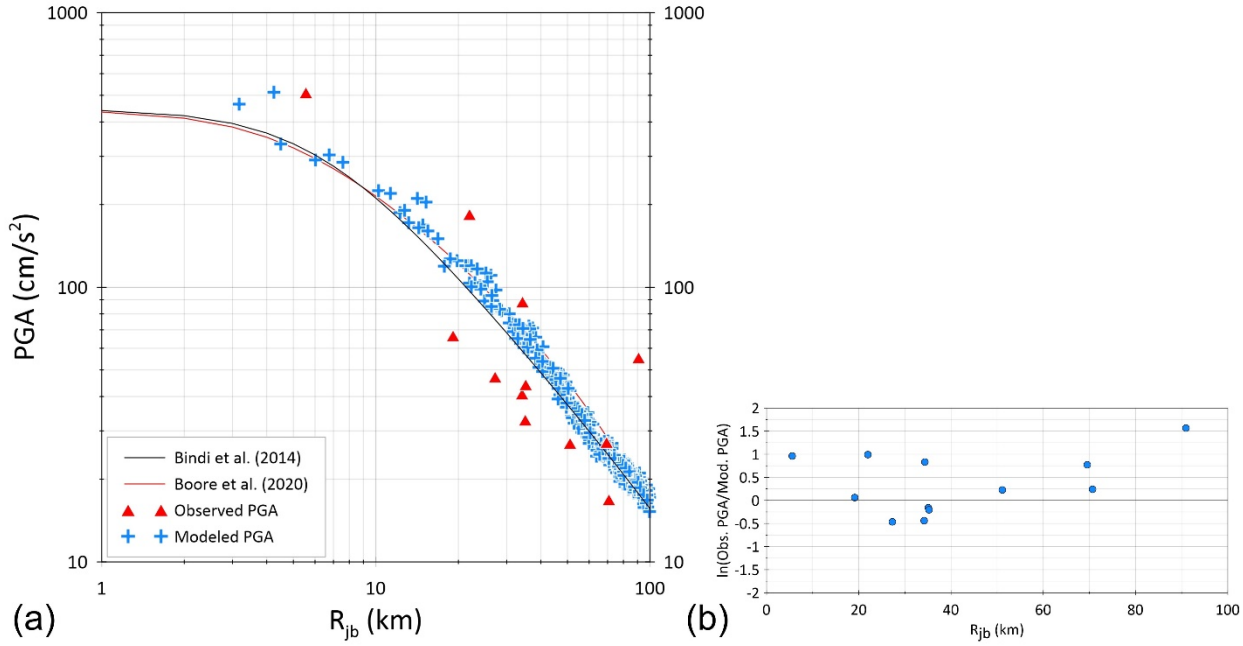

Figure 4.4: (a) the comparison of PGA values obtained from: i. recordings, represented by red triangles, ii. the GMPEs of Boore et al. (2020) and Bindi et al. (2014), indicated by lines, and iii. stochastic modeling, shown as crosses, plotted against the Joyner and Boore distance (R_{jb}). (b) Distribution of the residuals among observed and simulated PGA values against Joyner and Boore distance.

4.4.2 The 7/9/1999 Mw = 6.0 Athens earthquake

On 07/09/1999, a highly destructive earthquake, with a moment magnitude of Mw = 6.0, occurred 20 km northwest of Athens, as reported by several studies (Ganas et al., 2001; Louvari and Kiratzi, 2001; Voulgaris et al., 2001; Papadimitriou et al., 2002; Papadopoulos, 2002). Prior to this event, Western Attica was considered of low seismic hazard. The earthquake caused severe damage to the Greek capital, with more than 100 buildings collapsing, 143 fatalities, and an estimated cost exceeding three billion dollars (Kouskouna and Malakatas, 2000; Papadimitriou et al., 2002; Papadopoulos, 2002). It is, therefore, considered one of the most catastrophic earthquakes that has occurred in Greece over the last few centuries. Papadimitriou et al. (2002) relocated the epicenter using data from the Cornet local permanent network (Kaviris, 2003) and teleseismic recordings, determining that the earthquake ruptured a normal fault with an approximate E–W direction. Their fault plane solution indicated strike and dip values of 105° and 55°, respectively. In addition, they also provided information about the length and the width of the causative fault, which is essential for the finite fault stochastic ground motion simulation.

In a recent study by Kapetanidis et al. (2020), the aftershocks of the 1999 Athens earthquake were relocated utilizing a custom velocity model for Attica and the double–difference technique. Notably, the mainshock's spatial parameters were adopted from the work of Papadimitriou et al. (2002). Kapetanidis et al. (2020) concluded that the seismogenic fault was "blind". Based on their findings, the Thriassio and Fili faults (Figure 4.5) were identified as potential causative faults; however, the researchers did not definitively identify which fault was responsible for the 1999

Athens earthquake. Nevertheless, the authors proposed a least–squares fault plane by analyzing the relocated clusters within the sequence. The strike and dip values of this plane were similar to those proposed by Papadimitriou et al. (2002), with a difference of only 13° in strike (118° versus 105°) and 7° in dip (48° versus 55°). The negligible variation in the dip values suggests that the along dip distance will not be significantly affected by selecting either dip value. The only parameter that was not documented in either study was the depth of the fault's upper edge. To estimate this parameter, the seismic cross–sections of Kapetanidis et al. (2020) for the 1999 sequence were employed and the value of 5 km was selected. In conclusion, the source parameters provided by Papadimitriou et al. (2002) were adopted, and the cross–sections from Kapetanidis et al. (2020) were utilized to estimate the burial depth of the upper edge of the theoretical causative fault. A summary of all parameters is presented in Table 4.5.

The stress parameter value of 80 bar was selected for the finite fault stochastic ground motion simulation. As previously explained in the calibration chapter, this process entails a trial–and–error method that involves multiple iterations to converge on the optimal stress parameter value. The goal of this process is to obtain the most precise predictions of ground motion. During the calibration procedure of two (out of three) earthquakes, the stress parameter value of 80 bar yielded the most accurate predictions of ground motion.

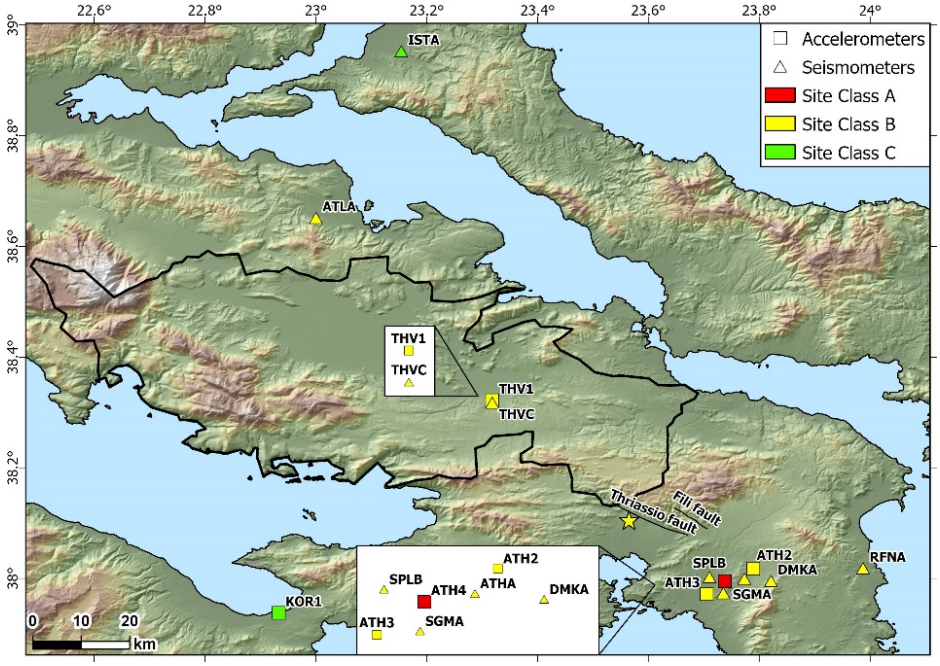

Figure 4.5: The epicenter and the causative fault of the Athens 1999 earthquake, as documented by Papadimitriou et al. (2002) and Kapetanidis et al. (2020). Notation as in Figure 4.3.

The two calibration graphs were produced similar to the Aigion 1996 case. The first graph (Figure 4.6a) demonstrates a strong correspondence between the modeled and observed PGAs. The theoretical regression line for the observed PGA values aligns closely with the modeled data, indicating that the geometrical spreading and anelastic attenuation parameters were accurately modeled for the Athens earthquake. Notably, if a theoretical power regression line with a Root Mean Square error of only 30% were plotted alongside the observed PGA data, it would closely resemble the distribution of the modeled PGA values. In Figure 4.6 b, it can be observed that over 80% of the data points demonstrate natural logarithm ratios [ln(Obs. PGA/Mod. PGA)] within the

range of [0.0, 0.4], indicating a stronger correlation between observed and modeled PGA values than was observed in the calibration of the Aigion event. The PGA values estimated by the two GMPEs exhibit a highly favorable correlation with the modeled PGA values. Therefore, the parameters presented in Table 4.5 describe the site and path characteristics of the broader area around the epicenter of the Athens 1999 event, which encompasses the eastern part of Boeotia located within a distance of 100 km from the Thriassio fault (Figure 4.5). As the same parameters were used in the calibration of the Aigion event, it is justifiable to apply them to the properties within Boeotia without excessive extrapolation.

Parameter	**Value**	**Reference**
Strike	105°	Papadimitriou et al. (2002)
Dip	55°	Papadimitriou et al. (2002)
Depth of the upper edge	5 km	Kapetanidis et al. (2020)
Fault dimensions (Length × Width)	15 km × 10 km	Papadimitriou et al. (2002)
Mw	6.0	Papadimitriou et al. (2002)
Stress parameter	80 bars	This study
Kappa parameter (k_0)	0.044	Klimis et al. (1999)
Quality factor	$100f^{0.8}$	Hatzidimitriou (1993)
Geometrical spreading (R^n)	n = -1.0, R < 70 km n = 0.0, 70 km ≤ R < 130 km n = -0.5, R ≥ 130 km	Atkinson (2004)
Site amplification	Adopted from Klimis et al. (1999)	

Table 4.5: The modeling parameters utilized for the stochastic ground motion modeling of the Athens 1999 event with EXSIM.

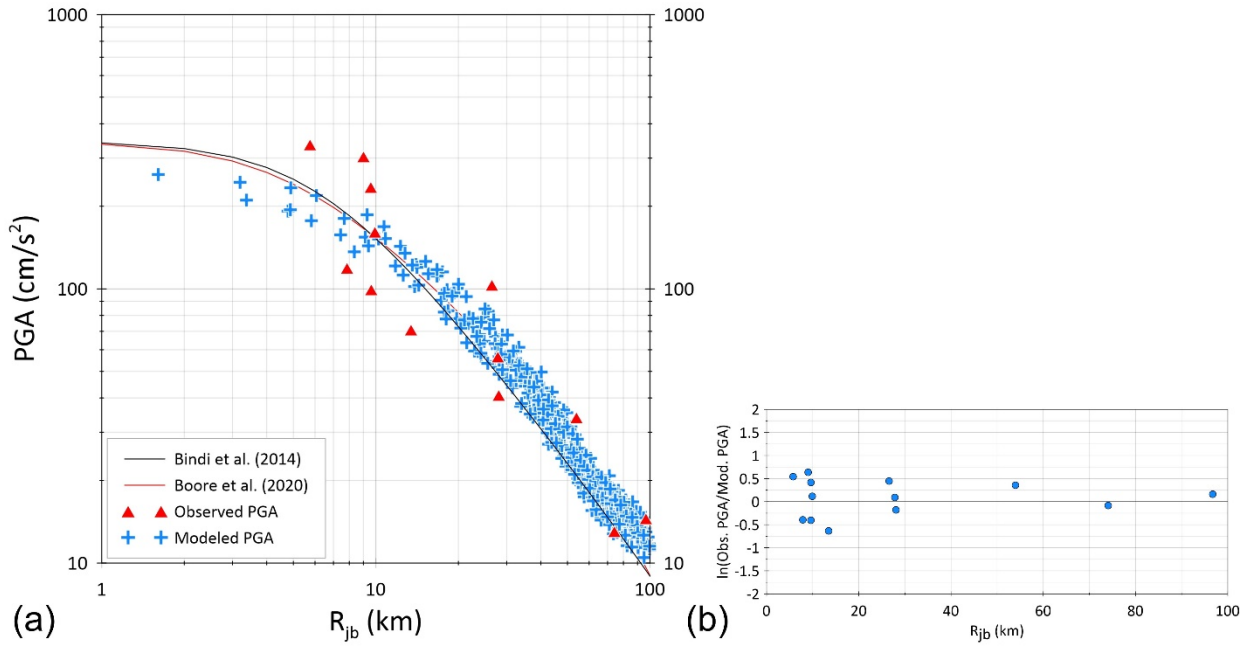

Figure 4.6: (a) the comparison of PGA values obtained from: i. recordings, represented by red triangles, ii. the GMPEs of Boore et al. (2020) and Bindi et al. (2014), indicated by lines, and iii. stochastic modeling, shown as crosses, plotted against the Joyner and Boore distance (R_{jb}). (b) Distribution of the residuals among observed and simulated PGA values against Joyner and Boore distance.

4.4.3 The 19/7/2019 Mw = 5.1 Athens earthquake

Approximately two decades after the Athens 1999 earthquake, an earthquake of magnitude Mw = 5.1 occurred in the same epicentral region on 19/07/2019, resulting in substantial damage to the western suburbs of Athens (Kouskouna et al., 2021). Kapetanidis et al. (2020) conducted a relocation analysis of this earthquake sequence. Additionally, Kouskouna et al. (2021) performed a relocation analysis of the 2019 event and evaluated its macroseismic intensities. The main difference between these studies in the relocation process lies in the velocity model utilized. Kapetanidis et al. (2020) employed a custom velocity model for Athens, while Kouskouna et al. (2021) assessed various proposed velocity models from the literature and adopted the one that yielded the minimum location errors. The parameters necessary to conduct finite–fault ground–motion simulation provided by both studies are comparable (Table 4.6). However, the parameters chosen are those suggested by Kapetanidis et al. (2020) because of the utilization of the custom Athens velocity model. These parameters stem from the least–square fault plane (Figure 4.7), which is assumed as the causative fault for the Athens 2019 mainshock. With regards to the width parameter, the value proposed by Kouskouna et al. (2021) was selected as Kapetanidis et al. (2020) did not put forward a specific value for that parameter. However, using the empirical relation of Wells and Coppersmith (1994), a width of 4 km is projected for an Mw = 5.1 magnitude. The adopted parameters are summarized in the Table 4.7. The stress parameter value of 80 bar was chosen for the purpose of finite fault stochastic ground motion simulation based on two principal reasons. First, it was deemed necessary to adopt the same value for both Athens earthquakes, which would enable its incorporation in subsequent simulations. Additionally, the selection of this specific stress parameter value was guided by the minimal misfit between the observed and modeled PGA values.

Ref.	strike	dip	Depth of upper edge (km)	Length (km)	Width (km)	Mw	Focal depth (km)
Kapetanidis et al. (2020)	113°	55°	7	8	-	5.1	8
Kouskouna et al. (2021)	110°	52°	7.2	5	4.4	5.1	8

Table 4.6: The source parameters proposed by Kapetanidis et al. (2020) and Kouskouna et al. (2021) for the 2019 Athens earthquake.

Regarding the first calibration graph (Figure 4.8a), the implemented GMPEs estimated significantly different PGA values. Specifically, the GMPE of Bindi et al. (2014) estimated much lower PGA values compared to the one of Boore et al. (2021) for all R_{jb} distances. This deviation among the models is obviously attributed to the smaller earthquake magnitude, as in the previous earthquakes, the magnitude was equal to or greater than 6.0. This could suggest that either the GMPE of Boore et al. (2021) overestimates or the GMPE of Bindi et al. (2014) underestimates the true ground motions. However, the reality lies somewhere in the middle, as the vast majority of the observed ground motions fall between the curves of the GMPEs. Similarly, the modeled PGA values fall within the range of the curves. Although some high recorded PGA values exist in the lower R_{jb} distances, these can be attributed to the soil amplification phenomenon. Overall, the modeled PGA values are comparable to the observed ones. Regarding the second graph (Figure 4.8b), it can be observed that almost half of the ln[(Obs. PGA/Mod. PGA)] values fall within the range of [-0.5, 0.5], indicating a worse correlation between the observed and modeled PGA values compared to the Athens 1999 earthquake case. This is probably related to the significance of the amplification phenomenon. Specifically, one station, MDFB, displays a ratio reaching 1.5,

indicating a significantly larger observed PGA value. It is worth noting that MDFB is located at a Holy Monastery with soil of a highly incoherent nature, as verified by satellite imaging.

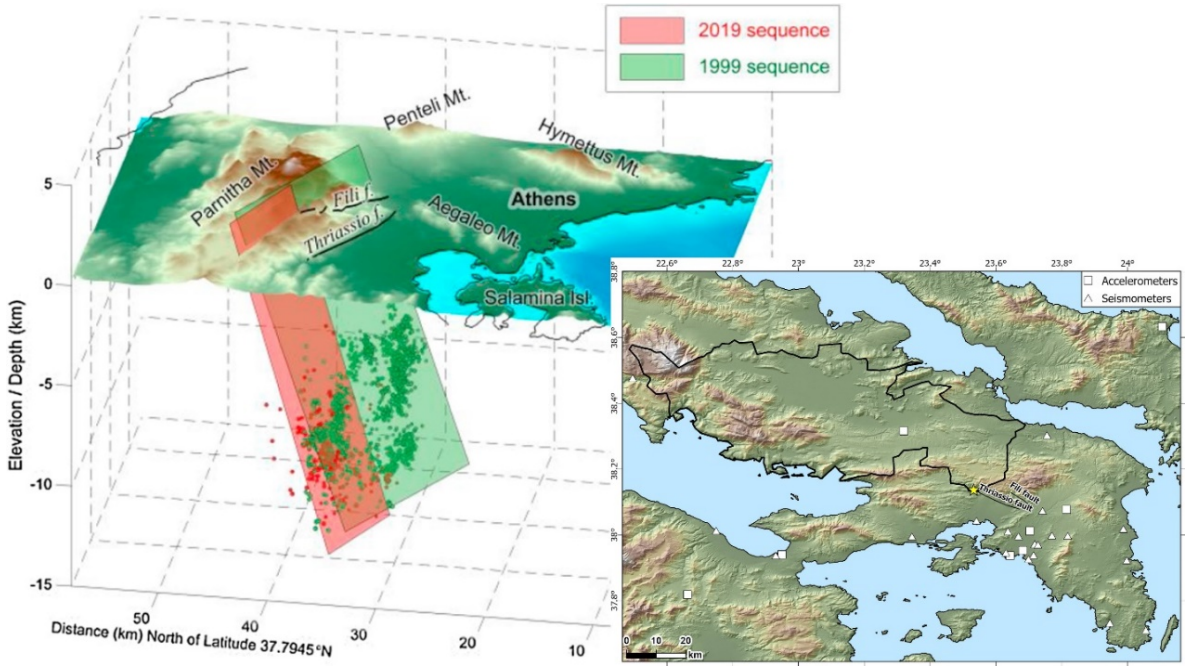

Figure 4.7: The least–square fault planes, which arise from the relocation procedure performed by Kapetanidis et al. (2020). The spatial distribution of the seismological stations is depicted in the lower right map.

Parameter	**Value**	**Reference**
Strike	113°	Kapetanidis et al. (2020)
Dip	55°	Kapetanidis et al. (2020)
Depth of the upper edge	7 km	Kouskouna et al. (2021)
Fault dimensions (Length × Width)	8 km × 4 km	Kapetanidis et al. (2020); Kouskouna et al. (2021)
Mw	5.1	Kapetanidis et al. (2020); Kouskouna et al. (2021)
Stress parameter	80 bars	This study
Kappa parameter (k_0)	0.044	Klimis et al. (1999)
Quality factor	$100f^{0.8}$	Hatzidimitriou (1993)
Geometrical spreading (R^n)	n = -1.0, R < 70 km n = 0.0, 70 km ≤ R < 130 km n = -0.5, R ≥ 130 km	Atkinson (2004)
Site amplification	Adopted from Klimis et al. (1999)	

Table 4.7: The modeling parameters utilized for the stochastic ground motion modeling of the Athens 2019 event executed with the EXSIM code.

The results indicate that the calibration process was successful for two out of the three earthquakes that shared similar path and site properties. The reasons for the partial success of the calibration process for the third earthquake can be attributed to two factors. Firstly, the magnitude of this event was significantly lower, which implies that the accuracy of the EXSIM code may be limited to strong–magnitude earthquakes. Alternatively, it is possible that the soil conditions at the stations could not be adequately characterized by the soil amplification factors or the kappa value.

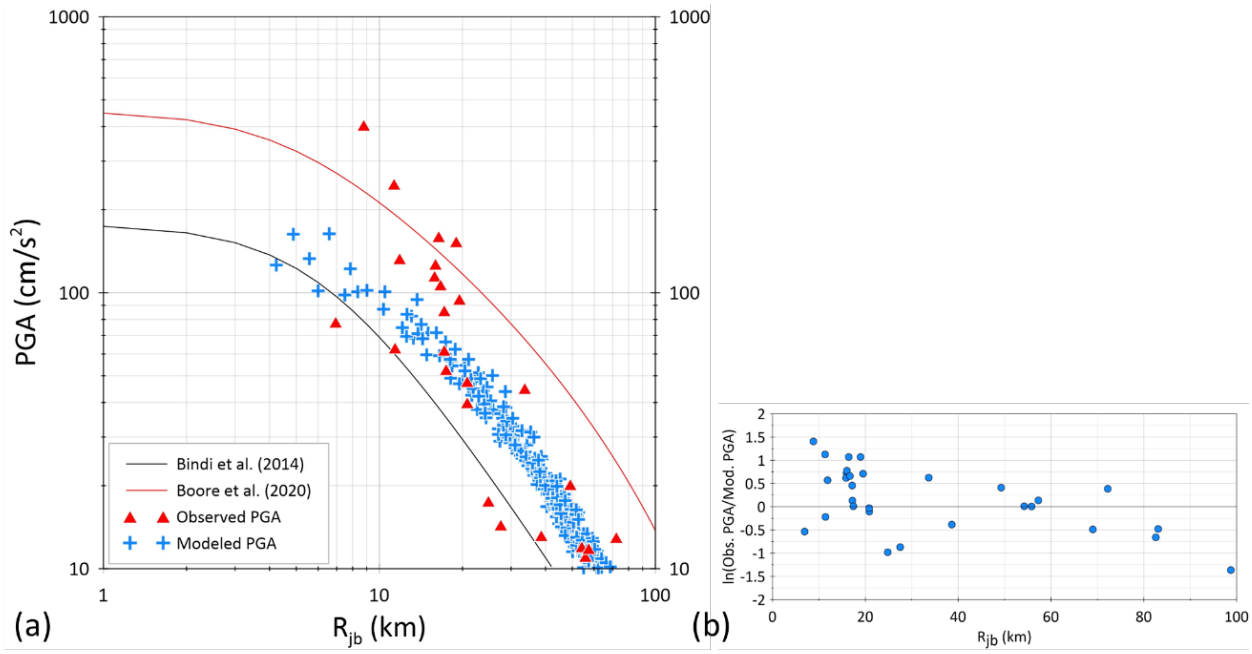

Figure 4.8: (a) the comparison of PGA values obtained from: i. recordings, represented by red triangles, ii. the GMPEs of Boore et al. (2020) and Bindi et al. (2014), indicated by lines, and iii. stochastic modeling, shown as crosses, plotted against the Joyner and Boore distance (R_{jb}). (b) Distribution of the residuals among observed and simulated PGA values against Joyner and Boore distance.

4.5 Earthquake scenarios in broader Boeotia

To adequately describe site effects, the Global V_{S30} Mosaic database was exploited (Allen and Wald, 2009; Heath et al., 2020). The subsequent step involved the selection of a grid with a resolution of 2.5 km for Boeotia. This decision was made to ensure the inclusion of as many sites as possible to avoid interpolation of the results for the region lacking data. Additionally, it aimed to present a smoother image of the distribution of PGA. The V_{S30} values were then extracted for each grid point and categorized according to the NEHRP site classification system (Table 4.1). The simulations were performed separately for each site class, employing unique site amplification factors and kappa values. Thiva and Livadia, both having a V_{S30} value of approximately 400 m/s, were classified as site class C.

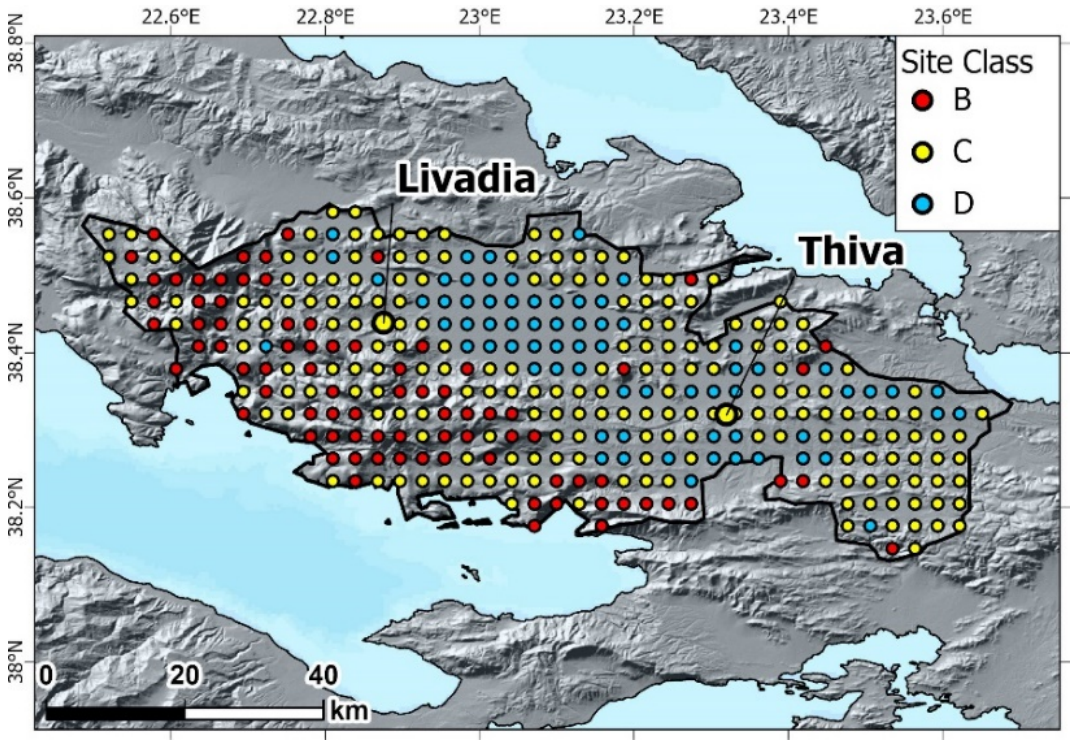

Figure 4.9: The grid that was created for Boeotia. Each grid point is classified according to the NEHRP site classification system based on its V_{S30} value that was obtained by the Global V_{S30} Mosaic database was exploited (Allen and Wald, 2009; Heath et al., 2020).

4.5.1 The 27/04/1894 M = 7.0 Atalanti earthquake

The earthquake occurred during the historical era, specifically pre–1900, before the installation of seismological stations in Greece. Conducting a finite fault stochastic ground motion simulation of this event is a valuable opportunity to investigate the PGA distribution in Boeotia and to estimate the potential accelerograms that would be recorded in the two most populated localities, i.e., Thiva and Livadia. Given that the calibration of the path and site properties has already been achieved for Boeotia, the focus will be directed solely towards determining the source parameters. The source parameters will be primarily based on macroseismic studies. Most studies concur that the rupture length of the causative fault is ~30 km, with a width of ~10 km (Skouphos, 1894; Ambraseys and Jackson, 1990; Ganas et al., 1998; Pantosti et al., 2001). The epicenter chosen for this event is 38.66°N, 23.03°E, as reported by Makropoulos and Kouskouna (1994). The depth of the upper edge has been selected to be 8 km, which is the upper limit of the average focal depths in the broader Euboekos Gulf (Makropoulos et al., 2012; Ganas et al., 2016). Additionally, the focal depth for this event has been estimated to be of the order of 10 km (Ganas et al., 2006). To summarize, the parameters for conducting the simulation are presented in Table 4.8. The stress parameter value of 80 bar remained constant for two out of three earthquakes in the calibration process.

The spatial distribution of the modeled PGA values is illustrated in Figure 4.10a. It is observed, as expected, that the highest ones are predominantly concentrated close to the causative fault. Notably, a maximum PGA value of approximately 400 cm/s^2 has been obtained. On the other hand, the lowest PGA value, equal to 50 cm/s^2, is determined at the southwestern part of the study area. It is noteworthy that comparable PGA values have been modeled for both Thiva and Livadia, with

Thiva having a slightly higher PGA value of 144 cm/s^2 compared to 131 cm/s^2 for Livadia. In addition to estimating PGA values, the PGV parameter was also modeled for the Boeotia region, as illustrated in Figure 4.10b. Consistent with the PGA values, the spatial PGV distribution indicates that the highest values are concentrated in proximity to the causative fault. Specifically, a maximum PGV value of 40 cm/s has been estimated, while the minimum value is approximately 5 cm/s. Thiva and Livadia exhibit comparable PGV values, with Thiva showing a slightly higher value of ~15 cm/s, compared to 13 cm/s for Livadia.

Parameter	**Value**	**Reference**
Strike	296°	Ganas (2022)
Dip	60°	Ganas (2022)
Depth of the upper edge	8 km	Makropoulos et al. (2012); Ganas et al. (2016)
Fault dimensions (Length × Width)	32 km × 12 km	Ganas et al. (1998); Pantosti et al. (2001)
Mw	7.0	Ambraseys and Jackson (1990); Makropoulos and Kouskouna (1994); Ganas et al. (1998)
Stress parameter	80 bars	This study
Kappa parameter (k_0)	0.035, 0.044, 0.066	Klimis et al. (1999)
Quality factor	$100f^{0.8}$	Hatzidimitriou (1993)
Geometrical spreading (R^n)	n = -1.0, R < 70 km n = 0.0, 70 km ≤ R < 130 km n = -0.5, R ≥ 130 km	Atkinson (2004)
Site amplification	Adopted from Klimis et al. (1999)	

Table 4.8: The modeling parameters utilized for the stochastic ground motion modeling of the Atalanti 1894 event executed with the EXSIM code.

In line with the PSHA framework, hazard elastic response spectra for the M = 7.0 Atalanti earthquake were created for the localities of Thiva and Livadia, with a 5% damping (Figure 4.11). The response spectra of ground motions that were modeled stochastically demonstrated a peak at short periods ranging from 0.1 to 0.3 s, followed by a steep decline. As depicted in Figure 4.11, the Atalanti fault's rupture poses a threat to the town of Thiva, whereas Livadia is exposed to a comparatively lower level of seismic hazard in the event of this earthquake. For a hypothetical rupture of the Atalanti fault, the maximum Sa values exceeded 300 cm/s^2. Additionally, the maximum anticipated Sa values approaching almost 380 cm/s^2 for Thiva. The most significant Sa value obtained in Livadia was approximately 330 cm/s^2.

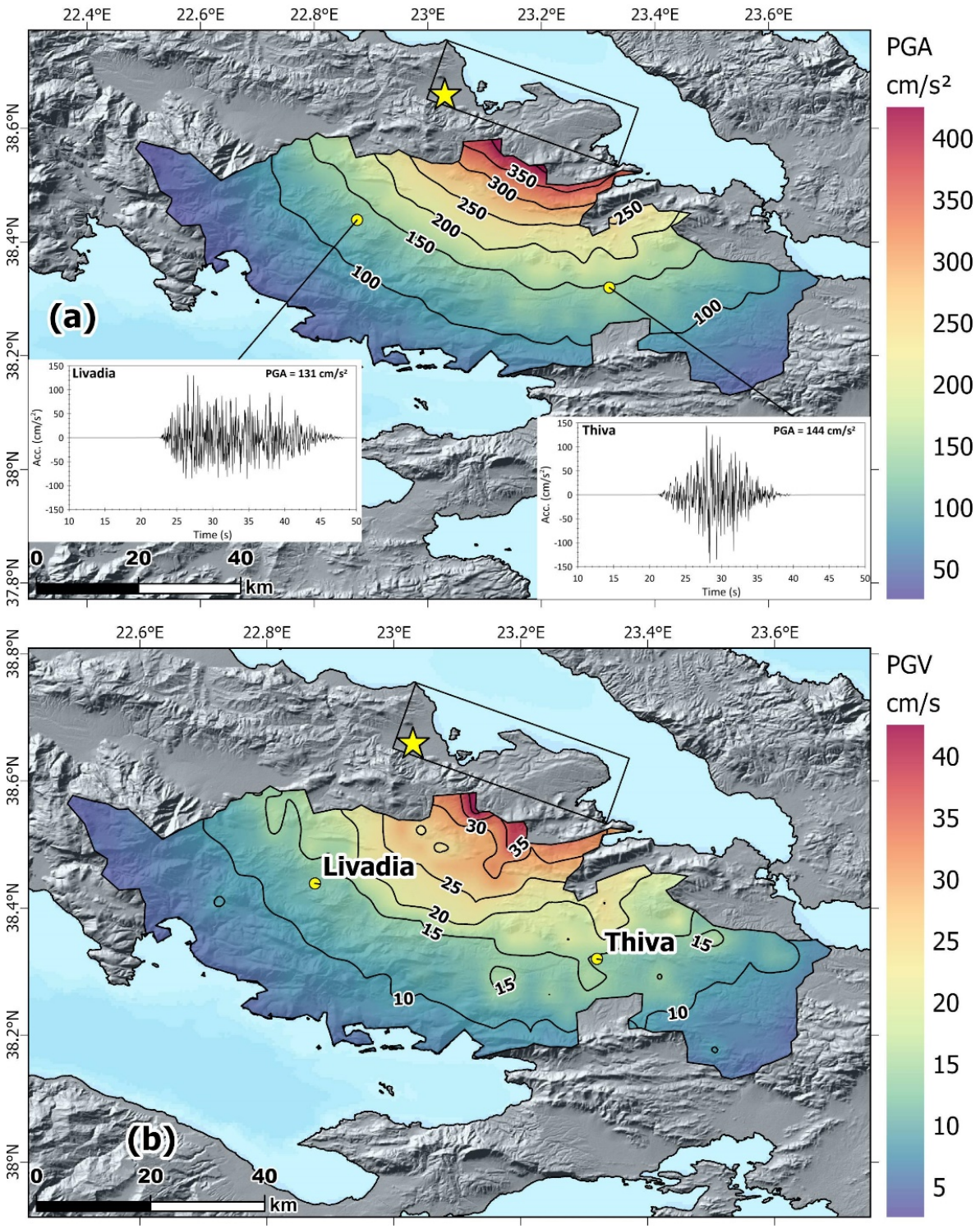

Figure 4.10: (a) Spatial distribution of PGA values alongside with the synthetic accelerograms for Thiva and Livadia and (b) spatial distribution of PGV values. The black rectangle indicates the modeled fault plane and the yellow star the selected epicenter of the 1894 M = 7.0 Atalanti earthquake.

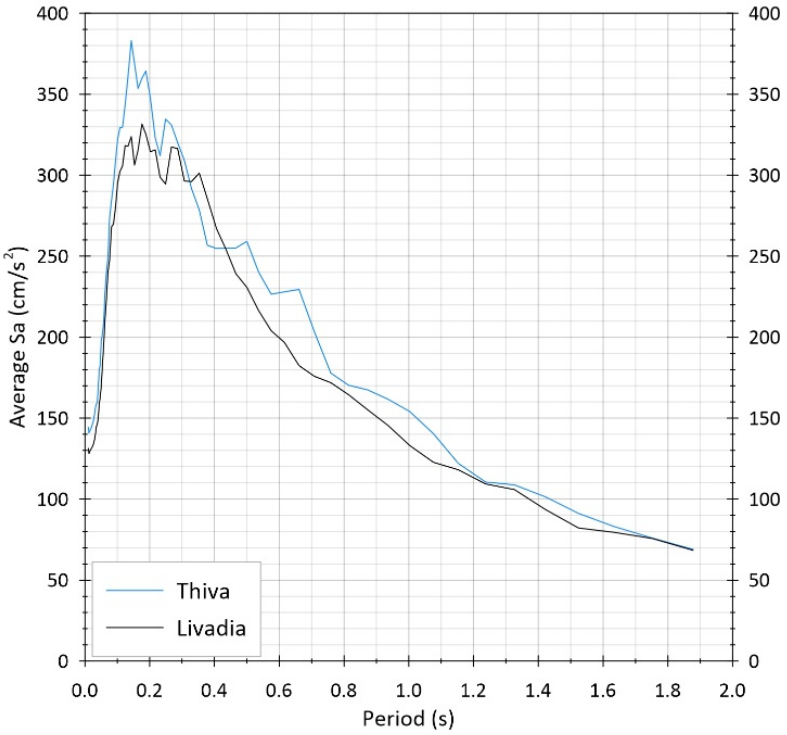

Figure 4.11: Response spectra of the 27 April 1894 M = 7.0 Atalanti earthquake scenario for Thiva and Livadia with 5% damping.

4.5.2 The 25/02/1981 Ms = 6.4 Alkyonides earthquake

On 25/02/1981, the second major aftershock of the Alkyonides earthquake sequence occurred with a magnitude of Ms = 6.4. The mainshock of this sequence (24/02/1981) was of magnitude M = 6.7, making this particular event a suitable candidate for finite fault stochastic modeling. However, the causative fault of this event has not been identified. On the other hand, the Pisia Fault was identified as the seismogenic fault of the 25/02/1981 Mw = 6.4 event, according to the work of Papazachos et al. (1984) and Hubert et al. (1996).

The seismotectonic study of the Alkionides earthquake sequence was initially conducted by Jackson et al. (1982). Subsequent work by Papazachos et al. (1984) utilized a different relocation method (absolute versus relative). Nevertheless, the fault plane solutions, proposed by both studies, for the 25/02/1981 event share similar strike and dip values. The depth of the upper edge was estimated from information regarding the hypocentral distribution in the Eastern Gulf of Corinth (Mesimeri et al., 2018; Michas et al., 2022). The length of the causative fault (Table 4.9) was adopted by the NOAFaults database, whereas for the width the empirical relations of Wells and Coppersmith (1994) and Thingbaijam et al. (2017) were taken into account and the mean value was used.

The spatial distribution of PGA and PGV values resulting from the seismic event under investigation is presented in Figure 4.12a and b, respectively. Similar with the Atalanti event scenario, the highest values of both PGA and PGV are observed in close proximity to the fault plane, while the lowest ones are situated in northern Boeotia. The maximum PGA value 220 cm/s^2 (Figure 4.12a) is located in southern Boeotia, whereas the lowest PGA value (~20 cm/s^2) is situated in the northern portion of the study area.

The PGV map (Figure 4.12b) displays the highest value of 18 cm/s and the lowest one of 2 cm/s, both at the same locations as the PGA values. However, it should be noted that the PGA and PGV values are considered intermediate to low. This can be attributed to the fact that the seismogenic layer is deeper than that of the Western Gulf of Corinth (Kaviris, 2003; Kaviris et al., 2021; Michas et al., 2022). This results in a stronger decay of the seismic wave's amplitude, given that it is inversely proportional to the distance, reducing the ground movement in Boeotia.

Parameter	**Value**	**Reference**
Strike	248°	Jackson et al. (1982)
Dip	42°	Jackson et al. (1982)
Depth of the upper edge	4 km	Michas et al. (2022)
Fault dimensions (Length × Width)	18 km × 15 km	Wells and Coppersmith (1994); Thingbaijam et al. (2017); Ganas (2022)
Mw	6.4	Jackson et al. (1982); Papazachos et al. (1984)
Stress parameter	80 bars	This study
Kappa parameter (k_0)	0.035, 0.044, 0.066	Klimis et al. (1999)
Quality factor	$100f^{0.8}$	Hatzidimitriou (1993)
Geometrical spreading (R^n)	n = -1.0, R < 70 km n = 0.0, 70 km ≤ R < 130 km n = -0.5, R ≥ 130 km	Atkinson (2004)
Site amplification	Adopted from Klimis et al. (1999)	

Table 4.9: The modeling parameters utilized for the stochastic ground motion modeling of the Alkyonides 1981 event executed with the EXSIM code.

Hazard elastic response spectra for the 25/02/1981 M= 6.4 event were created for Thiva and Livadia, with a 5% damping (Figure 4.13). The response spectra demonstrated a peak at low periods ranging from 0.1 to 0.3 s, followed by a steep decline (after 0.35 s), similar to the case of the Atalanti simulation. The Pisia fault's rupture poses the same threat to the towns of Thiva and Livadia, because the shape and the values from the two spectra are similar, with the exception that Livadia has higher spectral acceleration values for the range of periods [0.1, 0.2] s. For a hypothetical rupture of the Pisia fault, according to the applied scenario. The maximum Sa values are ~160 cm/s^2 for Livadia and ~150 cm/s^2 for Thiva.

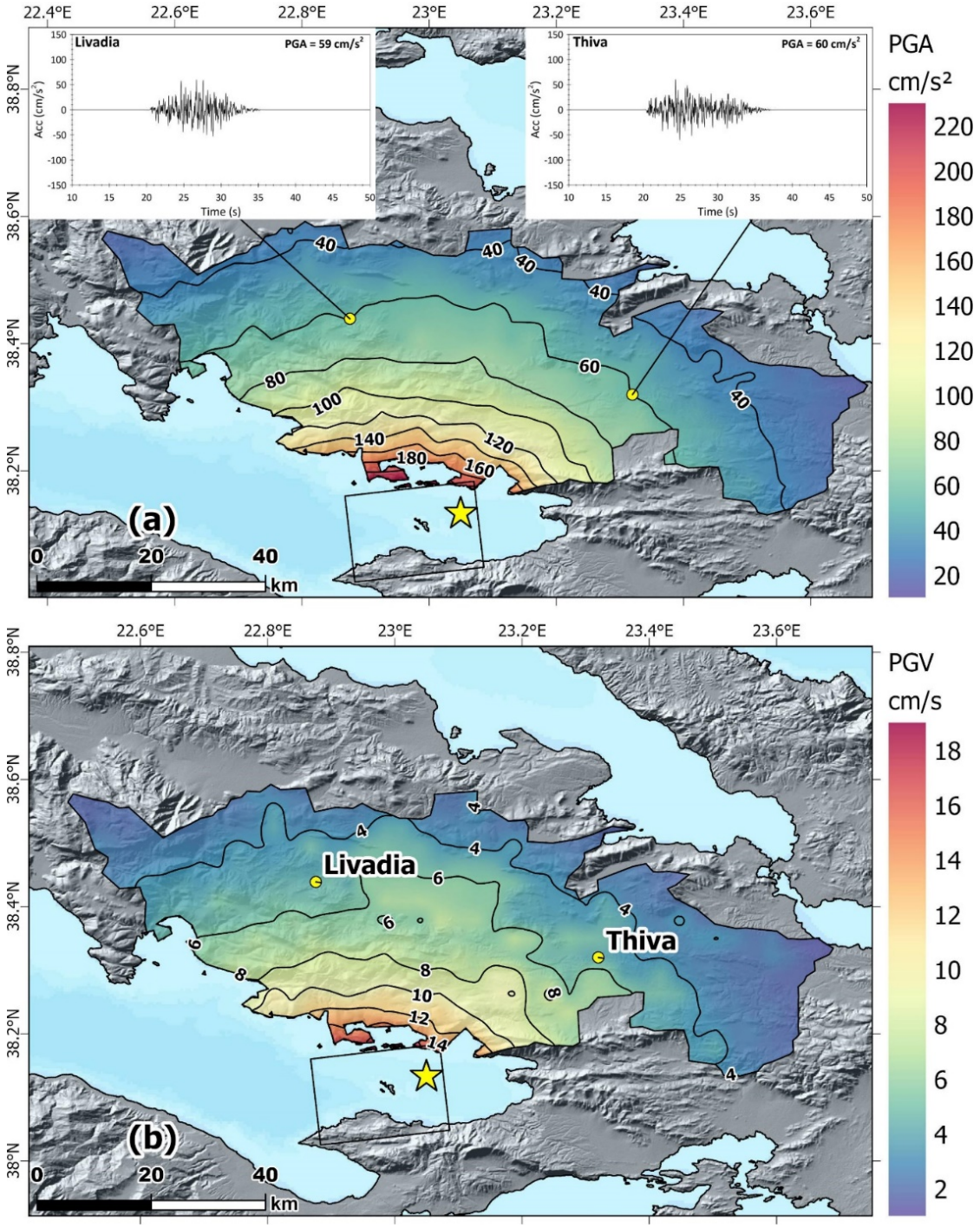

Figure 4.12: (a) Spatial distribution of PGA values alongside with the synthetic accelerograms for Thiva and Livadia and (b) spatial distribution of PGV values. The black rectangle indicates the modeled fault plane and the yellow star the selected epicenter of the 1981 M = 6.4 Alkyonides earthquake.

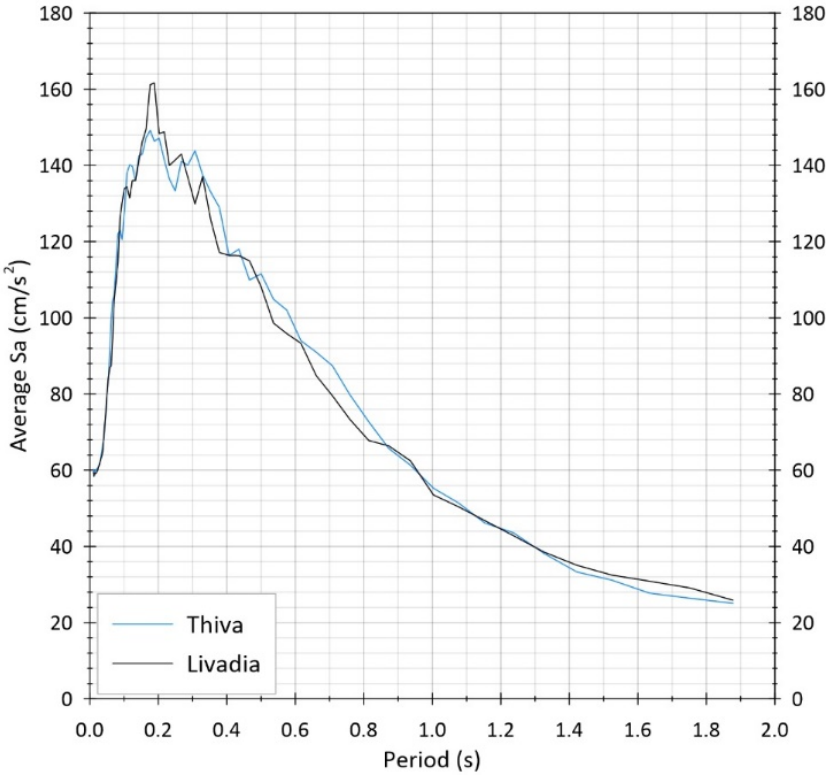

Figure 4.13: Response spectra of the 25 February 1981 M = 6.4 Alkyonides earthquake scenario for Thiva and Livadia with 5% damping.

4.5.3 The Kallithea–Mavrovouni earthquake simulation–(Mw = 6.3)

The commencement of the initial stage of the 2020-2021 Thiva sequence was attributed to the Mw = 4.2 mainshock, which occurred on 02/12/2020. As described in the works of Elias et al. (2021) and Kaviris et al. (2022a), the Kallithea fault was the causative fault that ruptured during the occurrence of this event. The Kallithea fault, as stated in these works, is one of the two segments of a zone, the other being the Mavrovouni fault (Figure 1.8). It is also documented that if both segments rupture as one, a strong earthquake with a magnitude of $6.2 \leq M \leq 6.4$ could occur. The 1914 M = 6.0 Thiva earthquake may have ruptured both faults as the epicenter's location is considered to be in close proximity to these two segments (Kaviris et al., 2022a).

In this thesis, the applied earthquake scenario considers an event of magnitude Mw = 6.3, rupturing the entire length of both the Kallithea and Mavrovouni faults. In this way, the PGA and PGV distributions and the theoretical elastic response spectra for Thiva and Livadia of this strong in terms of magnitude earthquake scenario are investigated. Most source parameters were obtained from the studies of Elias et al. (2021) and Kaviris et al. (2022a), with the exception of the length and width of the zone, which were estimated for an Mw = 6.3 scenario earthquake, using the mean values of the ones resulting from the empirical relations proposed by Wells and Coppersmith (1994) and Thingbaijam et al. (2017). The burial depth of the upper edge was estimated based on the seismic cross–sections provided by Kaviris et al. (2022a). All the parameters are presented in the Table 4.10.

Parameter	Value	Reference
Strike	106°	Elias et al. (2021); Kaviris et al. (2022a)
Dip	31°	Elias et al. (2021); Kaviris et al. (2022a)
Depth of the upper edge	1 km	Kaviris et al. (2022a)
Fault dimensions (Length × Width)	18 km × 14 km	Wells and Coppersmith (1994); Thingbaijam et al. (2017);
Mw	6.3	Kaviris et al. (2022a)
Stress parameter	80 bars	This study
Kappa parameter (k_0)	0.035, 0.044, 0.066	Klimis et al. (1999)
Quality factor	$100f^{0.8}$	Hatzidimitriou (1993)
Geometrical spreading (R^n)	n = -1.0, R < 70 km n = 0.0, 70 km ≤ R < 130 km n = -0.5, R ≥ 130 km	Atkinson (2004)
Site amplification	Adopted from Klimis et al. (1999)	

Table 4.10: The modeling parameters utilized for the stochastic ground motion modeling of a Mw=6.3 earthquake scenario, rupturing the Kallithea and Mavrovouni faults, executed with the EXSIM code.

The spatial distribution of PGA and PGV is illustrated in Figure 4.14a and b. The highest PGA and PGV values are observed in close proximity to the ruptured events, whereas the lowest values are concentrated in the western part of Boeotia. Regarding the modeled PGA values, as depicted in Figure 4.14a, there is a considerable variation in values within approximately 20 km of the rupture plane, ranging from 300 cm/s^2 to 1000 cm/s^2. The observed attenuation is strong, with the PGA approaching values close to zero in the westernmost part of Boeotia.An accelerograph station in Thiva and Livadia would record PGA values of 549 cm/s^2 and 45 cm/s^2, respectively, indicating the aforementioned strong attenuation. In terms of PGV, as depicted in Figure 4.14b, the highest value is 70 cm/s and the lowest value is nearly zero. Similarly, there is significant variation in PGV values near the rupture plane.

Hazard elastic response spectra for the M = 6.3 Kallithea–Mavrovouni scenario earthquake were created for Thiva and Livadia, with a 5% damping (Figure 4.15). The response spectra demonstrated a peak at short periods ranging from 0.1 to 0.3 s. As depicted in Figure 4.11, the rupture of the whole zone of Kallithea and Mavrovouni faults poses a significant threat to the town of Thiva, whereas Livadia is exposed to a significant lower level of seismic hazard. The maximum Sa value exceeded 1000 cm/s^2 for Thiva, whereas for Livadia is ~100 cm/s^2.

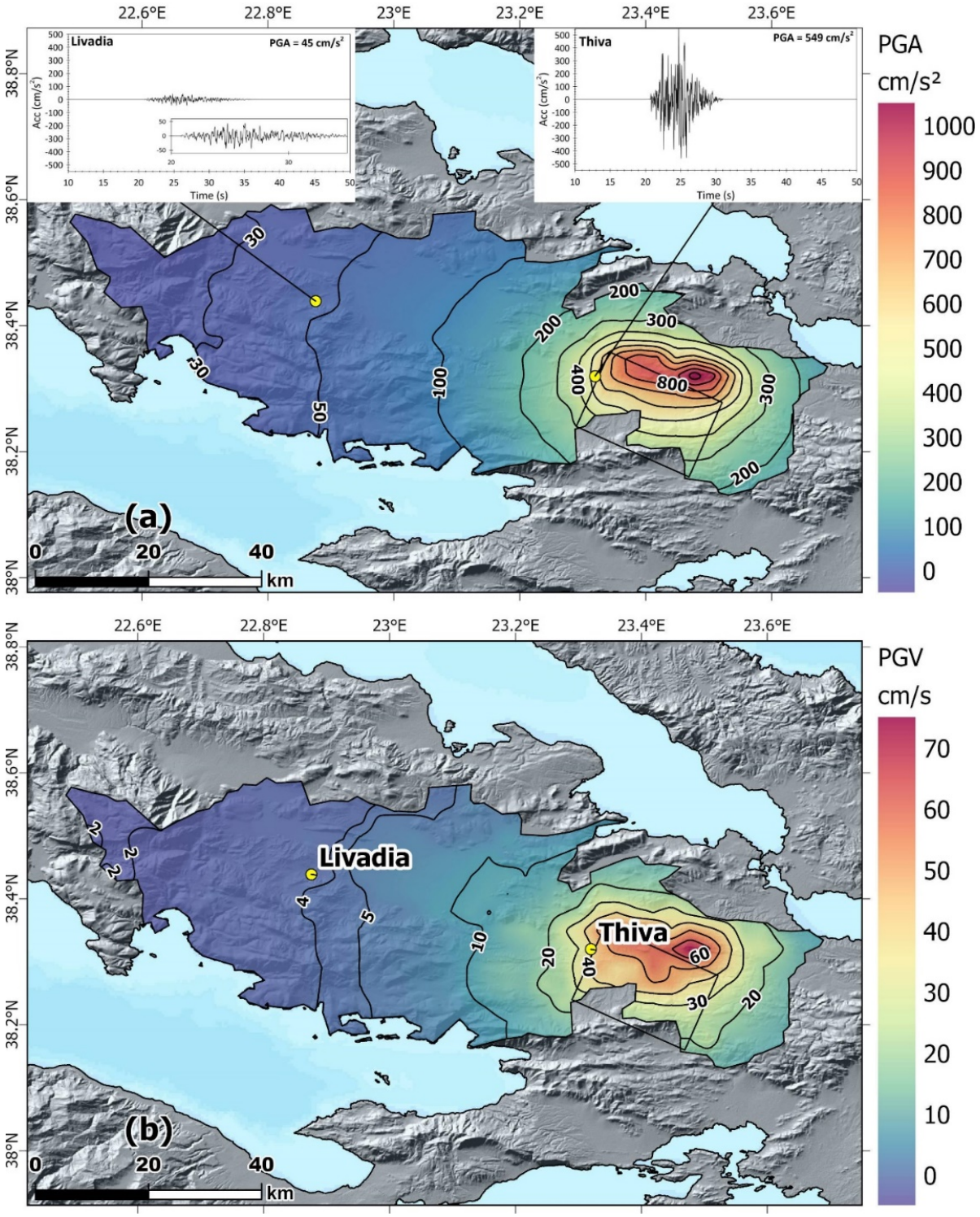

Figure 4.14: (a) Spatial distribution of PGA values alongside with the synthetic accelerographs for Thiva and Livadia and (b) spatial distribution of PGV values. The black rectangle indicates the modeled fault plane of the Kallithea–Mavrovouni scenario earthquake. The earthquake magnitude is Mw = 6.3.

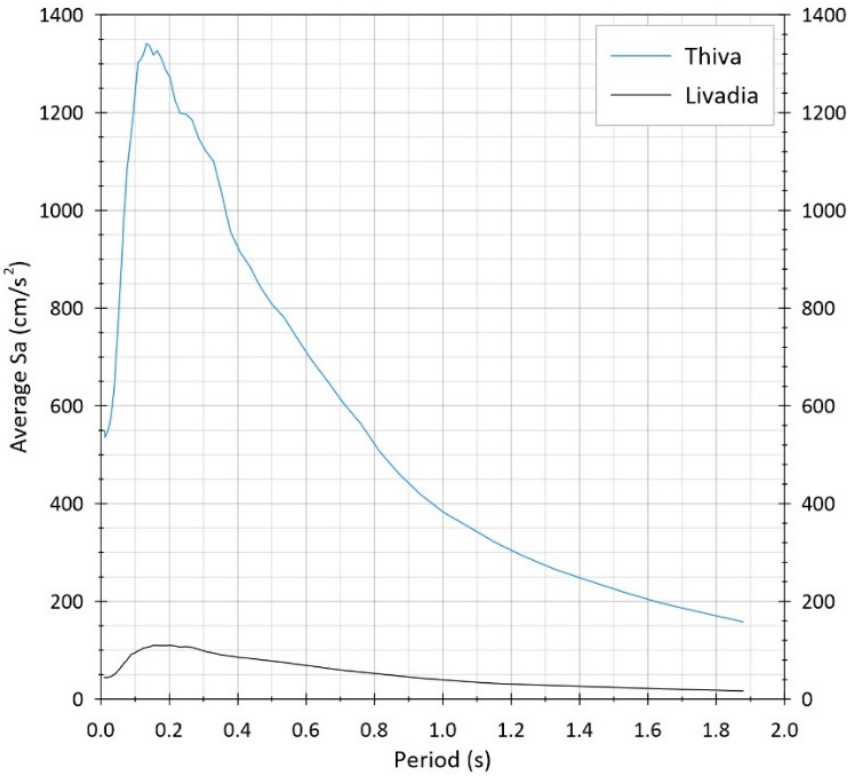

Figure 4.15: Response spectra of the Kallithea–Mavrovouni scenario for Thiva and Livadia with 5% damping. The earthquake magnitude is Mw = 6.3.

4.5.4 The Kallithea–Mavrovouni earthquake simulation–(Mw = 6.0)

As previously stated, the earthquake that occurred in Thiva in 1914 with a magnitude of M = 6.0 may have ruptured both Kallithea and Mavrovouni as a zone, as reported by Kaviris et al. (2022a). An earthquake scenario of higher magnitude was previously simulated which did not replicate the Thiva 1914 event. In order to estimate ground motions for an earthquake scenario that is similar to the Thiva 1914 event, the dimensions of the fault plane were adjusted for an earthquake of magnitude Mw = 6.0 (Table 4.10). Therefore, the herein considered fault length is 11 km and the width 10 km. The other parameters were adopted from Table 4.10. The spatial distribution of both PGA and PGV values is similar to the previous earthquake simulation, but the values are smaller (Figure 4.16a and b). The highest PGA value in the current simulation is approximately 900 cm/s^2 instead of 1000 cm/s^2, and the PGA value for Thiva is 234 cm/s^2 instead of the of 549 cm/s^2 for the previous scenario (Figure 4.16a). The PGA value for Livadia is 31 cm/s^2, compared to 45 cm/s^2 (Figure 4.16a). The highest PGV value is ~70 cm/s and the one in Thiva is ~20 cm/s, whereas for Livadia is only ~3 cm/s (Figure 4.16b). Regarding the hazard elastic response spectra for Thiva and Livadia (Figure 4.17), the difference between the two locations is significant, as the greatest Sa value computed for Thiva is approximately 580 cm/s^2, while for Livadia, it is 80 cm/s^2, indicating significant attenuation for all frequencies.

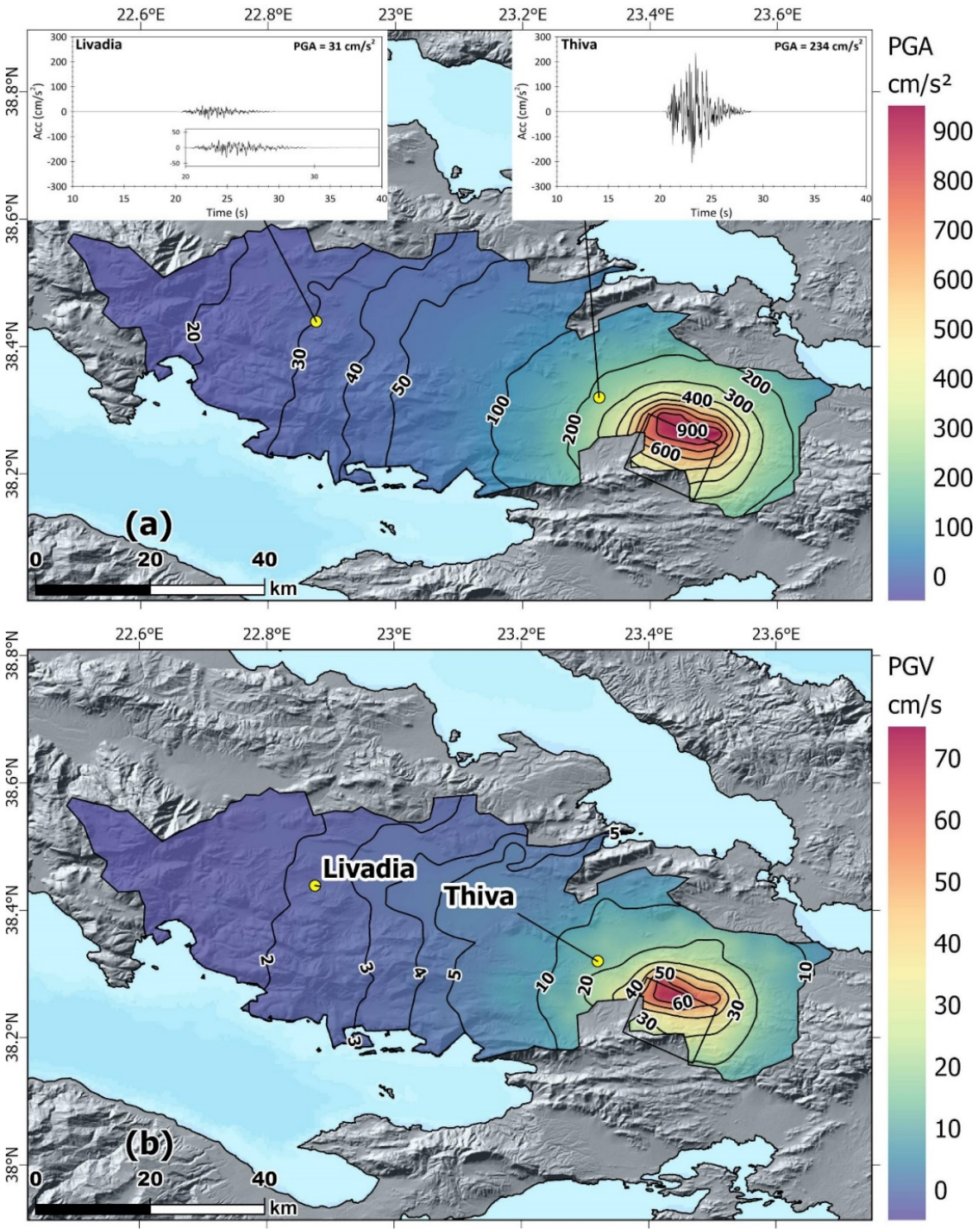

Figure 4.16: (a) Spatial distribution of PGA values alongside with the synthetic accelerographs for Thiva and Livadia and (b) spatial distribution of PGV values. The black rectangle indicates the modeled fault plane of the Kallithea-Mavrovouni. This earthquake simulation has the same parameters as those represented in the Table 4.10 except from the fault dimensions (11 km × 10 km) and the earthquake magnitude, which is Mw = 6.0.

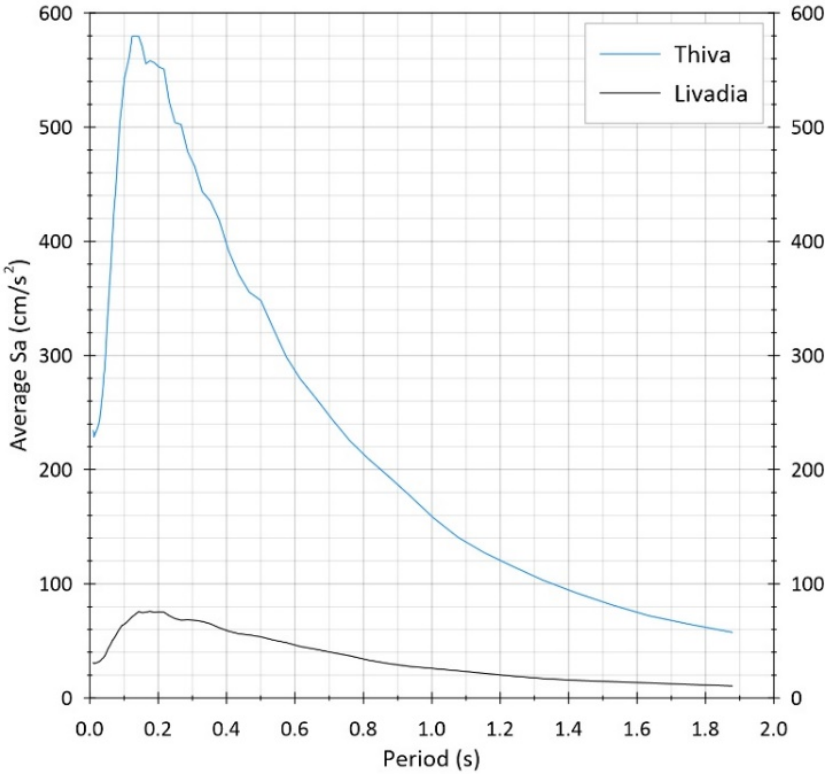

Figure 4.17: Response spectra of the Kallithea-Mavrovouni scenario for Thiva and Livadia with 5% damping. This earthquake simulation has the same parameters as those represented in the Table 4.10 except from the fault dimensions (11 km × 10 km) and the earthquake magnitude, which is Mw = 6.0.

5 Discussion

Boeotia is a region characterized by moderate seismic activity. However, in the past, several significant earthquakes have occurred within or close to the area. These include the Atalanti event of April 27th, 1894, which had a magnitude of M = 7.0, the Thiva event of 1914 with a magnitude of M = 6.0, and the Alkyonides earthquakes of February 24th and 25th and March 4th, with magnitudes of 6.7, 6.4, and 6.4, respectively. Recently, during 2020–2022 an intense earthquake sequence occurred close to Thiva, with the largest (however, moderate) event occurring near the village of Kallithea, with a magnitude of Mw = 4.6. Although this event did not cause any damage, it resulted in ground deformation due to its very shallow focal depth. This study assesses the seismic hazard of Boeotia by incorporating new data, aiming to achieve a reliable model with reduced epistemic uncertainties. Probabilistic and scenario–based finite fault stochastic modeling is used to quantify the maximum expected ground motions in the Boeotia region.

In order to address the research question at hand, seismic hazard must be evaluated using different approaches in order to account for the epistemic uncertainties that are inherent to such studies. To this end, maximum expected ground motions were quantified by estimating the Peak Ground Acceleration (PGA), Peak Ground Velocity (PGV), and Spectral acceleration (Sa), the latter for a range of periods and only for the two most populated localities, i.e., Thiva and Livadia. The first approach involved Probabilistic Seismic Hazard Assessment (PSHA), which was conducted using two software packages in order to compare and evaluate their performance. The software packages utilized were the latest version of CRISIS, now known as R–CRISIS, and the OpenQuake engine (OQ–engine). The PGA values computed using R–CRISIS (Figure 5.1a and c) are smaller throughout the region of Boeotia, in comparison to the ones obtained from the OQ–engine (Figure 5.1b and d). Specifically, for a return period of 475 years, the highest PGA value computed via R–CRISIS reaches approximately 300 cm/s², whereas in the OQ–engine, it approaches 400 cm/s². Furthermore, a difference is observed in the PGA spatial distribution. In the case of R–CRISIS, the highest PGA values are concentrated in the southern region, while the lowest values are predominantly found in the northern part of Boeotia. On the other hand, the OQ–engine yields the highest PGA values in the southeastern part of the map. For a return period of 950 years, the spatial distribution of the PGA values is the same as for the previous RP. With respect to the results obtained by R–CRISIS, the maximum PGA value is approximately 380 cm/s^2, while the lowest is around 200 cm/s^2. However, in the case of the OQ–engine software, the highest PGA value is approximately 480 cm/s^2, while the lowest is 260 cm/s^2.

The PGV results obtained by the OQ–engine (Figure 5.2b and d) are also higher in comparison to R–CRISIS (Figure 5.2a and c). The deviation between the highest PGV values is approximately 4 cm/s for a return period of 475 years and 8 cm/s for 950 years (Figure 5.2c and d). The spatial distribution of the PGV values for both software packages is almost identical with the one of PGA, yet different for R–CRISIS and the OQ–engine.

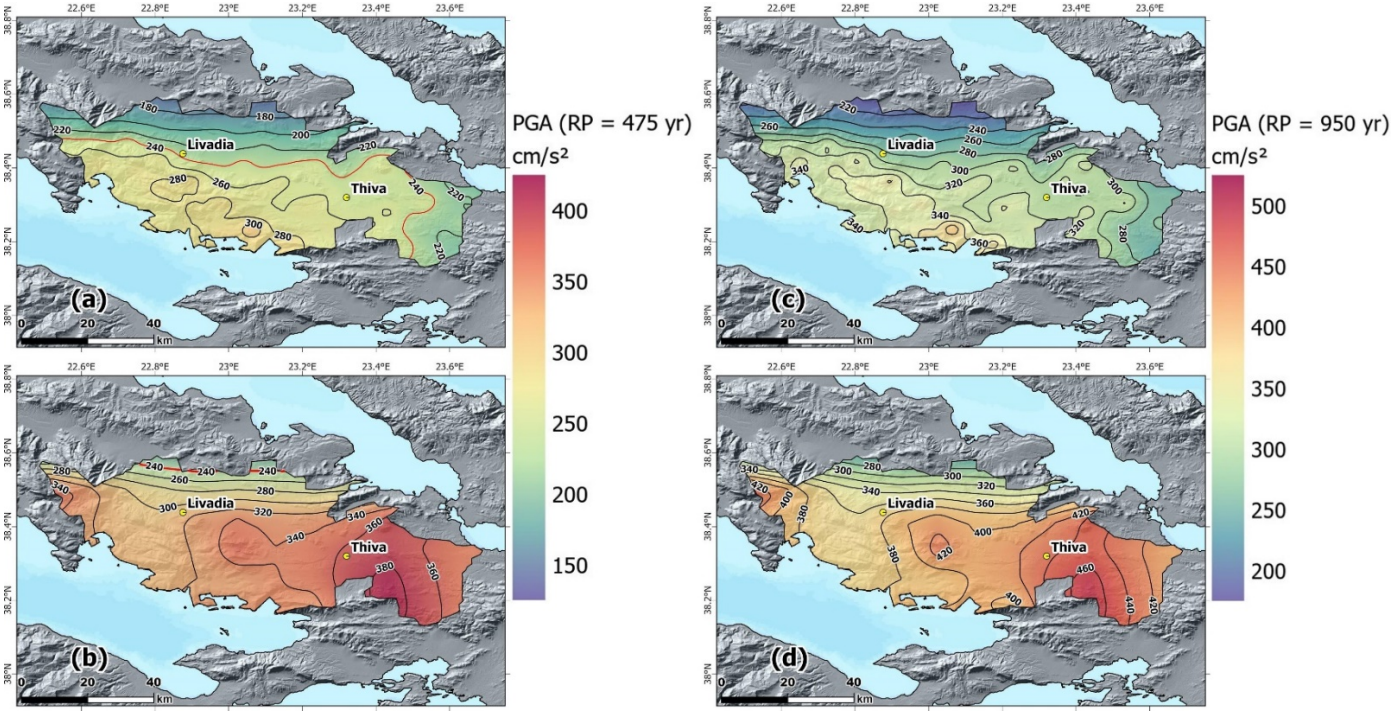

Figure 5.1: A comparison of the PGA results for a return period of 475 years (a, b) and 950 years (c, d) obtained from the software package of R–CRISIS (a, c) and OpenQuake–engine (b, d).

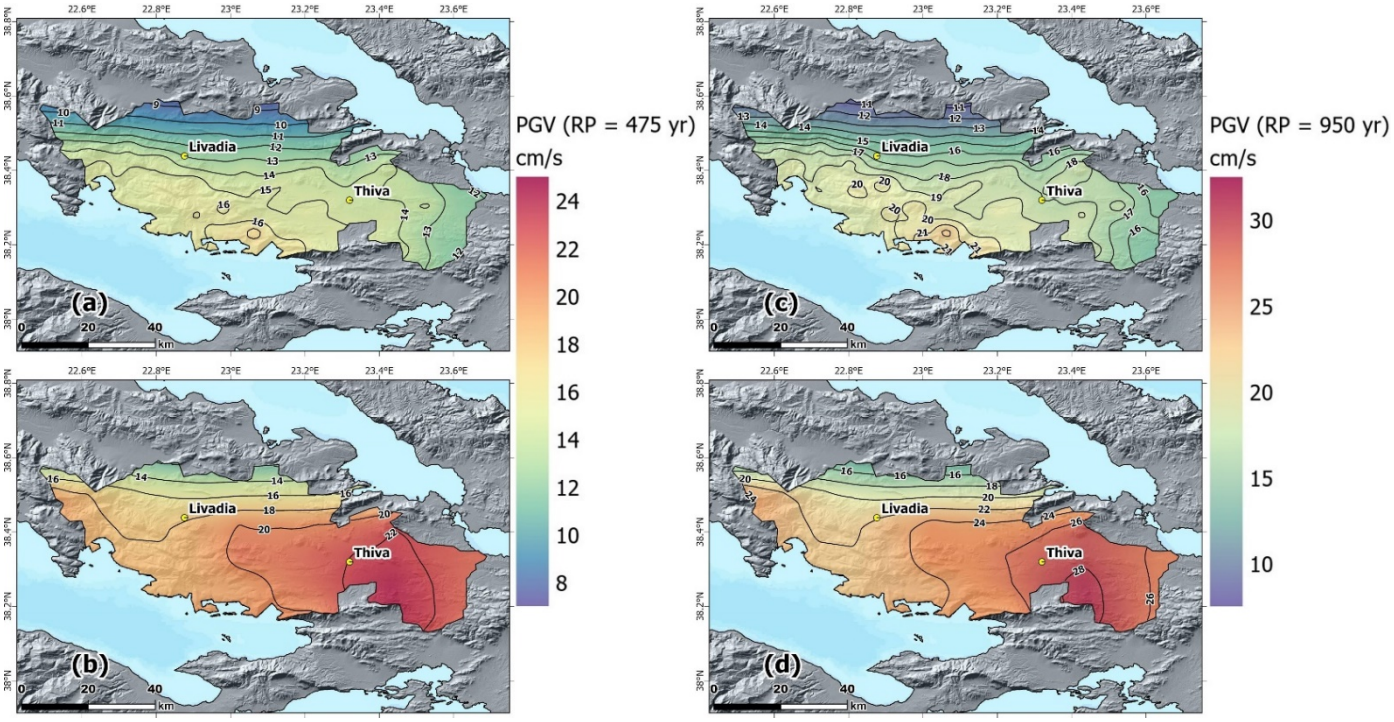

Figure 5.2: A comparison of the PGV results for a return period of 475 years (a, b) and 950 years (c, d) obtained from the software package of R–CRISIS (a, c) and OpenQuake–engine (b, d).

Apart from the differences in spatial distribution, significant differences were also observed in the PGA–hazard curves (Figure 5.3a) and the Uniform Hazard Spectra (UHS) (Figure 5.3b). The OQ–engine again computed higher PGA values for both Thiva and Livadia compared to R–CRISIS, as shown in the PGA–hazard curves. In addition, the Livadia curve, constructed using PGA values computed via the OQ–engine, was higher than the Thiva curve, which was constructed using PGA values computed via R–CRISIS. This suggests that the OQ–engine computes significantly higher PGA values for all sites, even for those with lower levels of seismic hazard, and likely all surpass the values obtained using R–CRISIS. However, based on the PSHA, it is evident that the occurrence of extreme ground motions of the order of 1 g is unlikely. Similar observations were made for the UHS (Figure 5.4b), where differences were also observed between the two software packages. Both software indicate a fundamental period of 0.25 s, as the same GMPE was utilized. The highest Sa value was 550 cm/s^2 for the site of Thiva, computed using the OQ–engine.

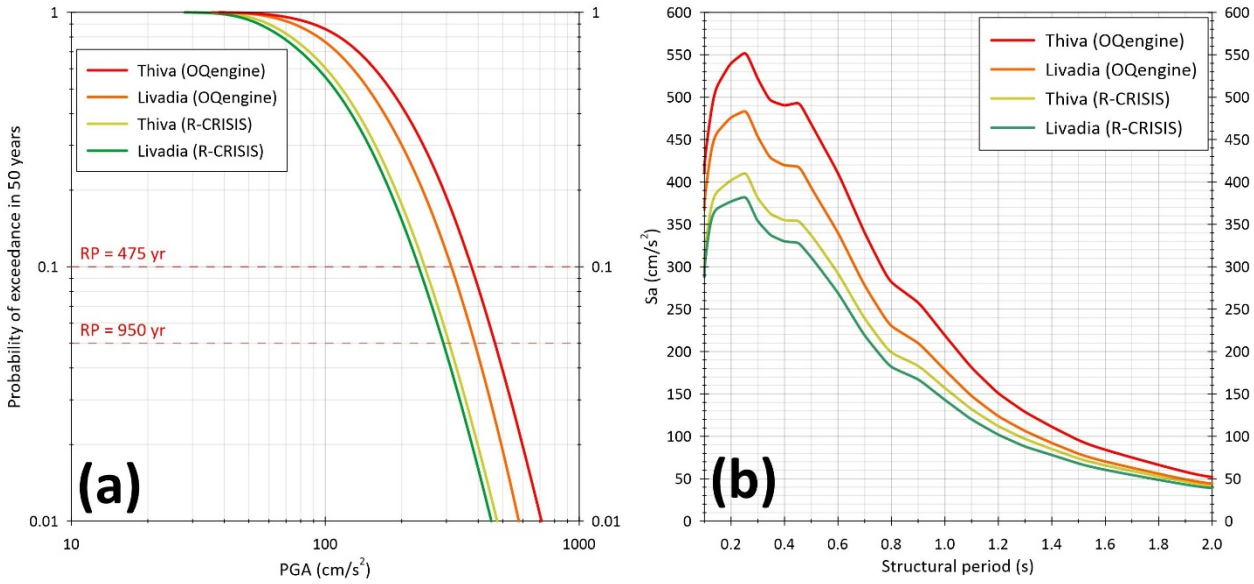

Figure 5.3: A comparison of the (a) PGA-hazard curves and (b) the Uniform Hazard Spectra constructed for the localities of Thiva and Livadia using the software package of R-CRISIS and OpenQuake-engine.

Although the mathematical background of both software packages is the same, i.e., both estimate the annual probability of exceedance for a given PGA value via the "hazard integral", the OQ–engine offers the addition of Monte Carlo (MC) sampling to the computational process. The “hazard integral” is a double integral of a function of two independent variables, i.e., distance and magnitude (equation 2.12). Given that the magnitude and distance bins are infinite, some samples of these two variables are randomly selected in order to compute the IMT annual probability of exceedance. Multiple samples are collected and used to approximate the desired quantity and, as the number of random trials performed increases, the approximated quantity becomes more accurate (Goodfellow et al., 2016). To investigate how different sampling rates affect the distribution of PGA, PGV, and Sa values, an arbitrary illustration was created for four different sample sizes, as shown in Figure 5.4. In the OQ–engine, it is feasible to specify the number of samples for the MC sampling. However, in the R–CRISIS software, there is no provision for adjusting the computation resolution, rendering the software akin to a black box, which makes the results obtained by OQ–engine preferable. Thus, the herein obtained results, regarding both the

PGA and PGV values and their spatial distribution, are considered more accurate in the OQ–engine.

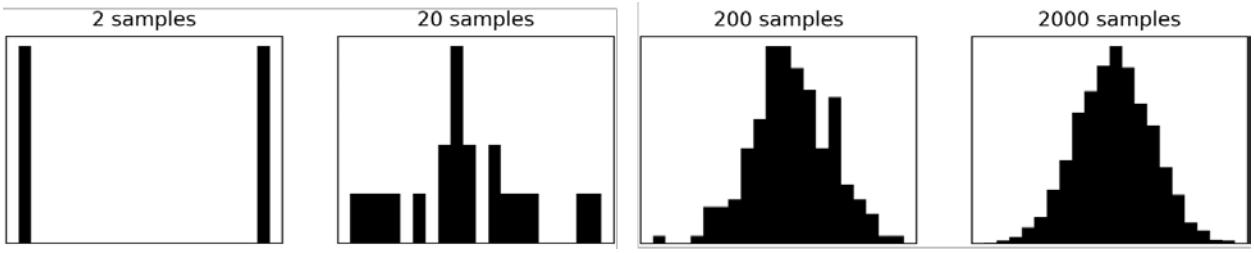

Figure 5.4: The example of Monte Carlo sampling. An arbitrary distribution of data and how it is affected by the different number of random samples.

In Greece, the National Building Code divides the country into three zones, each with a reference value of PGA for a return period of 475 years (referring to rock conditions). The low, medium, and high seismic hazard zones correspond to PGA values of 0.16 g (~160 cm/s^2), 0.24 g (~240 cm/s^2), and 0.36 g (~360 cm/s^2), respectively. Boeotia falls entirely within the moderate zone. The OQ results (RP = 475 years) indicate that almost the entire Boeotia, except for its northernmost part, exceeds the reference value of 240 cm/s^2 (red contour in Figures 5.1 a and b). However, it must be noted that the reference values provided by EAK (2003) are the so-called "effective" peak accelerations, which are the maximum ground accelerations to which a building responds, and are bound to be lower from the PGA values in most case studies (Algermissen and Perkins, 1976).

The second approach employed for evaluating seismic hazard in Boeotia involved a scenario–based finite fault stochastic ground motion modeling technique. This approach utilized earthquake scenarios to generate PGA, PGV, and Sa values for various sites, which were considered as phantom stations. To prevent the need for value computation through an interpolation process, the grid of stations was expanded to include Thiva and Livadia. The choice of this approach was motivated by the desire to investigate individual fault ruptures and the associated ground motion resulting. In contrast to the PSHA method that considers the entire earthquake catalog, the finite fault stochastic ground motion modeling technique enables the study of a single earthquake occurrence. Furthermore, the PSHA that was conducted in this thesis relies on area source zones that are constrained to describe similar spatial seismotectonic characteristics and do not incorporate faults, unlike the aforementioned method.

In this thesis, three fault ruptures were simulated to estimate the ground motions that would occur in Boeotia. The first fault rupture simulated was that of the Atalanti fault, which was responsible for the historical earthquake of the 27/04/1894, with a magnitude of M = 7.0. The second fault rupture considered was that of the Pisia fault, which was responsible for the event of the 25/02/1981, in the Alkyonides gulf, with a magnitude of M = 6.4. The third and final fault rupture simulated was that of the Kallithea and Mavrovouni zone, which consists of two segments that were possibly activated during the 1914 Thiva event, with a magnitude of M = 6.0. However, two different earthquake scenarios were considered for this rupture. The first scenario involved an earthquake with a magnitude of Mw = 6.3, which is the worst credible scenario, while the second one considered an earthquake with a magnitude of Mw = 6.0, which simulated the 1914 earthquake event.

Regarding the 1894 M = 7.0 Atalanti earthquake scenario, PGA values greater than 240 cm/s^2 were identified in the northern part of Boeotia, at a distance of approximately 20 km from the Atalanti

fault. In contrast, the 1981 Mw = 6.4 event that ruptured the Pisia fault did not exhibit any modeled PGA values exceeding 240 cm/s^2, the design value proposed by EAK (2003). This result is attributed to the significantly lower magnitude of this scenario, compared to Atalanti. For the third scenario earthquake considered, which is supposed to rupture the two segments of Kallithea and Mavrovouni faults and had a magnitude of Mw = 6.3, very high PGA values were simulated, reaching up to 1000 cm/s^2 near the fault plane and approximately 550 cm/s^2 in Thiva. However, the PGA values were significantly reduced at greater distances from the fault plane, with a value of 45 cm/s^2 in Livadia. For these localities, there was a significant reduction in PGA values when the same simulation was performed with a lower earthquake magnitude of Mw = 6.0, corresponding to the 1914 Thiva earthquake. In addition to the PGA values, elastic response spectra were constructed for Thiva and Livadia (Figure 5.5) for all scenarios. These spectra clearly indicate the fault ruptures that pose the greatest hazard in terms of producing ground motions for each locality. Specifically, Thiva is highly exposed to the scenario which involves the rupture of the entire Kallithea and Mavrovouni fault zone. Conversely, Livadia is primarily exposed to the rupture of the Atalanti fault, however with much smaller Sa values compared to Thiva.

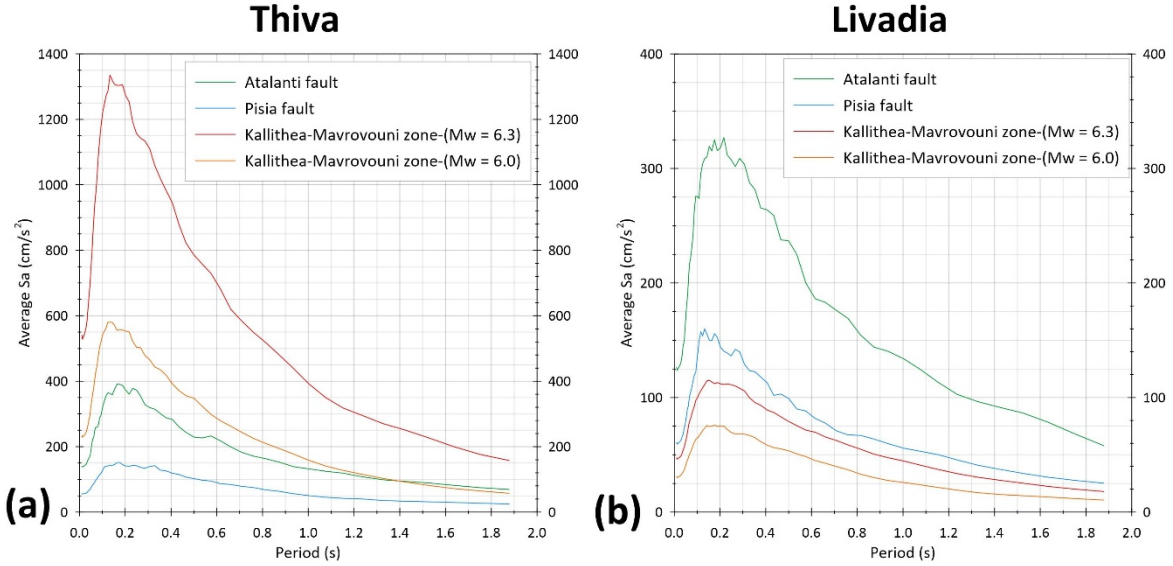

Figure 5.5: Response elastic spectra of the selected earthquake scenarios for (a) Thiva and (b) Livadia corresponding to 5% damping.

There has been a lack of seismic hazard assessments for the Boeotia region. However, previous seismic hazard studies conducted for the broader Greek region or Europe have obviously included Boeotia. Danciu et al. (2021) conducted a recent study with the aim of updating the seismic hazard map for Europe, which was previously established by Woessner et al. (2015). Utilizing the probabilistic method, Danciu et al. (2021) computed PGA values for Boeotia for a return period of 475 years, ranging from 250 cm/s^2 to 450 cm/s^2, in agreement with the results obtained herein from the OQ–engine software package, which fall within this range. Prior to Danciu et al. (2021), Woessner et al. (2015) conducted a seismic hazard study proposing PGA values for a return period of 475 years, with the PGA values for Boeotia ranging from 300 to 400 cm/s^2. These values are similar to those obtained using the OQ–engine software. Another PSHA study that focused on the Greek region was conducted by Tselentis and Danciu (2010), who computed PGA values for Boeotia ranging from 300 to 500 cm/s^2, providing higher values than the ones computed in this thesis (maximum ~400 cm/s^2). Differences in PGA values are expected due to variations in the

parameters adopted by each study, ranging from the earthquake catalogue to the seismotectonic model. In terms of the stochastic finite fault earthquake scenario approach utilized in this thesis to estimate PGA, PGV, and Sa values, no studies have simulated the exact same earthquake ruptures.

The computational scheme utilized in this thesis was subject to certain limitations and potential sources of bias. With respect to the PSHA method, no new area sources were developed for the broader Boeotia region. By creating area sources within a distance of 100 km from Boeotia, it would have been possible to more accurately characterize the seismotectonic features, as the scaling of observations would have been significantly smaller compared to that of an entire country or whole continent. Furthermore, in addition to the area source seismotectonic model, all active faults in the PSHA framework should have been incorporated. However, this requires knowledge of specific kinematic and tectonic characteristics for each active fault, which is a challenging task for areas like Boeotia, because the region lies north of the Eastern Gulf of Corinth, where there are multiple offshore faults, whose characteristics remain unknown. The GMPEs were derived from seismological data from throughout Greece, as there are no adequate data to focus on the local area of Boeotia. Concerning the finite fault stochastic ground motion technique, all physical properties were obtained from established publications, such as the anelastic attenuation parameters, the geometrical spreading, and the kappa values. This implies that ground motions were estimated based on generic properties, which could have impacted the attenuation of seismic waves.

The Boeotia region has not undergone any seismic hazard studies in the past. The maximum expected ground motions have, until the completion of this thesis, been deduced only through interpolations from studies that have focused on the entire country of Greece, rather than solely on Boeotia. The scope of this local study justifies the use of a large sample size in the MC sampling. Additionally, this thesis employs a sophisticated logic tree approach that significantly reduces epistemic uncertainties. Logic tree approaches are considered to minimize epistemic uncertainties by adopting multiple outcomes in the computational scheme (Bommer and Scherbaum, 2008; Atkinson et al., 2014; Marzocchi et al., 2015). More branches result in a greater number of possible outcomes that are simultaneously accounted for in the logic tree approach. In this study, the PSHA section considers three seismotectonic models, and for each area source of each model, GMPEs with the variable of focal mechanism were reconstructed to account for the varying faulting types as percentages, instead of extrapolating the predominant type of focal mechanism for a single area source. This created sub–logic trees for each area source for a single seismotectonic model. The final output of the PSHA method took into account all three seismotectonic models. To reduce the bias of one method, the scenario–based finite fault stochastic ground motion method was also employed to eliminate the effect of the return periods and to investigate hazardous fault rupture scenarios for Boeotia. The results of this thesis contribute to a current seismic hazard background for Boeotia that may serve to update the regulations proposed by the EAK (2003).

Possible future research endeavors may involve the development of local area source zones that delineate the seismotectonic characteristics of the Boeotia region. Additionally, a GMPE ranking system could be performed to assess and rank the current GMPEs. Moreover, the epicentral distance could be converted to Joyner and Boore distance to incorporate newer GMPEs, such as the one by Boore et al. (2020). Furthermore, fieldwork focused on seismic microzonation could be conducted to provide a more comprehensive understanding of the actual site amplifications and introduce site effects to seismic hazard calculations. Regarding the scenario–based finite fault stochastic ground motion method, the parameters could be calculated using seismological data rather than adopting international properties.

6 Conclusions

The present master's thesis endeavors to evaluate the seismic hazard in Boeotia, situated in Central Greece, with reduced epistemic uncertainties. The underlying impetus for this study stems from the Thiva 2020-2021 earthquake sequence, the mainshock of which is the 02/12/2020 Mw = 4.6 event that was located close to Kallithea village and the aftershocks lasted for approximately one month. Several months later, an intermediate, in terms of magnitude, event occurred a few km west of Kallithea village, close to Thiva, which increased the seismic activity of the area. Thiva is known for hosting strong earthquake occurrences, such as the M = 6.0 in 1914. Therefore, the evaluation of seismic hazard for Boeotia holds significant importance owing to the likelihood of high ground motions, which may occur, possibly close to densely populated localities, due to earthquakes with higher magnitudes, despite it being an area of moderate seismicity.

The assessment of seismic hazard is carried out using two methods: probabilistic and scenario–based finite fault stochastic ground motion simulation. For the first method, the PGA, PGV, and Sa results are obtained for return periods of 475 and 950 years through a logic tree procedure to include multiple outcome variations in order to represent accurate mean values of PGA, PGV, and Sa. The UHS are also constructed for Thiva and Livadia based on the Sa results. The second method assumes that a fault will rupture due to the occurrence of an event of a specific magnitude. Three earthquakes are used to calibrate the parameters to ensure data availability. After the calibration of the site and path parameters, simulation–scenarios are created, and the modeled ground motions are obtained in terms of PGA, PGV, and Sa. Candidate faults are selected based on their likelihood to produce high ground motions and their proven previous seismic activity.

Regarding the PSHA PGA and PGV maps, two areas of high seismic hazard level are identified, i.e., one at the western part of the study area and the other at southeastern Boeotia, close to Thiva. Regarding the two most populated localities, Thiva and Livadia, the first has larger PGA values for all the range of return periods, as depicted in the PGA–hazard curves. Moreover, Thiva has greater Sa values for all periods in the range of 0.1 s to 2.0 s. The PGA results for a return period of 475 years are compared to the reference value proposed by the Greek Building Code. Only the northern part of Boeotia is covered by the regulations of EAK (2003). Nevertheless, it is imperative to acknowledge that the acceleration values provided by the building code are generally expected to be lower than each PSHA, given that they are considered as normalizing factors aiding the construction of smoothed elastic response spectra (Algermissen and Perkins, 1976). Regardless, there is no single definitive PSHA model of seismic hazard due to the significant uncertainties involved in this scientific field. According to the results of the finite fault stochastic ground simulation method, Thiva is highly susceptible to the occurrence of a Mw = 6.3 scenario earthquake that ruptures the fault zone of Kallithea and Mavrovouni. Both the elastic spectra and the UHS indicated that the higher spectral amplitudes were identified for the periods of range [0.15, 0.30] s.

Overall, this thesis aims to reduce epistemic uncertainties by employing two distinct methods for seismic hazard assessment and implementing a sophisticated logic tree approach in the framework of PSHA. However, the update of the seismic hazard of Boeotia with new data and methods is vital to maintain an up–to–date knowledge of the maximum expected ground motions. In future work, the automation of all file preparation tasks required for software package execution will be pursued to improve the computational efficiency of the analysis by introducing batch file runs between PSHA and finite fault stochastic ground motion simulation.

7 Bibliography

Abd el-aal, A., Kamal, H., Abdelhay, M., Elzahaby, K., 2015. Probabilistic and stochastic seismic hazard assessment for wind turbine tower sites in Zafarana Wind Farm, Gulf of Suez, Egypt. Bulletin of Engineering Geology and the Environment 74, 1225–1241. https://doi.org/10.1007/s10064-015-0717-x

Abercrombie, R.E., Main, I.G., Douglas, A., Burton, P.W., 1995. The nucleation and rupture process of the 1981 Gulf of Corinth earthquakes from deconvolved broad-band data. Geophysical Journal International 120, 393–405. https://doi.org/10.1111/j.1365-246X.1995.tb01827.x

Abrahamson, N.A., Bommer, J.J., 2005. Probability and Uncertainty in Seismic Hazard Analysis. Earthquake Spectra 21, 603–607. https://doi.org/10.1193/1.1899158

Aki, K., 1965. Maximum likelihood estimate of b in the formula log N = a-bM and its confidence limits. Bull. Earthq. Res. Inst. 43, 237–239.

Akkar, S., Sandıkkaya, M.A., Bommer, J.J., 2014. Empirical ground-motion models for point- and extended-source crustal earthquake scenarios in Europe and the Middle East. Bull Earthquake Eng 12, 359–387. https://doi.org/10.1007/s10518-013-9461-4

Albini, P., Pantosti, D., 2004. The 20 and 27 April 1894 (Locris, Central Greece) Earthquake Sources through Coeval Records on Macroseismic Effects. Bulletin of the Seismological Society of America 94, 1305–1326. https://doi.org/10.1785/012003174

Algermissen, S.T., Perkins, D.M., 1976. A probabilistic estimate of maximum acceleration in rock in the contiguous United States. US Geological Survey Reston, VA.

Allen, T.I., Wald, D.J., 2009. On the Use of High-Resolution Topographic Data as a Proxy for Seismic Site Conditions (VS30). Bulletin of the Seismological Society of America 99, 935–943. https://doi.org/10.1785/0120080255

Ambraseys, N., 2009. Earthquake in the Mediterranean and in the Middle East: A Multidisciplinary Study of Seismicity up to 1900. Cambridge University Press, New York, 968.

Ambraseys, N.N., Jackson, J.A., 1990. Seismicity and associated strain of central Greece between 1890 and 1988. Geophysical Journal International 101, 663–708. https://doi.org/10.1111/j.1365-246X.1990.tb05577.x

Anderson, J.G., Hough, S.E., 1984. A model for the shape of the fourier amplitude spectrum of acceleration at high frequencies. Bulletin of the Seismological Society of America 74, 1969–1993. https://doi.org/10.1785/BSSA0740051969

Armijo, R., Meyer, B., Hubert, A., Barka, A., 1999. Westward propagation of the North Anatolian fault into the northern Aegean: Timing and kinematics. Geology 27, 267–270. https://doi.org/10.1130/0091-7613(1999)027<0267:WPOTNA>2.3.CO;2

Armijo, R., Meyer, B., King, G.C.P., Rigo, A., Papanastassiou, D., 1996. Quaternary evolution of the Corinth Rift and its implications for the Late Cenozoic evolution of the Aegean. Geophysical Journal International 126, 11–53. https://doi.org/10.1111/j.1365-246X.1996.tb05264.x

Atkinson, G.M., 2004. Empirical Attenuation of Ground-Motion Spectral Amplitudes in Southeastern Canada and the Northeastern United States. Bulletin of the Seismological Society of America 94, 1079–1095.

Atkinson, G.M., 1996. The high-frequency shape of the source spectrum for earthquakes in eastern and western Canada. Bulletin of the Seismological Society of America 86, 106–112. https://doi.org/10.1785/BSSA08601A0106

Atkinson, G.M., Assatourians, K., 2014. Implementation and Validation of EXSIM (A Stochastic Finite-Fault Ground-Motion Simulation Algorithm) on the SCEC Broadband Platform. Seismological Research Letters 86, 48–60. https://doi.org/10.1785/0220140097

Atkinson, G.M., Beresnev, I., 1997. Don't Call it Stress Drop. Seismological Research Letters 68, 3–4. https://doi.org/10.1785/gssrl.68.1.3

Atkinson, G.M., Bommer, J.J., Abrahamson, N.A., 2014. Alternative Approaches to Modeling Epistemic Uncertainty in Ground Motions in Probabilistic Seismic-Hazard Analysis. Seismological Research Letters 85, 1141–1144. https://doi.org/10.1785/0220140120

Avallone, A., Briole, P., Agatza-Balodimou, A.M., Billiris, H., Charade, O., Mitsakaki, C., Nercessian, A., Papazissi, K., Paradissis, D., Veis, G., 2004. Analysis of eleven years of deformation measured by GPS in the Corinth Rift Laboratory area. Comptes Rendus Geoscience 336, 301–311. https://doi.org/10.1016/j.crte.2003.12.007

Baker, J., 2015. Introduction to Probabilistic Seismic Hazard Analysis. White Paper Version 2.1. 77.

Baker, J., Bradley, B., Stafford, P., 2021. Seismic Hazard and Risk Analysis. Cambridge University Press, Cambridge, England. 79.

Bernard, P., Briole, P., Meyer, B., Lyon-Caen, H., Gomez, J.-M., Tiberi, C., Berge, C., Cattin, R., Hatzfeld, D., Lachet, C., Lebrun, B., Deschamps, A., Courboulex, F., Larroque, C., Rigo, A., Massonnet, D., Papadimitriou, P., Kassaras, J., Diagourtas, D., Makropoulos, K., Veis, G., Papazisi, E., Mitsakaki, C., Karakostas, V., Papadimitriou, E., Papanastassiou, D., Chouliaras, M., Stavrakakis, G., 1997. The Ms = 6.2, June 15, 1995 Aigion earthquake (Greece): evidence for low angle normal faulting in the Corinth rift. Journal of Seismology 1, 131–150. https://doi.org/10.1023/A:1009795618839

Bernard, P., Lyon-Caen, H., Briole, P., Deschamps, A., Boudin, F., Makropoulos, K., Papadimitriou, P., Lemeille, F., Patau, G., Billiris, H., Paradissis, D., Papazissi, K., Castarède, H., Charade, O., Nercessian, A., Avallone, A., Pacchiani, F., Zahradnik, J., Sacks, S., Linde, A., 2006. Seismicity, deformation and seismic hazard in the western rift of Corinth: New insights from the Corinth Rift Laboratory (CRL). Tectonophysics 426, 7–30. https://doi.org/10.1016/j.tecto.2006.02.012

Bindi, D., Massa, M., Luzi, L., Ameri, G., Pacor, F., Puglia, R., Augliera, P., 2014. Pan-European ground-motion prediction equations for the average horizontal component of PGA, PGV, and 5 %-damped PSA at spectral periods up to 3.0 s using the RESORCE dataset. Bull Earthquake Eng 12, 391–430. https://doi.org/10.1007/s10518-013-9525-5

Bommer, J.J., Scherbaum, F., 2008. The Use and Misuse of Logic Trees in Probabilistic Seismic Hazard Analysis. Earthquake Spectra 24, 997–1009. https://doi.org/10.1193/1.2977755

Bonatis, P., 2020. Strong ground motion simulation in the Central Ionian Islands using a hybrid (deterministic and stochastic) approach. Master Thesis, School of Geology, Aristotle University of Thessaloniki. 129.

Boore, D.M., 2009. Comparing Stochastic Point-Source and Finite-Source Ground-Motion Simulations: SMSIM and EXSIM. Bulletin of the Seismological Society of America 99, 3202–3216. https://doi.org/10.1785/0120090056

Boore, D.M., 2003. Simulation of Ground Motion Using the Stochastic Method. pure and applied geophysics 160, 635–676. https://doi.org/10.1007/PL00012553

Boore, D.M., 1983. Stochastic simulation of high-frequency ground motions based on seismological models of the radiated spectra. Bulletin of the Seismological Society of America 73, 1865–1894. https://doi.org/10.1785/BSSA07306A1865

Boore, D.M., Stewart, J.P., Skarlatoudis, A.A., Seyhan, E., Margaris, B., Theodoulidis, N., Scordilis, E., Kalogeras, I., Klimis, N., Melis, N.S., 2020. A Ground-Motion Prediction Model for Shallow Crustal Earthquakes in Greece. Bulletin of the Seismological Society of America 111, 857–874. https://doi.org/10.1785/0120200270

Box, G., 197. Science and statistics. Journal of the American Statistical Association, 71(356):791–799.

Briole, P., Ganas, A., Elias, P., Dimitrov, D., 2021. The GPS velocity field of the Aegean. New observations, contribution of the earthquakes, crustal blocks model. Geophysical Journal International 226, 468–492. https://doi.org/10.1093/gji/ggab089

Brune, J.N., 1970. Tectonic stress and the spectra of seismic shear waves from earthquakes. Journal of Geophysical Research (1896-1977) 75, 4997–5009. https://doi.org/10.1029/JB075i026p04997

Byrne, M.D., 2013. How many times should a stochastic model be run? An approach based on confidence intervals, in: Proceedings of the 12th International Conference on Cognitive Modeling, Ottawa.

Caputo, R., Pavlides, S., 2013. Greek Database of Seismogenic Sources (GreDaSS). https://doi.org/10.15160/UNIFE/GREDASS/0200

Chousianitis, K., Del Gaudio, V., Pierri, P., Tselentis, G.-A., 2018. Regional ground-motion prediction equations for amplitude-, frequency response-, and duration-based parameters for Greece. Earthquake Engng Struct Dyn 47, 2252–2274. https://doi.org/10.1002/eqe.3067

Chousianitis, K., Ganas, A., Evangelidis, C.P., 2015. Strain and rotation rate patterns of mainland Greece from continuous GPS data and comparison between seismic and geodetic moment release. Journal of Geophysical Research: Solid Earth 120, 3909–3931. https://doi.org/10.1002/2014JB011762

Chousianitis, K., Ganas, A., Gianniou, M., 2013. Kinematic interpretation of present-day crustal deformation in central Greece from continuous GPS measurements. Journal of Geodynamics 71, 1–13. https://doi.org/10.1016/j.jog.2013.06.004

Cooke, P., 1979. Statistical inference for bounds of random variables. Biometrika 66, 367–374. https://doi.org/10.1093/biomet/66.2.367

Cormier, V.F., 1990. Seismic attenuation: Observation and measurement, in: Geophysics. Springer US, Boston, MA, pp. 1005–1018. https://doi.org/10.1007/0-387-30752-4_122

Cornell, C., 1968. Engineering Seismic Risk Analysis. Bulletin of the Seismological Society of America. 58, 1583–1606.

Cornell, C.A., 1988. On the seismology-engineering interface. Bulletin of the Seismological Society of America 78, 1020–1026. https://doi.org/10.1785/BSSA0780021020

Danciu, L., Nandan, S., Reyes, C., Basili, R., Weatherill, G., Beauval, C., Rovida, A., Vilanova, S., Sesetyan, K., Bard, P.-Y., Cotton, F., Wiemer, S., Giardini, D., 2021. ESHM20 - EFEHR Technical ReportThe 2020 update of the European Seismic Hazard Model - ESHM20: Model Overview. EFEHR European Facilities of Earthquake Hazard and Risk. https://doi.org/10.12686/A15

Danciu, L., Tselentis, G.-A., 2007. Engineering Ground-Motion Parameters Attenuation Relationships for Greece. Bulletin of the Seismological Society of America 97, 162–183. https://doi.org/10.1785/0120050087

Dang, P., Liu, Q., Xia, S., Ma, W., 2021. A Stochastic Method for Simulating Near-Field Seismograms: Application to the 2016 Tottori Earthquake. Earth and Space Science 8, e2021EA001939. https://doi.org/10.1029/2021EA001939

Doutsos, T., Kontopoulos, N., Poulimenos, G., 1988. The Corinth-Patras rift as the initial stage of continental fragmentation behind an active island arc (Greece). Basin Research 1, 177–190. https://doi.org/10.1111/j.1365-2117.1988.tb00014.x

EAK, 2003. Greek seismic code edited by: Earthquake planning and protection organization. Athens, Greece.

Eginitis, D., 1916. Le tremblement de terre de Thèbes du 17 Octobre 1914. Ann. L'observatoire Natl. D'athènes 7, 23–26.

Elias, P., Briole, P., 2018. Ground Deformations in the Corinth Rift, Greece, Investigated Through the Means of SAR Multitemporal Interferometry. Geochemistry, Geophysics, Geosystems 19, 4836–4857. https://doi.org/10.1029/2018GC007574

Elias, P., Spingos, I., Kaviris, G., Karavias, A., Gatsios, T., Sakkas, V., Parcharidis, I., 2021. Combined Geodetic and Seismological Study of the December 2020 Mw = 4.6 Thiva (Central Greece) Shallow Earthquake. Applied Sciences 11. https://doi.org/10.3390/app11135947

ELSTAT, 2021. Census Results of Population and Housing 2021. Hellenic Statistical Authority. 64.

Evangelidis, C.P., Triantafyllis, N., Samios, M., Boukouras, K., Kontakos, K., Ktenidou, O., Fountoulakis, I., Kalogeras, I., Melis, N.S., Galanis, O., Papazachos, C.B., Hatzidimitriou, P., Scordilis, E., Sokos, E., Paraskevopoulos, P., Serpetsidaki, A., Kaviris, G., Kapetanidis, V., Papadimitriou, P., Voulgaris, N., Kassaras, I., Chatzopoulos, G., Makris, I., Vallianatos, F., Kostantinidou, K., Papaioannou, C., Theodoulidis, N., Margaris, B., Pilidou, S., Dimitriadis, I., Iosif, P., Manakou, M., Roumelioti, Z., Pitilakis, K., Riga, E., Drakatos, G., Kiratzi, A., Tselentis, G. -Akis, 2021. Seismic Waveform Data from Greece

and Cyprus: Integration, Archival, and Open Access. Seismological Research Letters 92, 1672–1684. https://doi.org/10.1785/0220200408

Ganas, A., 2022. NOAFAULTS KMZ layer Version 4.0. Zenodo. https://doi.org/10.5281/zenodo.6326260

Ganas, A., Mouzakiotis, E., Moshou, A., Karastathis, V., 2016. Left-lateral shear inside the North Gulf of Evia Rift, Central Greece, evidenced by relocated earthquake sequences and moment tensor inversion. Tectonophysics 682, 237–248. https://doi.org/10.1016/j.tecto.2016.05.031

Ganas, A., Oikonomou, I.A., Tsimi, C., 2013. NOAfaults: a digital database for active faults in Greece. geosociety 47, 518–530. https://doi.org/10.12681/bgsg.11079

Ganas, A., Papadopoulos, G., Pavlides, S.B., 2001. The 7 September 1999 Athens 5.9 Ms earthquake: Remote sensing and digital elevation model inputs towards identifying the seismic fault. International Journal of Remote Sensing 22, 191–196. https://doi.org/10.1080/014311601750038938

Ganas, A., Roberts, G.P., Memou, T., 1998. Segment boundaries, the 1894 ruptures and strain patterns along the Atalanti Fault, Central Greece. Journal of Geodynamics 26, 461–486. https://doi.org/10.1016/S0264-3707(97)00066-5

Ganas, A., Sokos, E., Agalos, A., Leontakianakos, G., Pavlides, S., 2006. Coulomb stress triggering of earthquakes along the Atalanti Fault, central Greece: Two April 1894 M6+ events and stress change patterns. Tectonophysics 420, 357–369. https://doi.org/10.1016/j.tecto.2006.03.028

Gibowicz, S.J., Kijko, A. (Eds.), 1994. Chapter 8 - Attenuation and Scattering of Seismic Waves, in: International Geophysics. Academic Press, pp. 128–175. https://doi.org/10.1016/B978-0-12-282120-2.50012-1

Goodfellow, I., Bengio, Y., Courville, A., 2016. Deep Learning (Adaptive Computation and Machine Learning series). The MIT Press; Illustrated edition. 800.

Goulandris, E., 1916. Sur le tremblement de terre de Thèbes du 17 Octobre 1914. Ann. L'observatoire Natl. D'athènes 7, 47–50.

Graizer, V., Kalkan, E., 2016. Summary of the GK15 ground-motion prediction equation for horizontal PGA and 5% damped PSA from shallow crustal continental earthquakes. Bulletin of the Seismological Society of America 106, 687–707. https://doi.org/10.1785/0120150194

Gutenberg, B., Richter, C.F., 1944. Frequency of earthquakes in California. Bulletin of the Seismological Society of America 34, 185–188. https://doi.org/10.1785/BSSA0340040185

Hanks, T.C., 1979. b values and ω−γ seismic source models: Implications for tectonic stress variations along active crustal fault zones and the estimation of high-frequency strong ground motion. Journal of Geophysical Research: Solid Earth 84, 2235–2242. https://doi.org/10.1029/JB084iB05p02235

Hanks, T.C., McGuire, R.K., 1981. The character of high-frequency strong ground motion. Bulletin of the Seismological Society of America 71, 2071–2095. https://doi.org/10.1785/BSSA0710062071

Hanks, T., 1982. fmax. Bulletin of the Seismological Society of America 72, 1867–1879.

Hatzidimitriou, P.M., 1993. Attenuation of coda waves in northern Greece. PAGEOPH 140, 63–78. https://doi.org/10.1007/BF00876871

Heath, D.C., Wald, D.J., Worden, C.B., Thompson, E.M., Smoczyk, G.M., 2020. A global hybrid VS30 map with a topographic slope–based default and regional map insets. Earthquake Spectra 36, 1570–1584. https://doi.org/10.1177/8755293020911137

Hollenstein, C., Kahle, H.-G., Geiger, A., 2006. Plate tectonic framework and gpsderived strain-rate field within the boundary zones of the eurasian and african plates, in: Pinter, N., Gyula, G., Weber, J., Stein, S., Medak, D. (Eds.), The Adria Microplate: GPS Geodesy, Tectonics and Hazards. Springer Netherlands, Dordrecht, pp. 35–50.

Hubert, A., King, G., Armijo, R., Meyer, B., Papanastasiou, D., 1996. Fault re-activation, stress interaction and rupture propagation of the 1981 Corinth earthquake sequence. Earth and Planetary Science Letters 142, 573–585. https://doi.org/10.1016/0012-821X(96)00108-2

Jackson, J., Fitch, T.J., 1979. Seismotectonic implications of relocated aftershock sequences in Iran and Turkey. Geophysical Journal International 57, 209–229. https://doi.org/10.1111/j.1365-246X.1979.tb03781.x

Jackson, J.A., Gagnepain, J., Houseman, G., King, G.C.P., Papadimitriou, P., Soufleris, C., Virieux, J., 1982. Seismicity, normal faulting, and the geomorphological development of the Gulf of Corinth (Greece): the Corinth earthquakes of February and March 1981. Earth and Planetary Science Letters 57, 377–397. https://doi.org/10.1016/0012-821X(82)90158-3

Jolivet, L., Daniel, J.M., Truffert, C., Goffé, B., 1994. Exhumation of deep crustal metamorphic rocks and crustal extension in arc and back-arc regions. Lithos 33, 3–30. https://doi.org/10.1016/0024-4937(94)90051-5

Kameda, H., 1994. Probabilistic seismic hazard and stochastic ground motions. Engineering Structures 16, 547–557. https://doi.org/10.1016/0141-0296(94)90090-6

Kapetanidis, V., Karakonstantis, A., Papadimitriou, P., Pavlou, K., Spingos, I., Kaviris, G., Voulgaris, N., 2020. The 19 July 2019 earthquake in Athens, Greece: A delayed major aftershock of the 1999 Mw = 6.0 event, or the activation of a different structure? Journal of Geodynamics 139, 101766. https://doi.org/10.1016/j.jog.2020.101766

Kapetanidis, V., Kassaras, I., 2019. Contemporary crustal stress of the Greek region deduced from earthquake focal mechanisms. Journal of Geodynamics 123, 55–82. https://doi.org/10.1016/j.jog.2018.11.004

Karastathis, V.K., Ganas, A., Makris, J., Papoulia, J., Dafnis, P., Gerolymatou, E., Drakatos, G., 2007. The application of shallow seismic techniques in the study of active faults: The Atalanti normal fault, central Greece. Journal of Applied Geophysics 62, 215–233. https://doi.org/10.1016/j.jappgeo.2006.11.004

Karnik, V., 1971. The Seismicity of the European Area. D. Reidel Publishing Co., Dordrecht. 2.

Kaviris, G., 2003. Study of Seismic Source Properties of the Eastern Gulf of Corinth, Ph.D. Thesis. Geophysics-Geothermics Department, Faculty of Geology, University of Athens, Greece (in Greek). 402. http://dx.doi.org/10.12681/eadd/21647

Kaviris, G., Elias, P., Kapetanidis, V., Serpetsidaki, A., Karakonstantis, A., Plicka, V., De Barros, L., Sokos, E., Kassaras, I., Sakkas, V., Spingos, I., Lambotte, S., Duverger, C., Lengliné, O., Evangelidis, C.P., Fountoulakis, I., Ktenidou, O., Gallovič, F., Bufféral, S., Klein, E., Aissaoui, E.M., Scotti, O., Lyon-Caen, H., Rigo, A., Papadimitriou, P., Voulgaris, N., Zahradnik, J., Deschamps, A., Briole, P., Bernard, P., 2021. The Western Gulf of Corinth (Greece) 2020–2021 Seismic Crisis and Cascading Events: First Results from the Corinth Rift Laboratory Network. The Seismic Record 1, 85–95. https://doi.org/10.1785/0320210021

Kaviris, G., Kapetanidis, V., Spingos, I., Sakellariou, N., Karakonstantis, A., Kouskouna, V., Elias, P., Karavias, A., Sakkas, V., Gatsios, T., Kassaras, I., Alexopoulos, J.D., Papadimitriou, P., Voulgaris, N., Parcharidis, I., 2022a. Investigation of the Thiva 2020–2021 Earthquake Sequence Using Seismological Data and Space Techniques. Applied Sciences 12. https://doi.org/10.3390/app12052630

Kaviris, G., Papadimitriou, P., Makropoulos, K., 2007. Magnitude Scales in Central Greece. geosociety 40, 1114–1124. https://doi.org/10.12681/bgsg.16838

Kaviris, G., Spingos, I., Kapetanidis, V., Papadimitriou, P., Voulgaris, N., Makropoulos, K., 2017. Upper crust seismic anisotropy study and temporal variations of shear-wave splitting parameters in the western Gulf of Corinth (Greece) during 2013. Physics of the Earth and Planetary Interiors 269, 148–164. https://doi.org/10.1016/j.pepi.2017.06.006

Kaviris, G., Zymvragakis, A., Bonatis, P., Kapetanidis, V., Voulgaris, N., 2022b. Probabilistic and Scenario-Based Seismic Hazard Assessment on the Western Gulf of Corinth (Central Greece). Applied Sciences 12. https://doi.org/10.3390/app122111152

Kaviris, G., Zymvragakis, A., Bonatis, P., Sakkas, G., Kouskouna, V., Voulgaris, N., 2022c. Probabilistic Seismic Hazard Assessment for the Broader Messinia (SW Greece) Region. Pure and Applied Geophysics 179, 551–567. https://doi.org/10.1007/s00024-022-02950-z

Kijko, A., Sellevoll, M.A., 1992. Estimation of earthquake hazard parameters from incomplete data files. Part II. Incorporation of magnitude heterogeneity. Bulletin of the Seismological Society of America 82, 120–134. https://doi.org/10.1785/BSSA0820010120

Kijko, A., Sellevoll, M.A., 1989. Estimation of earthquake hazard parameters from incomplete data files. Part I. Utilization of extreme and complete catalogs with different threshold magnitudes. Bulletin of the Seismological Society of America 79, 645–654. https://doi.org/10.1785/BSSA0790030645

Kijko, A., Smit, A., 2012. Extension of the Aki-Utsu b-Value Estimator for Incomplete Catalogs. Bulletin of the Seismological Society of America 102, 1283–1287. https://doi.org/10.1785/0120110226

Klein, F.W., 2002. User's guide to HYPOINVERSE-2000, a Fortran program to solve for earthquake locations and magnitudes (Report No. 2002–171), Open-File Report. https://doi.org/10.3133/ofr02171

Klimis, N.S., Margaris, B.N., Koliopoulos, P.K., 1999. Site-dependent amplification functions and response spectra in Greece. Journal of Earthquake Engineering 3, 237–270. https://doi.org/10.1080/13632469909350346

Kokkalas, S., Pavlides, S., Koukouvelas, I., Ganas, A., Stamatopoulos, L., 2007. Paleoseismicity of the Kaparelli fault (eastern Corinth Gulf): evidencefor earthquake recurrence and fault behaviour. Bollettino- Societa Geologica Italiana (Italian Journal of Geosciences). 126, 387–395.

Kouskouna, V., Ganas, A., Kleanthi, M., Kassaras, I., Sakellariou, N., Sakkas, G., Valkaniotis, S., Manousou, E., Bozionelos, G., Tsironi, V., Karamitros, I., Tavoularis, N., Papaioannou, Ch., Bossu, R., 2021. Evaluation of macroseismic intensity, strong ground motion pattern and fault model of the 19 July 2019 Mw5.1 earthquake west of Athens. Journal of Seismology 25, 747–769. https://doi.org/10.1007/s10950-021-09990-3

Kouskouna, V., Malakatas, N., 2000. Correlation between EMS98 with damage reported of the earthquake of 7th September 1999. Annales Géologiques des Pays Helléniques XXXVIII/B, 187–196.

Kouskouna, V., Sakkas, G., Cecic, I., Sakkas, S., Kaviris, G., Tertulliani, A., 2020. Earthquake induced crises: game tree approached risk communication and lessons learnt. Annals of Geophysics 63, 6. https://doi.org/10.4401/ag-8405

Kranis, H., Papanikolaou, D., 2001. Evidence for detachment faulting on the NE Parnassos mountain front (Central Greece). geosociety 34, 281–287. https://doi.org/10.12681/bgsg.17024

Kreemer, C., Chamot-Rooke, N., 2004. Contemporary kinematics of the southern Aegean and the Mediterranean Ridge. Geophysical Journal International 157, 1377–1392. https://doi.org/10.1111/j.1365-246X.2004.02270.x

Ktenidou, O., Cotton, F., Abrahamson, N.A., Anderson, J.G., 2014. Taxonomy of κ: A Review of Definitions and Estimation Approaches Targeted to Applications. Seismological Research Letters 85, 135–146. https://doi.org/10.1785/0220130027

Ktenidou, O. -J., Gélis, C., Bonilla, L. -F., 2013. A Study on the Variability of Kappa (κ) in a Borehole: Implications of the Computation Process. Bulletin of the Seismological Society of America 103, 1048–1068. https://doi.org/10.1785/0120120093

Lay, T., Wallace, T.C., 1995. Modern Global Seismology. London: Academic Press. 58, 521. https://doi.org/10.1016/s0074-6142%2805%29x8001-9

Louvari, E., Kiratzi, A., 2001. Source parameters of the 7 September 1999 Athens (Greece) earthquake based on teleseismic data. Journal of the Balkan Geophysical Society 4, 51–60.

Luzi, L., Puglia, R., Russo, E., D'Amico, M., Felicetta, C., Pacor, F., Lanzano, G., Çeken, U., Clinton, J., Costa, G., Duni, L., Farzanegan, E., Gueguen, P., Ionescu, C., Kalogeras, I., Özener, H., Pesaresi, D., Sleeman, R., Strollo, A., Zare, M., 2016. The Engineering Strong-Motion Database: A Platform to Access Pan-European Accelerometric Data. Seismological Research Letters 87, 987–997. https://doi.org/10.1785/0220150278

Makropoulos, K., Kaviris, G., Kouskouna, V., 2012. An updated and extended earthquake catalogue for Greece and adjacent areas since 1900. Natural Hazards and Earth System Sciences 12, 1425–1430. https://doi.org/10.5194/nhess-12-1425-2012

Makropoulos, K., Kouskouna, V., 1994. The 1894 April 20 and 27 Atalanti earthquakes: 100 years after—lessons learnt. In Proceedings of the XXIV ESC General Assembly, Athens, Greece, 19–24 September 1, 61–71.

Margaris, B., Papazachos, C., Papaioannou, C., Theodulidis, N., Kalogeras, I., Skarlatoudis, A., 2002. Empirical attenuation relations for the horizontal strong ground motion parameters of shallow earthquakes in Greece. in Proc. of the 12th European Conf. on Earthquake Engineering, 9–13 September, London. 11.

Margaris, B.N., Boore, D.M., 1998. Determination of $\Delta\sigma$ and $\kappa 0$ from response spectra of large earthquakes in Greece. Bulletin of the Seismological Society of America 88, 170–182. https://doi.org/10.1785/BSSA0880010170

Marzocchi, W., Taroni, M., Selva, J., 2015. Accounting for Epistemic Uncertainty in PSHA: Logic Tree and Ensemble Modeling. Bulletin of the Seismological Society of America 105, 2151–2159. https://doi.org/10.1785/0120140131

McGuire, R.K., 1976. FORTRAN computer program for seismic risk analysis (Report No. 76–67), Open-File Report. https://doi.org/10.3133/ofr7667

McGuire, R.K., Shedlock, K.M., 1981. Statistical uncertainties in seismic hazard evaluations in the United States. Bulletin of the Seismological Society of America 71, 1287–1308.

McKenzie, D., 1978. Active tectonics of the Alpine—Himalayan belt: the Aegean Sea and surrounding regions. Geophysical Journal of the Royal Astronomical Society 55, 217–254. https://doi.org/10.1111/j.1365-246X.1978.tb04759.x

Mesimeri, M., Karakostas, V., Papadimitriou, E., Tsaklidis, G., Jacobs, K., 2018. Relocation of recent seismicity and seismotectonic properties in the Gulf of Corinth (Greece). Geophysical Journal International 212, 1123–1142. https://doi.org/10.1093/gji/ggx450

Michas, G., Kapetanidis, V., Spingos, I., Kaviris, G., Vallianatos, F., 2022. The 2020 Perachora peninsula earthquake sequence (East Corinth Rift, Greece): spatiotemporal evolution and implications for the triggering mechanism. Acta Geophysica 70, 2581–2601. https://doi.org/10.1007/s11600-022-00864-x

Mitsopoulos, K., 1895. O megas tis Lokridos seismos kata aprilion tou 1894. Ethnikon Typographeion, Athinai, 40, (In Greek).

Mori, T., Shigefuji, M., Bijukchhen, S., Kanno, T., Takai, N., 2020. Ground motion prediction equation for the Kathmandu Valley, Nepal based on strong motion records during the 2015 Gorkha Nepal earthquake sequence. Soil Dynamics and Earthquake Engineering 135, 106208. https://doi.org/10.1016/j.soildyn.2020.106208

Motazedian, D., Atkinson, G.M., 2005. Stochastic Finite-Fault Modeling Based on a Dynamic Corner Frequency. Bulletin of the Seismological Society of America 95, 995–1010. https://doi.org/10.1785/0120030207

Musson, R., 2012. On the Nature of Logic Trees in Probabilistic Seismic Hazard Assessment. Earthquake Spectra 28, 1291–1296. https://doi.org/10.1193/1.4000062

Nyst, M., Thatcher, W., 2004. New constraints on the active tectonic deformation of the Aegean. Journal of Geophysical Research: Solid Earth 109. https://doi.org/10.1029/2003JB002830

Ordaz, M., Salgado-Gálvez, M.A., Giraldo, S., 2021. R-CRISIS: 35 years of continuous developments and improvements for probabilistic seismic hazard analysis. Bull Earthquake Eng 19, 2797–2816. https://doi.org/10.1007/s10518-021-01098-w

Pagani, M., Monelli, D., Weatherill, G., Danciu, L., Crowley, H., Silva, V., Henshaw, P., Butler, L., Nastasi, M., Panzeri, L., Simionato, M., Vigano, D., 2014. OpenQuake Engine: An Open Hazard (and Risk) Software for the Global Earthquake Model. Seismological Research Letters 85, 692–702. https://doi.org/10.1785/0220130087

Pantosti, D., De Martini, P.M., Papanastassiou, D., Palyvos, N., Lemeille, F., Stavrakakis, G., 2001. A Reappraisal of the 1894 Atalanti Earthquake Surface Ruptures, Central Greece. Bulletin of the Seismological Society of America 91, 760–780. https://doi.org/10.1785/0120000051

Papadimitriou, P., Kaviris, G., Makropoulos, K., 1999. Evidence of shear-wave splitting in the eastern Corinthian Gulf (Greece). Physics of the Earth and Planetary Interiors 114, 3–13. https://doi.org/10.1016/S0031-9201(99)00041-2

Papadimitriou, P., Voulgaris, N., Kassaras, I., Kaviris, G., Delibasis, N., Makropoulos, K., 2002. The Mw = 6.0, 7 September 1999 Athens Earthquake. Natural Hazards 27, 15–33. https://doi.org/10.1023/A:1019914915693

Papadopoulos, G.A., 2002. The Athens, Greece, Earthquake (Ms 5.9) of 7 September 1999: An Event Triggered by the İzmit, Turkey, 17 August 1999 Earthquake? Bulletin of the Seismological Society of America 92, 312–321. https://doi.org/10.1785/0120000805

Papageorgiou, A.S., Aki, K., 1983. A specific barrier model for the quantitative description of inhomogeneous faulting and the prediction of strong ground motion. I. Description of the model. Bulletin of the Seismological Society of America 73, 693–722.

Papanikolaou, D.J., Royden, L.H., 2007. Disruption of the Hellenic arc: Late Miocene extensional detachment faults and steep Pliocene-Quaternary normal faults—Or what happened at Corinth? Tectonics 26. https://doi.org/10.1029/2006TC002007

Papazachos, B., 1989. Measures of earthquake size in Greece and surrounding area. Proceedings of the 1st Scientific Conference in Geophysics, Geological Society of Greece 19-21 April, 438–447.

Papazachos, B., Papazachou, C., 2003. The Earthquakes of Greece. Ziti Publications, Thessaloniki, 273 (In Greek).

Papazachos, B., Papazachou, C., 1997. The Earthquakes of Greece. Editions Ziti, Thessaloniki. 304.

Papazachos, B.C., Comninakis, P.E., Papadimitriou, E., Scordilis, E., 1984. Properties of the February-March 1981 seismic sequence in the Alkyonides gulf in central Greece. Annales Geophysicae 2, 537–544.

Pavlou, K., Kaviris, G., Kouskouna, V., Sakkas, G., Zymvragakis, A., Sakkas, V., Drakatos, G., 2021. Minor seismic hazard changes in the broader area of Pournari artificial lake after the

first filling (W. Greece). Results in Geophysical Sciences 100025. https://doi.org/10.1016/j.ringps.2021.100025

Prabhu, K., 2014. Window Functions and Their Applications in Signal Processing. CRC Press, Florida, 265-271.

Pujol, J. (Ed.), 2003. Anelastic attenuation, in: Elastic Wave Propagation and Generation in Seismology. Cambridge University Press, Cambridge, pp. 357–390. https://doi.org/10.1017/CBO9780511610127.012

Raghucharan, M.C., Surendra Nadh Somala, 2018. Stochastic Extended Simulation (EXSIM) of Mw 7.0 Kumamoto-Shi earthquake on 15 April 2016 in the Southwest of Japan using the SCEC Broadband Platform (BBP). AIMS Geosciences 4, 144–165. https://doi.org/10.3934/geosci.2018.2.144

Raghukanth, S.T.G., Nadh Somala, S., 2009. Modeling of Strong-Motion Data in Northeastern India: Q, Stress Drop, and Site Amplification. Bulletin of the Seismological Society of America 99, 705–725. https://doi.org/10.1785/0120080025

Rigo, A., Lyon-Caen, H., Armijo, R., Deschamps, A., Hatzfeld, D., Makropoulos, K., Papadimitriou, P., Kassaras, I., 1996. A microseismic study in the western part of the Gulf of Corinth (Greece): implications for large-scale normal faulting mechanisms. Geophysical Journal International 126, 663–688. https://doi.org/10.1111/j.1365-246X.1996.tb04697.x

Robson, D.S., Whitlock, J.H., 1964. Estimation of a truncation point. Biometrika 51, 33–39. https://doi.org/10.1093/biomet/51.1-2.33

Rovida, A., Antonucci, A., Locati, M., 2022. The European Preinstrumental Earthquake Catalogue EPICA, the 1000–1899 catalogue for the European Seismic Hazard Model 2020. Earth System Science Data Discussions 2022, 1–30. https://doi.org/10.5194/essd-2022-103

Sabetta, F., Pugliese, A., Fiorentino, G., Lanzano, G., Luzi, L., 2021. Simulation of non-stationary stochastic ground motions based on recent Italian earthquakes. Bulletin of Earthquake Engineering 19, 3287–3315. https://doi.org/10.1007/s10518-021-01077-1

Sakkas, G., 2016. Calculation and analysis of the seismic motion rotational components in Greece, Ph.D. Thesis. Geophysics-Geothermics Department, Faculty of Geology, University of Athens, Greece (in Greek). 278. http://dx.doi.org/10.12681/eadd/39773

Saragoni, G., Hart, G.C., 1973. Simulation of artificial earthquakes. Earthquake Engineering & Structural Dynamics 2, 249–267. https://doi.org/10.1002/eqe.4290020305

Savvaidis, A., Smirnov, M.Yu., Tranos, M.D., Pedersen, L.B., Chouliaras, G., 2012. The seismically active Atalanti fault in Central Greece: A steeply dipping fault zone imaged from magnetotelluric data. Tectonophysics 554–557, 105–113. https://doi.org/10.1016/j.tecto.2012.06.002

Sboras, S., Ganas, A., Pavlides, S., 2010. Morphotectonic analysis of the neotectonic and active faults of Beotia (central Greece), using g.i.s. techniques. geosociety 43, 1607–1618. https://doi.org/10.12681/bgsg.11335

Shebalin, N., Kárnik, V., Hadzievski, D., 1974. Catalogue of earthquakes of the Balkan region. In Part I, UNDP-UNESCO Survey of the Seismicity of the Balkan Region; UNESCO: Skopje, North Macedonia.

Singh, S.K., García, D., Pacheco, J.F., Valenzuela, R., Bansal, B.K., Dattatrayam, R.S., 2004. Q of the Indian Shield. Bulletin of the Seismological Society of America 94, 1564–1570. https://doi.org/10.1785/012003214

Skarlatoudis, A.A., Papazachos, C.B., Margaris, B.N., Theodulidis, N., Papaioannou, Ch., Kalogeras, I., Scordilis, E.M., Karakostas, V., 2007. Erratum to Empirical Peak Ground-Motion Predictive Relations for Shallow Earthquakes in Greece. Bulletin of the Seismological Society of America 97, 2219–2221. https://doi.org/10.1785/0120070176

Skarlatoudis, A.A., Papazachos, C.B., Margaris, B.N., Theodulidis, N., Papaioannou, Ch., Kalogeras, I., Scordilis, E.M., Karakostas, V., 2003. Empirical Peak Ground-Motion Predictive Relations for Shallow Earthquakes in Greece. Bulletin of the Seismological Society of America 93, 2591–2603. https://doi.org/10.1785/0120030016

Skouphos, T., 1894. Die zwei grossen Erdbeben in Lokris am 8/20 und 15/27 April 1894. Zeitschrift der Gesellschaft fu¨r Erdkunde zu Berlin, 29, 409–475.

Stucchi, M., Rovida, A., Gomez Capera, A.A., Alexandre, P., Camelbeeck, T., Demircioglu, M.B., Gasperini, P., Kouskouna, V., Musson, R.M.W., Radulian, M., Sesetyan, K., Vilanova, S., Baumont, D., Bungum, H., Fäh, D., Lenhardt, W., Makropoulos, K., Martinez Solares, J.M., Scotti, O., Živčić, M., Albini, P., Batllo, J., Papaioannou, C., Tatevossian, R., Locati, M., Meletti, C., Viganò, D., Giardini, D., 2013. The SHARE European Earthquake Catalogue (SHEEC) 1000–1899. Journal of Seismology 17, 523–544. https://doi.org/10.1007/s10950-012-9335-2

Thingbaijam, K.K.S., Martin Mai, P., Goda, K., 2017. New Empirical Earthquake Source-Scaling Laws. Bulletin of the Seismological Society of America 107, 2225–2246. https://doi.org/10.1785/0120170017

Tolis, S.V., 2014. Chapter 20 - To What Extent Can Engineering Reduce Seismic Risk?, in: Shroder, J.F., Wyss, M. (Eds.), Earthquake Hazard, Risk and Disasters. Academic Press, Boston, pp. 531–541. https://doi.org/10.1016/B978-0-12-394848-9.00020-1

Tselentis, G.-A., Danciu, L., 2010. Probabilistic seismic hazard assessment in Greece – Part 1: Engineering ground motion parameters. Nat. Hazards Earth Syst. Sci. 10, 25–39. https://doi.org/10.5194/nhess-10-25-2010

Tsodoulos, I.M., Koukouvelas, I.K., Pavlides, S., 2008. Tectonic geomorphology of the easternmost extension of the Gulf of Corinth (Beotia, Central Greece). Tectonophysics 453, 211–232. https://doi.org/10.1016/j.tecto.2007.06.015

Valkanou, K., Karymbalis, E., Papanastassiou, D., Soldati, M., Chalkias, C., Gaki-Papanastassiou, K., 2021. Assessment of Neotectonic Landscape Deformation in Evia Island, Greece, Using GIS-Based Multi-Criteria Analysis. ISPRS International Journal of Geo-Information 10. https://doi.org/10.3390/ijgi10030118

Vamvakaris, D.A., Papazachos, C.B., Papaioannou, Ch.A., Scordilis, E.M., Karakaisis, G.F., 2016. A detailed seismic zonation model for shallow earthquakes in the broader Aegean area. Nat. Hazards Earth Syst. Sci. 16, 55–84. https://doi.org/10.5194/nhess-16-55-2016

Vita-Finzi, C., King, G.C.P., Matthews, D.H., 1985. The seismicity, geomorphology and structural evolution of the Corinth area of Greece. Philosophical Transactions of the Royal Society

of London. Series A, Mathematical and Physical Sciences 314, 379–407. https://doi.org/10.1098/rsta.1985.0024

Voulgaris, N., Pirli, M., Papadimitriou, P., Kassaras, J., Makropoulos, K., 2001. Seismotectonic characteristics of the area of Western Attica derived from the study of the September 7, 1999 Athens earthquake aftershock sequence. geosociety 34, 1645–1651. https://doi.org/10.12681/bgsg.17274

Wang, Z., 2011. Seismic Hazard Assessment: Issues and Alternatives. Pure and Applied Geophysics 168, 11–25. https://doi.org/10.1007/s00024-010-0148-3

Wang, Z., 2006. Understanding Seismic Hazard and Risk Assessments: An Example in The New Madrid Seismic Zone of The Central United States. Proceedings of the 8th U.S. National Conference on Earthquake Engineering, April 18-22, San Francisco, California, USA. 416.

Wang, Z., 2005. A Clear Definition of Seismic Hazard and Risk: A Basis for Hazard and Risk Assessment, Communication, and Management. Presented at the AGU Fall Meeting Abstracts, pp. S53B-1110.

Wells, D.L., Coppersmith, K.J., 1994. New empirical relationships among magnitude, rupture length, rupture width, rupture area, and surface displacement. Bulletin of the Seismological Society of America 84, 974–1002. https://doi.org/10.1785/BSSA0840040974

Wiemer, S., Wyss, M., 2000. Minimum Magnitude of Completeness in Earthquake Catalogs: Examples from Alaska, the Western United States, and Japan. Bulletin of the Seismological Society of America 90, 859–869. https://doi.org/10.1785/0119990114

Woessner, J., Laurentiu, D., Giardini, D., Crowley, H., Cotton, F., Grünthal, G., Valensise, G., Arvidsson, R., Basili, R., Demircioglu, M.B., Hiemer, S., Meletti, C., Musson, R.W., Rovida, A.N., Sesetyan, K., Stucchi, M., The SHARE Consortium, 2015. The 2013 European Seismic Hazard Model: key components and results. Bulletin of Earthquake Engineering 13, 3553–3596. https://doi.org/10.1007/s10518-015-9795-1

Zhou, Y., Zhou, S., Zhuang, J., 2018. A test on methods for MC estimation based on earthquake catalog. Earth and Planetary Physics 2, 150–162. https://doi.org/10.26464/epp2018015